MICRO-ANATOMICAL CHARACTERIZATION OF CENTRAL WHITE MATTER USING MAGNETIC RESONANCE IMAGING

By

Dissertation

Submitted to the Faculty of the

Graduate School of Vanderbilt University

in partial fulfillment of the requirements

for the degree of

DOCTOR OF PHILOSOPHY

in

Biomedical Engineering

May, 2008
Nashville, Tennessee

Approved:

Professor Mark D. Does

Professor John C. Gore

Professor Daniel F. Gochberg

Professor Adam W. Anderson

Professor William M. Valentine

TABLE OF CONTENTS

Page

ACKNOWLEDGEMENTS

This work would not have been possible without the financial support of National Institutes of Health's sub-voxel tissue characterization with in vivo MRI. I am especially indebted to the founding members of the Vanderbilt Institute of Imaging Science, particularly Dr. John Gore, for establishing an environment of state-of-the-art resources fostering both scientific and social collaboration.

I am grateful to all those I had the pleasure to work with. The members of my committee have each provided extensive personal and professional guidance. Their availability and knowledge have been invaluable to my development. I would especially like to thank Dr. Mark Does, the chairman of my committee, for his remarkable patience during my graduate student career. He has been a wonderful mentor and friend and has taught me more than I could ever give him credit for.

The members of the support staff in VUIIS were crucial in the success of this project. Jarrod True, Richard Baheza, and Heather Scott all provided valuable assistance for experimental setup and troubleshooting throughout my studies.

My friends and family have been essential, providing much needed love and support throughout my education. My family has always encouraged my decisions and provided me with much needed confidence. Most importantly, I wish to thank my amazing husband, whose achievements, accompanied by his distinctly relaxed attitude, are a never-ending source of inspiration.

LIST OF TABLES

LIST OF FIGURES

LIST OF ABBREVIATIONS AND SYMBOLS

MRI	magnetic resonance imaging
d	axon diameter
D	fiber diameter
ROI	region of interest
WM	white matter
CNS	central nervous system
PNS	peripheral nervous system
MR	magnetic resonance
NMR	nuclear magnetic resonance
FC	fasciculus cuneatus
FG	fasciculus gracilis
ReST	reticulospinal tract
RST	rubrospinal tract
VST	vestibulospinal tract
^1H	hydrogen nucleus
T_2	*spin-spin* or transverse relaxation time
MT	magnetization transfer
$\mathbf{M}_o$	net magnetization
$\mathbf{B}_o$	static magnetic field
$\mathbf{B}_1$	time-varying magnetic field
ω_{rf}	angular frequency of the time-varying magnetic field
M_T	transverse magnetization
M_z	longitudinal magnetization
ω_o	Larmor frequency
ϕ	phase-angle between the rotating x-axis and $\mathbf{B}_1$
Ω	difference between the Larmor and *rf* frequencies
T_1	*spin-lattice* or longitudinal relaxation
K_1	number of phase encoding steps
K_2	number of read encoding steps
M_o^{mye}	signal contribution from myelin water
T_2^{mye}	transverse relaxation of myelin water
M_o^{ie}	signal contribution from intra- and extra-axonal water
T_2^{ie}	transverse relaxation of intra- and extra-axonal water
S_{WM}	signal from white matter voxel
k_{mie}	diffusion of water molecules from myelin to intra- and extra-axonal compartments
k_{iem}	diffusion of water molecules from intra- and extra-axonal to myelin compartment
MT	magnetization transfer
R_{mf}	magnetization transfer exchange rate between the macromolecular and free pool
R_{fm}	magnetization transfer exchange rate between the free and macromolecular pool
T_2^*	Transverse relaxation with the effects of static field inhomogeneities

τ_{SE}	waiting period between 90° *rf* pulse and 180° *rf* pulse in the *spin-echo* sequence
T_E	echo time
n	echo number
CPMG	Carr-Purcell-Meiboom-Gill method of measuring T_2 relaxation
NNLS	Non-negative, least-squares fitting technique
$\mathbf{y}$	vector of measured echo amplitudes
$\mathbf{A}$	matrix of all possible exponential terms
$\mathbf{S}$	T_2 spectra
λ	regularizing term
χ^2	misfit of fit
MTR	magnetization transfer ratio
qMT	quantitative magnetization transfer
R_1^-	slow recovery rate of qMT
R_1^+	fast recovery rates of qMT
b_f^-	amplitude of slow recovery rate of qMT
b_f^+	amplitude of fast recovery rate of qMT
$M_f(t)$	longitudinal magnetization of free pool at time t
$M_m(t)$	longitudinal magnetization of macromolecular pool at time t
$M_{f\infty}$	equilibrium value of longitudinal magnetization of free pool
$M_{m\infty}$	equilibrium value of longitudinal magnetization of macromolecular pool
R_1	longitudinal relaxation rates when no MT exists
k_{fm}	MT rate from the free to the macromolecular pool
k_{mf}	MT rate from the macromolecular to the free pool
k_{fm}/k_{mf}	pool size ratio
PSR	pool size ratio
SIR	selective inversion recovery
SNR	signal to noise ratio
T_R	repetition time
SW	sweepwidth
N_{aq}	number of averages
ME	multi-echo
N_E	number of echoes
$T_{E,min}$	minimum T_E
ε	Gaussian noise added to simulated signal
σ_n	standard deviation of Gaussian noise added to simulated signal
β_{MWF}	bias of myelin water fraction
r_1	radius of axon
r_2	radius of fiber
σ_{MWF}	standard deviation of myelin water fraction
β_{T_2}	bias of myelin T_2
σ_{T_2}	standard deviation of myelin T_2
T_R	repetition time
FOV	field of view
$T_2^{'mye}$	apparent transverse relaxation of myelin
$M_o^{'mye}$	apparent signal fraction of myelin

$T_2^{'ie}$ apparent transverse relaxation of intra- and extra-axonal compartments
$M_o^{'ie}$ apparent signal fraction of intra- and extra-axonal compartments
τ_{ie} lifetime of spins in the intra- and extra-axonal compartment
$T_{E,max}$ endpoint for echo sampling
SC spinal cord
ANOVA one-way analysis of variance
T_{E1} initial echo time
ρ_m myelin water density
$\tilde{\rho}_m$ apparent myelin water density
MF myelin fraction extracted from quantitative histology
r relaxivity of myelin
R_2 inverse of T_2
R_{2o} initial R_2 value
T_2^{VST} mean T_2 of pixels in the VST region
T_2^{ROI} mean T_2 of pixels in other white matter tracts
ADC apparent diffusion coefficient
$\sigma_{M_0^{ie}}$ standard deviation of intra- and extra-axonal compartment amplitude estimate
SNR_{MWF} signal to noise of the myelin water fraction

CHAPTER I

INTRODUCTION AND BACKGROUND

All magnetic resonance imaging techniques offer tissue contrast with spatial resolution but provide limited information regarding the variation of the magnetic resonance signal that exists on a scale smaller than a voxel. The magnetic resonance signal arising from a heterogeneous tissue, such as spinal cord white matter, is the sum of signals from each tissue compartment within the imaging voxel. Analysis of this signal can better characterize the micro-anatomical heterogeneity tissue, white matter in particular. Many questions remain with regard to the compartmental contributions for the various types of magnetic resonance imaging (MRI) contrast. This project utilizes a variety of *in vitro* studies as well as simulations to better characterize the contribution of different water compartments to conventional MRI methods. Such an understanding of the complex combination of the various relaxation and exchange properties is important in developing an anatomical basis for interpreting magnetization transfer and T_2 weighted images, particularly with respect to myelination.

Myelin

Structure

Myelin is an arrangement of Schwann cell or oligodendrocyte wrapped in a spiral fashion around a segment of axon and its plasma membrane contains phospholipids and

glycoproteins. This membrane arises from its cell of origin as a cytoplasmic process that is then wrapped around the target axon. It is eventually compacted and looses the majority of its cytoplasmic content to form tightly wound membranous sheath comprising a series of alternating lipid and protein lamellae known as compact myelin. Isolated myelin is 70-85% lipid and 15-30% protein. Due to the high myelin content, white matter has relatively low water content (72%) compared to that of gray matter (82%).

Myelin is found in segments called internodes along the axonal fibers. The internodes are delineated on either side by unmyelinated sections called Nodes of Ranvier. Cat spinal cord nerves have been examined and internodal length varied from 0.3-1.5 mm for fiber diameters of 5-25 μm while nodal lengths were estimated from 0.4-4.4 μm [1]. The alternating internodes and Nodes of Ranvier aid in salutatory conduction of the signal along the axon. The myelin acts as a non-conducting envelope to surround the conducting axon and insulate it electrically from the external conducting medium of the intracellular space.

Myelin's cell of origin differs depending on its location in the nervous system. In the central nervous system (CNS) oligodendrocytes may ensheath 30-50 internodes, while in the peripheral nervous system (PNS) a single Schwann cell ensheathes one internode. Schwann cell myelin in the PNS has been found to be thicker than oligodendrocyte myelin by up to 36% in all axon calibers [2]. In comparison, the periodicity of the oligodendrocytes is somewhat smaller and adjacent fibers have little surrounding space resulting in the sheaths commonly touching each other.

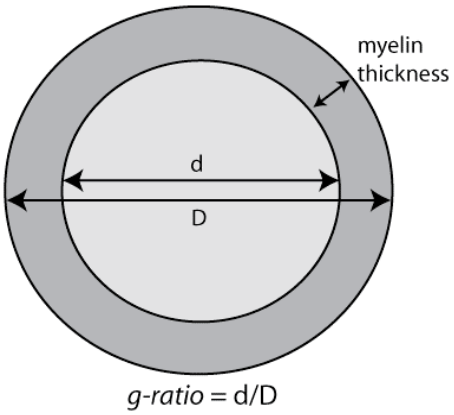

Figure 1.1 – Axon diagram for calculation of *g-ratio*

In mature nerve fibers, the thickness of the myelin sheath is thought to be related to its associated axonal fiber diameter, with larger axons having a thicker myelin sheath. The relationship between the axon size and its myelin thickness is called the *g-ratio*. This ratio is defined by measuring the axon diameter (d) and the myelin thickness, as seen in Figure 1.1. The *g-ratio* is defined as d/D and is a useful tool to characterize the myelin/axon relationship within a specific neuronal tissue. Rushton [3] predicted optimal *g-ratio* of 0.6 for energetically most efficient ratio. If this relationship is assumed to be constant, it implies that the thickness of myelin will vary linearly with local axonal diameters.

Results of *g-ratio* studies vary widely, but they fall broadly into several groups [4], regardless of the animal or nerve investigated; a) constant values of *g-ratio* for all fiber diameters [5-7], b) *g-ratio* rising with increasing fiber diameter and reaching a plateau [8-

11], c) *g-ratio* continues to rise with increasing fiber diameter without a plateau [2], d) values of *g-ratio* smaller in larger fibers [12], and e) no correlation between *g-ratio* and fiber diameter [13].

The location of the fiber is also important when considering *g-ratio* measurements. The *g-ratio* has been found to be higher in the CNS (0.82) than in the PNS (0.78) in studies of the rat vagal nerve [2], cervical [14] and lumbar ventral motorneurons [15], as well as the ventral funiculus of cat spinal cord [16]. Fraher [14] found that the mean myelin sheath thickness and axon circumference are greater for peripheral than for central segments of several nerve fiber bundles in the spinal cord and ventral root. It has also been proposed that the nodal length is longer in the central than in the peripheral nerve fibers [17].

The spinal cord presents unique structural organization of central nervous system white matter. The peripheral regions of the oval-shaped spinal cord contain the well-organized white matter tracts surrounding a characteristic butterfly-shaped grey matter region. The parallel structure of the white matter tracts in the spinal cord facilitates analysis of their myelin properties.

Longitudinal variation of the axon diameter in spinal cord roots has been established [18]. In this study, Lubinska, et al. found that the axon diameter is greater proximal to the cervical spine, suggesting that the diameter of the myelin sheath in the spinal cord is thickest proximally and tapers distally from its origin in the brain stem. Peripheral nerve tapering has also been studied and axon perimeter was found to be significantly greater proximally than distally for the rat phrenic nerve [12]. It can be concluded that fibers taper in their un-branched course, and its been shown that the degree of diameter

reduction and it abruptness vary from one animal to another. If the *g-ratio* is assumed to be dependent on the axon calibers, this suggests that it will be characteristic of the spinal cord location.

In addition to the longitudinal variation along the length of the spinal cord, variation within the transverse plane is also of interest. Although Schwartz et al. [19], as well as others [20, 21], have found no left-right differences between regions of interest (ROI's) in different spinal tracts, transverse in-plane variation of axonal size has been suggested [18]. The configuration of the white matter (WM) tracts in the spinal cord, as well as the postulated variation of myelin thickness, provides motivation for further study on the relationship between axon diameter and myelin thickness.

Fixation of Neural Tissue

Although the gluteraldehyde/osmium fixation is the most widely used for neural tissue preservation [19, 22], tissue fixation is known to change the cellular properties and no one method is beneficial for both axon and myelin preservation. Histological measurements of fiber size will be affected by fixation procedures. A major source of error when attempting quantitative measurements on histology is tissue shrinkage. Van Harreveld, et al. [23] observed on cerebral cortex of mouse that fixation by gluteraldehyde perfusion results in a transport of extracellular material into cellular elements. In the following osmium treatment, extracellular space is again created. Despite this redistribution, Hildebrand and Muller found myelin sheaths decreased by 3.7% in thickness during primary gluteraldehyde fixation in feline white matter [24]. Due to the higher water

content in the intra- and extra-axonal space, the shrinking of the two compartments is expected to be unequal. Despite these effects, the Karnovsky [25] fixation technique is the most widely used and provides a good preservation of axon/myelin coherence [26].

The structure of the myelin sheath and its relation to the axon establish a heterogeneous environment on a microscopic level. The high lipid, low water content of myelin and the contrasting high water content of the intra- and extra-axonal space establish contrasting compartments. The potential variation in the myelin thickness and axon diameter characteristic of specific white matter tracts in the spinal cord provides an exceptional system to examine how the microscopic properties influence the magnetic resonance (MR) signal.

Nuclear Magnetic Resonance *(Haacke, E.M. 1999)*

The principles of nuclear magnetic resonance (NMR) [27, 28] have been exploited in MRI so that NMR signals can be localized in space allowing creation of images [29]. Hydrogen, ^{1}H, is the most abundant nuclei in the human body and it exhibits nuclear magnetic resonance, existing mainly within water molecules. This allows MRI to visualize the water in the body. The NMR signal is sensitive to the physical and chemical environments of the tissue, not only the local water density. This allows manipulation of the signal based on several NMR parameters. The two parameters of interest for this dissertation are the transverse relaxation time (T_2) and magnetization transfer (MT). Manipulation of imaging parameters can allow the image intensity to be controlled. Generation of images based on either T_2 or MT characteristics allows differences in these

parameters to be examined.

Fundamentals of NMR

The water molecule contains two hydrogen nuclei, which are simply protons. The charge of these ^{1}H's results in a net magnetic moment that can be manipulated by an external magnetic field. Exploring the interaction of the ^{1}H's magnetic moment with a static magnetic field will aid in the understanding the principles of NMR.

The charged proton possesses an intrinsic property known as angular momentum. A net magnetic moment results at thermal equilibrium for a population of spins. This net magnetic moment is called the net magnetization or $\mathbf{M}_o$ and is aligned with the static magnetic field, $\mathbf{B}_o$. This net magnetization is manipulated and observed in an NMR experiment.

In an NMR experiment, there is a static magnetic field, as well as a time-varying magnetic field, $\mathbf{B}_1$. This time-varying $\mathbf{B}_1$ is oscillating with an angular frequency ω_{rf} in the plane normal to $\mathbf{B}_o$, where *rf* refers to the radio-frequency. In the presence of the total magnetic field ($\mathbf{B}_o + \mathbf{B}_1$), a magnetic moment precesses. The precession will occur about the axis of the total magnetic field and is described by

$$d\mathrm{M}/dt = \gamma \mathbf{M} \times \mathbf{B}. \qquad [1.1]$$

If the static magnetic field defines the z-axis of the coordinate system, the total magnetic field can be written as

$$\mathbf{B} = \mathbf{B}_1 \cos(\omega_{rf} t)\hat{\mathrm{i}} + \mathbf{B}_1 \sin(\omega_{rf} t)\hat{\mathrm{j}} + \mathbf{B}_o \hat{\mathrm{k}}. \qquad [1.2]$$

When there is no time-varying magnetic field, $\mathbf{B}_1$=0, the solution of Eq. [1.1] is

$$M_T(t) = M_x(t) + \mathrm{i}M_y(t) = M_T(0)\left[\cos(\omega_o t) + \mathrm{i}\cdot\sin(\omega_o t)\right],$$
$$M_z(t) = M_z(0) \qquad [1.3]$$

where the M_T refers to the magnetization in the transverse, or xy-plane. Where,

$$\omega_o \equiv -\gamma \mathbf{B}_o \qquad [1.4]$$

defines the Larmor frequency of precession. This is the frequency at which the angular momentum vector precesses about $\mathbf{B}_o$ with no external forces.

In the situation of an NMR experiment external radio frequency pulses are applied to manipulate the magnetization vector, $\mathbf{B}_1 \neq 0$. To simplify the situation where $\mathbf{B}_1$ is applied, an axis transformation is performed to align with the $\mathbf{B}_1$ field equating ω_{rf} and ω_o. The result is a coordinate system that rotates around the z-axis at the same rate as $\mathbf{M}_T$ at a frequency equal to ω_o. In this reference frame, referred to as the rotating frame, the $\mathbf{B}_1$

appears stationary. This rotating frame is aligned with the previously described axes, the laboratory frame, at the origin and rotating around the common z-axis.

The phase-angle between the rotating x-axis and $\mathbf{B}_1$ is ϕ, and the difference between the Larmor and *rf* frequencies, (ω_o-w_{rf}), is Ω. The net magnetic field after transforming to the rotating frame is

$$\mathbf{B} = B_x\hat{\mathrm{i}} + B_y\hat{\mathrm{j}} + B_z\hat{\mathrm{k}}, \qquad [1.5]$$

where

$$\begin{aligned} B_x &= B_1\cos(\phi) = -\left(\omega_1/\gamma\right)\cos(\phi) \\ B_y &= B_1\sin(\phi) = -\left(\omega_1/\gamma\right)\sin(\phi) \\ B_z &= B_o - \left(-\omega_{rf}/\gamma\right) = \left(\omega_o/\gamma\right) + \left(\omega_{rf}/\gamma\right) = -\Omega/\gamma \end{aligned} \quad . \qquad [1.6]$$

To describe the motion of the magnetization vector in the rotating frame,

$$\frac{d\mathrm{M}}{dt} = \begin{bmatrix} \dot{M}_x \\ \dot{M}_y \\ \dot{M}_z \end{bmatrix} = \begin{bmatrix} \gamma\left(B_z M_y - B_y M_z\right) \\ \gamma\left(-B_z M_x + B_x M_z\right) \\ \gamma\left(B_y M_x - B_x M_y\right) \end{bmatrix} = \begin{bmatrix} -\Omega M_y + \omega_1\sin(\phi) M_z \\ \Omega M_x - \omega_1\cos(\phi) M_z \\ -\omega_1\sin(\phi) M_x + \omega_1\cos(\phi) M_y \end{bmatrix}. \qquad [1.7]$$

Relaxation

In addition to the rotation, the net magnetization vectors also experiences the effects of interactions with their physical environment and with each other. If a group of spins is not in equilibrium, the spins' energy will transfer to the physical environment, also called the lattice, in order to return to equilibrium. The restoration of the net magnetization along the z-axis is referred to as *spin-lattice* or T_1relaxation. As equilibrium is restored, M_z will approach M_o and M_T will decay to zero. There are two main causes for this decay of the transverse magnetization. The first is directly related to the growth of the net magnetization along the z-axis and due to the spin-lattice relaxation. The second involves the effects between spins. The longitudinal relaxation of the magnetization vector, **M**, in the absence of $\mathbf{B}_1$ is described by

$$\begin{aligned} \frac{dM_z}{dt} &= (M_o - M_z)/T_1 \\ M_z &= M_o + C_z \exp\left(-t/T_1\right) \end{aligned}, \qquad [1.8]$$

where C_z is a constant of integration.

The magnetic moment of each nucleus contributes to the local magnetic field causing the net magnetic field at any point in space proximal to a group of spins to be the sum of $\mathbf{B}_o$ and the local magnetic field. As a result, each spin experiences a slightly different magnetic field and, according to Eq. [1.4], will precess at a slightly different frequency. This difference in resonant frequencies causes a loss of phase coherence among the spins and

therefore a decrease in the net transverse magnetization. Molecular motion is an important factor in the mechanism of spin-spin relaxation because the more a nuclei moves, the greater number of magnetic fields it will experience over time. This tends to average out the effect of local field variations.

In addition to molecular movement, transverse relaxation is also caused by interactions between spins. The net loss of the transverse magnetization components is called transverse relaxation, giving rise to an exponential decay of the transverse magnetization. This is described as

$$\begin{aligned} \frac{dM_x}{dt} &= -M_x \big/ T_2 \\ \frac{dM_y}{dt} &= -M_y \big/ T_2 \end{aligned}, \qquad [1.9]$$

and,

$$\begin{aligned} M_x &= C_x \exp\left(-t \big/ T_2\right) \\ M_y &= C_y \exp\left(-t \big/ T_2\right) \end{aligned}, \qquad [1.10]$$

where T_2 is the transverse relaxation time. Incorporating these descriptions of relaxation into the magnetic moment equations results in the Bloch equations:

$$\frac{d\mathrm{M}}{dt} = \begin{bmatrix} \dot{M}_x \\ \dot{M}_y \\ \dot{M}_z \end{bmatrix} = \begin{bmatrix} -M_x/T_2 - \Omega M_y + \omega_1 \sin(\phi) M_z \\ \Omega M_x - M_y/T_2 - \omega_1 \cos(\phi) M_z \\ -\omega_1 \sin(\phi) M_x + \omega_1 \cos(\phi) M_y + (M_o - M_z)/T_1 \end{bmatrix}. \quad [1.11]$$

Multiexponential T_2

The MR signal of a heterogeneous voxel is influenced by the individual properties of each constituent environment. The micro-environment of spinal cord WM includes two distinct water pools, the water trapped between the myelin bilayers and the water in the intra- and extra-axonal space. A diagram of these two water compartments is shown in Figure 1.2 where the k_{mie} represents the diffusion of water molecules from the myelin to

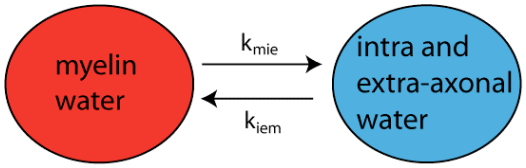

Figure 1.2 – Diagram of water exchange in white matter

the intra- and extra-axonal compartments and k_{iem} represents the opposite path of diffusion. The MR signal expected from a WM voxel is the sum of the two components' individual signals described by

$$S_{WM} = M_o^{mye} e^{-T_E/T_2^{mye}} + M_o^{ie} e^{-T_E/T_2^{ie}}, \quad [1.12]$$

where M_o^{mye} and T_2^{mye} are the signal contribution and T_2 of the myelin and M_o^{ie} and T_2^{ie} are the signal contribution and T_2 of the intra- and extra-axonal compartment. Equation 1.12 holds if the compartments are in slow exchange.

Effect of Water Exchange on MET$_2$

The measured MET$_2$ signal is a reflection the local molecular structure as well as motion within a heterogeneous tissue. Observation of unique relaxation times depends on the Brownian motion of the ^{1}H's within and between tissue compartments. These WM spins can exist between the myelin bilayers or in the intra- or extra-axonal space. The time spent within a certain compartment is defined as the lifetime. The effects of spin exchange between compartments has been explored by Woessner [30] based on simulations performed by Zimmermian and Brittain [31] using a general case for biexponential relaxation. Application of this theory to the biology of spinal cord WM is useful in the examination of the effects of water exchange on the MET$_2$ signal expected from rat spinal cord *in vitro*. With the presence of water exchange between the compartments, the measured WM signal from Eq. [1.12] is

$$M_T(t) = M_o^{'ie} e^{-T_E / T_2^{'ie}} + M_o^{'mye} e^{-T_E / T_2^{'mye}}, \qquad [1.13]$$

where the prime symbols signify the apparent (or observable) relaxation times and signal fractions. These can be related to the inherent properties of the spins [30] to examine the

effects of exchange on the observed signal. The results of numerical simulations are shown in Figure 1.3. The lifetime of the spins in the intra- and extra-axonal space, τ_{ie}, is gradually decreased, simulating faster water exchange between the myelin and intra- and

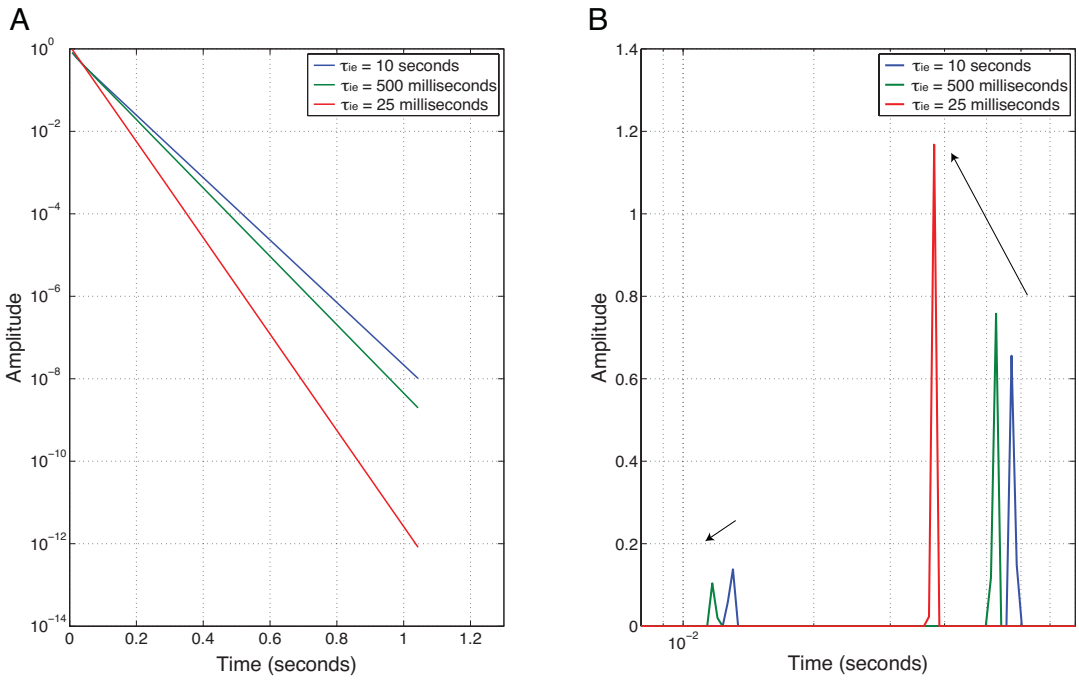

Figure 1.3 – A) MET_2 relaxation curves incorporating the effects of water exchange for spinal cord WM and B) corresponding MET_2 spectra following NNLS decomposition. M_o^{mye} was set at 0.2, M_o^{ie} was 0.8, T_2^{mye} and T_2^{ie} were

extra-axonal compartments. The faster water exchange results in a decrease in the $T_2^{'mye}$ and a concomitant decrease in $M_o^{'mye}$. When the τ_{ie} is decreased to a value $\approx T_2^{'mye}$, the myelin component is not detected (red line). These simulations demonstrate that in the presence of fast exchange the apparent relaxation decay curve can differ significantly.

Magnetization Transfer

The longitudinal magnetization is also influenced by a mechanism known as magnetization transfer (MT). MT is the MR phenomenon in which spins in two or more distinct environments exchange their magnetization via cross-relaxation and/or chemical exchange. In a two-pool tissue model protons may exist in a highly mobile liquid state associated with water (free pool comprised of intra-axonal and extra-cellular space) or in semisolid macromolecular sites, of relatively restricted motion, such as protein matrices or cell membranes (macromolecular pool of myelin). Figure 1.4 builds on the previous idea of water exchange related to T_2 to incorporate the magnetization transfer occurring in WM

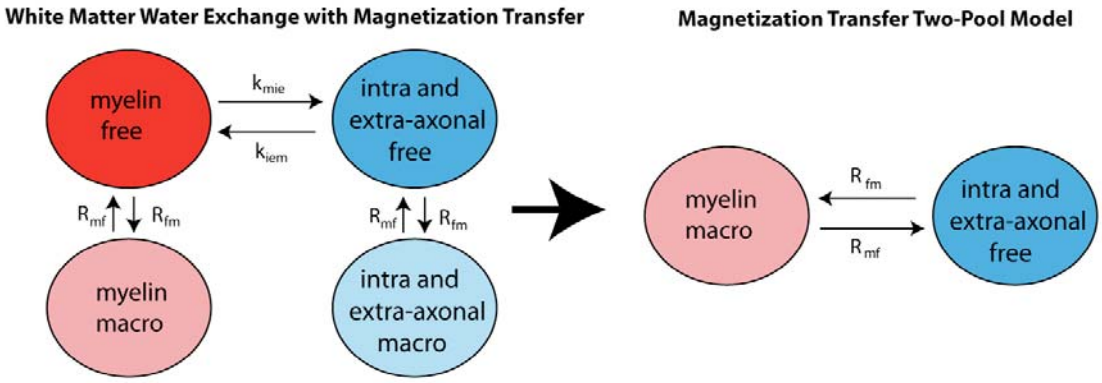

Figure 1.4 – Diagram of water exchange and magnetization transfer in white matter

between the free and macromolecular pools. The four pools pictured on the left in Figure 1.4 can be simplified into two pools for the case of MT as shown on the right. The dipole interactions leading to energy transitions described previously constitute this phenomenon. These dipole interactions don't necessarily need to be between water ^{1}H nuclei, but can also involve a wide range of ^{1}H nuclei from larger and less mobile molecules. Although these protons exhibit a transverse relaxation time too short to observe directly with MRI, they influence the magnetization of water ^{1}H through an exchange of magnetization. An off-resonance *rf* pulse can be applied to saturate the protons associated with the macromolecular pool. Following this pulse, the saturated macromolecular protons interact with the free proton pool via dipole coupling and/or chemical exchange. This causes a decrease in the MR signal in areas of macromolecules affected by magnetization transfer.

Measurement and Signal Analysis

Image Generation

The application of an *rf* pulse (B_1) results in the net magnetization, **M**, to rotate from the z-axis through some angle, called the tip-angle. This rotation of the **M** vector is governed by Eqs. [1.5] and [1.6]. If this tip-angle is 90^{o}, the **M** vector will rotate into the transverse plane. The phase angle, ϕ, defines the axis to which $\mathbf{B}_1$ is aligned in the rotating frame if the off-resonance frequency is zero ($\Omega = 0$). The typical *rf* excitation pulse refers

to a 90^o B_1 pulse with ϕ of 0 so that it is aligned along the x-axis. The result of such a pulse is to rotate the **M** vector from the z-axis to the –y-axis.

The net magnetic moment, **M**, will produce a signal when this $\mathbf{B}_1$ pulse is applied using hardware called an RF coil. This coil can also be used to receive the signal given off by the oscillating **M** due to the principle of reciprocity. The signal is received in the form of an oscillating magnetic field, inducing a current in the coil. This current does not contain any spatial information about **M**. In order to obtain spatial information about the sample, magnetic fields that vary spatially called magnetic gradients are added to $\mathbf{B}_o$. In order to obtain 3-dimensional spatial information, three orthogonal magnetic field gradients are applied along the x,y,and z-axes in the laboratory frame. The images for this dissertation were acquired using the technique called *spin-warp* imaging [32]. This method begins with slice selection, followed by phase encoding, and then read encoding to obtain information from the three axes.

Slice selection is achieved by turning on one of the three gradients, called the slice gradient, in conjunction with the B_1 pulse. The B_1 pulse is applied over a wide range of frequencies, defined by the *rf* bandwidth. The result of the slice gradient is that the spins' resonant frequencies will vary based on their location within the 'slice plane'. The *rf* bandwidth of the slice gradient limits the excitation of the B_1 pulse to those spins in the slice containing resonant frequencies within this bandwidth. The read encoding is accomplished by acquiring the resonance frequencies across the slice in one direction by applying another gradient, the read gradient, resulting in a limited bandwidth signal that maps the spins to the spatial domain in the read direction. The phase encoding is achieved by applying a pulsed gradient before acquisition that temporarily changes the frequencies

linearly across the phase direction. This results in a spatially dependent phase for each spin. The repeated application of the slice, read, then phase-encoding gradients with varying amplitudes of the phase-encode gradient will result in a signal reflecting the spatial location of the spins based on its frequency and phase of precession. An array of data (K_1xK_2) with K_1 corresponding to the number of phase encoding steps and K_2 corresponding to the number of samples per acquisition will be acquired. This data can be Fourier transformed to produce an image.

Measuring T_2

According to the Bloch equations, M_T decays exponentially at the rate of $1/T_2$. In practice, simply measuring the decay of M_T will not result in an accurate estimate of T_2. This obstacle is due to inevitable static field inhomogeneities that cause spins to precess at different rates. The effects of these inhomogeneities result in the observed M_T to decay at a more rapid rate called T_2^*. This can be corrected by using a specific method of signal acquisition called a *spin-echo* sequence.

The spin-echo sequence begins by first exciting the spins into the transverse plane using a 90^o *rf* pulse. This is then followed by a waiting period of τ_{SE} to allow for dephasing. After the time τ_{SE} has elapsed, a 180^o *rf* pulse is applied flipping all of the magnetization in the transverse plane and effectively reversing their phase. At a time of $2\tau_{SE}$ an echo will form. This time of $2\tau_{SE}$ is referred to as the echo time (T_E). This refocusing can be applied many times to create an echo train and is called the Carr-Purcell (CP) method [33]. This method was modified by Meiboom-Gill (MG) [34] to establish the CPMG

method of measuring T_2. The measured echoes from the CPMG sequence can be fitted to an exponential decay,

$$M_T(nT_E) = M_T(2n\tau_{SE}) = M_o \exp\left(^{-2n\tau_{SE}}/_{T_2}\right), \qquad [1.14]$$

where *n* is the echo number and $T_E = 2\tau_{SE}$.

In practice, the spin-echo approach still suffers from B_o and B_1 inhomogeneities, preventing perfect refocusing pulses. In the case of an imperfect B_1, the *rf* pulse will not effectively rotate all spins in the sample. When the refocusing pulses are not perfect, the echo decay is corrupted, causing inaccurate estimation of T_2. These imperfections must be removed in order to achieve accurate T_2 measurements. The application of gradient spoilers was used in the presented work to remove the unwanted magnetization from the multi-echo pulse sequence. Each *rf* refocusing pulse is surrounded by two identical gradient pulses causing the spins that experience a perfect 180° pulse to be rephased by

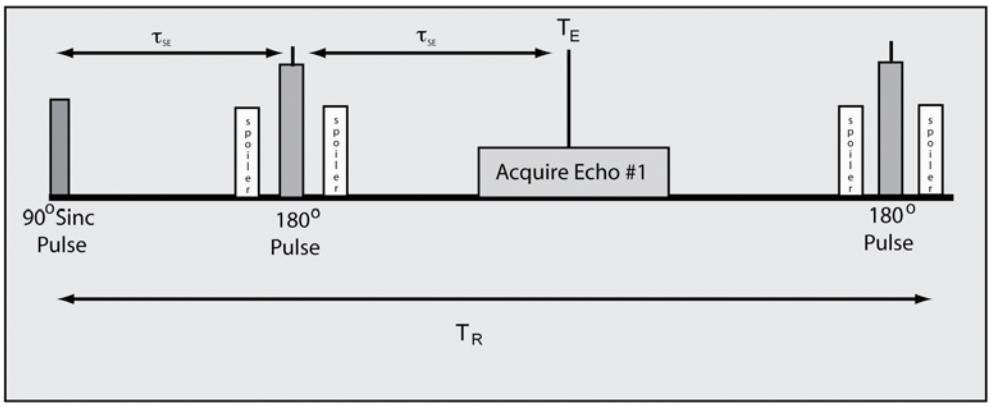

Figure 1.5 – Multi-echo, single-slice pulse

the second gradient and the spins that experienced an imperfect 180^o pulse to be dephased and not contribute to the echo [35, 36]. Using these gradient pairs in multi-echo imaging, the strengths and/or direction must be adjusted to avoid undesirable rephasing of magnetization by subsequent gradient pairs. A composite 90_x-180_y-90_x RF pulse was used in the multi-echo imaging in this work [37] to more effectively refocus magnetization in the presence of B_1 and B_o inhomogeneities. The multi-echo, single slice sequence used to acquire multiexponential T_2 data can be found in Figure 1.5.

Fitting of T_2 Data

In a simple scenario when a sample is homogeneous, the T_2 fitting process is straightforward. As discussed previously, the microenvironment in white matter is heterogeneous on a subvoxel scale resulting in a multiexponential T_2 decay. This multiexponential transverse decay makes a monoexponential model unfit for estimating the T_2 of white matter. The various environments for water to exist in white matter requires the signal from white matter be fit to more than one T_2 component. The preferred method is to fit the signal decay to an unspecified number of exponentials using the non-negative, least-squares (NNLS) method [38, 39]. This fitting technique uses the NNLS method to fit to a range of T_2 values resulting in a T_2 spectrum given by the solution of

$$\mathbf{y}=\mathbf{AS} \qquad [1.15]$$

for **S** where **y** is an N-element column vector of the measured echo amplitudes and **A** is an NxK matrix of all possible exponential terms. The variable **A** is described as

$$A = \exp\left(\begin{bmatrix} (-t_o/T_o) & (-t_o/T_1) & \cdots & (-t_o/T_k) \\ (-t_1/T_o) & \ddots & & (-t_1/T_k) \\ \vdots & & \ddots & \vdots \\ (-t_N/T_o) & (-t_N/T_1) & \cdots & (-t_N/T_K) \end{bmatrix}\right) \qquad [1.16]$$

where **S** is the T_2 spectra and **y** is a particular vector of multi-echo data. A minimum energy constraint is incorporated into an (N+K)xK **A** matrix as a KxK diagonal sub-matrix of terms λ:

$$A = \exp\left(\begin{bmatrix} (-t_o/T_o) & (-t_o/T_1) & \cdots & (-t_o/T_K) \\ (-t_1/T_o) & \ddots & & (-t_1/T_K) \\ \vdots & & & \\ (-t_N/T_o) & (-t_N/T_1) & \cdots & (-t_N/T_K) \\ \lambda & 0 & \cdots & 0 \\ 0 & \lambda & \ddots & \vdots \\ \vdots & \ddots & \ddots & 0 \\ 0 & \cdots & 0 & \lambda \end{bmatrix}\right) \qquad [1.17]$$

[38, 40]. The raw data vector, **y**, is then padded with zeroes to the dimensions of (N+K)x1. The scalar λ must be adjusted iteratively until the fit is statistically satisfactory, a condition determined by the χ^2 statistic. It can be used to adjust the continuous fit based on a restriction to the T_2 distributions. This requires the most appropriate solutions to be the simplest (least complex). This term forces neighboring points in the T_2 spectrum to be

close to each other and rejects solutions with a large number of peaks. The λ essentially smoothes the T_2 distribution as the cost of the χ^2 misfit, altering the discrete characteristics of the basic least squares solution. If the χ^2 is too small, the data will be fit too accurately and structure that is merely an artifact of the noise will be evident. Conversely, if the χ^2 is too large, the data are not fit closely enough and information will be lost. If λ is chosen carefully, a more robust fit will result in the presence of noise [41]. This can provide smooth solutions that better represent the T_2 distribution from the tissue microstructure.

Magnetization Transfer Measurement

The macromolecular pool's transverse relaxation is extremely fast compared to that of the free liquid pool. Another way to think of this is that the macromolecular ^1H absorption line width is much broader than the absorption line width of the free ^1H. It is possible to take advantage of this by applying a B_1 pulse with a large Ω (far off resonance) to affect the macromolecular pool more than the free pool. The general approach to quantifying MT is to apply such a $\mathbf{B}_1$ field off resonance that will rapidly saturate the magnetization of the macromolecular pool. Image contrast based on MT can be obtained by taking the ratio of the magnetization with and without the off-resonance saturation pulse (magnetization transfer ratio, MTR.) These measurements are sensitive to the effects of dipolar interactions and chemical exchange between the free pool and the macromolecular pool, but are highly scanner-dependent. In addition, the line-shape of the macromolecular pool must be known [42].

Quantitative magnetization transfer (qMT) methods have been developed by various groups [42-46]. A particular method proposed by Gochberg and Gore [47], uses a modification to Gochberg's original spectroscopy sequence [48] to enable imaging of the sample. It allows measurement of physical parameters such as size of macromolecular pool and spin exchange rates between the pools (R_{fm} and R_{mf}), as well as directly quantifying free water protons. This qMT sequence uses the method of selective inversion recovery (SIR) to selectively invert the free pool ^1H using only low power pulses. As the free and macromolecular pools undergo dipole interactions and/or chemical exchange, the addition of the macromolecular pool's magnetization to the inverted free pool has a substantial impact on the recovery of the signal. The resulting signal is biexponential function fit to

$$\frac{M_f(t)}{M_{f\infty}} = b_f^+ \exp\left(-R_1^+ t\right) + b_f^- \exp\left(-R_1^- t\right) + 1, \qquad [1.18]$$

where

$$2R_1^{\pm} = R_{1f} + R_{1m} + k_{fm} + k_{mf} \pm \sqrt{\left(R_{1f} - R_{1m} + k_{fm} - k_{mf}\right)^2 + 4k_{fm}k_{mf}}$$
$$b_f^{\pm} = \pm \frac{\left[\frac{M_f(0)}{M_{f\infty}} - 1\right]\left(R_{1f} - R_1^{\pm}\right) + \left[\frac{M_f(0)}{M_{f\infty}} - \frac{M_m(0)}{M_{m\infty}}\right]k_{fm}}{R_1^+ - R_1^-}, \qquad [1.19]$$

where R_1^- and R_1^+ are the slow and fast recovery rates with amplitudes b_f^- and b_f^+. The subscripts *f* and *m* refer to the free and macromolecular proton pools, respectively. $M_f(t)$ and $M_m(t)$ are the longitudinal magnetizations at time *t* whose equilibrium values are

$M_{f\infty}$ and $M_{m\infty}$. The R_1 values are the longitudinal relaxation rates when no MT exists between them. k_{fm} is the MT rate from the free to the macromolecular pool, k_{mf} is the reverse rate, and k_{fm}/k_{mf} is the pool size ratio (PSR) [49]. At the end of each repetition, both the macromolecular and free water pools have a longitudinal magnetization, M_z, of zero. The M_f is nulled due to a 90^o pulse along with a series of refocusing 180^o pulses preventing any T_1 recovery. The spins of the macromolecular pool are nulled because they are not affected by the low-power 90^o pulse, but are pulled toward the nulled M_f by the MT effect. If the M_f are held at zero for a certain time period, the M_m will be nulled [47]. Another benefit of this method is that the analysis is independent of the macromolecular pool line-shape. A pulse sequence diagram can be found in Figure 1.6. The qMT method proves to be a useful tool to examine the micro-anatomical characteristics of myelin.

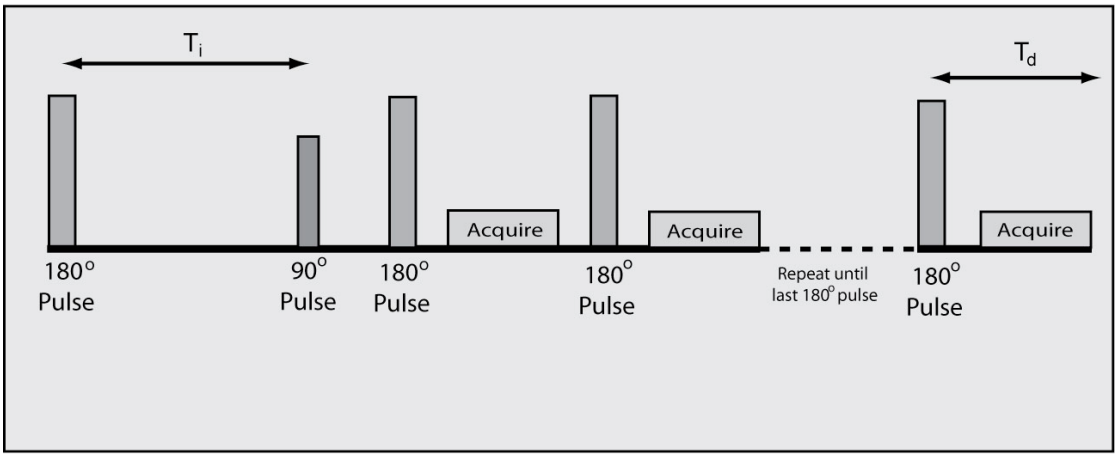

Figure 1.6 –pulse sequence used to acquire quantitative magnetization transfer data.

MRI of White Matter

Magnetic resonance imaging is a common method for quantification of white matter properties in the central nervous system. Multiexponential T_2 decay has been consistently demonstrated in WM of the spinal cord [50-52]. The fitted M_o values can be normalized to sum to one, resulting in an estimate for the relative signal fraction arising from each component. The normalized M_o of the component arising from the myelin compartment is referred to as the myelin water fraction (MWF). Minty et al. [52] found two T_2 components in excised and in vivo human spinal cord at 3 Tesla, revealing a myelin T_2 = 16 ms and a relative myelin fraction of 30.7%. This estimate of the MWF is substantially higher than those made in guinea pig spinal cord [50] or bovine brain [53], but they do agree with similar measures in bovine optic nerve, 32% ± 3% [54] and in vivo measurements of human cervical spine, 26.8% ± 2% [55]. The variation of the MWF based on the longitudinal location in the human spinal cord in vivo is still unresolved. It has been demonstrated to vary [51, 56], but the results conflict with the axon/myelin relationship proposed by Lubinska [57].

The biological basis of both MT and MET_2 imaging methods has been previously studied [50, 58-63]. Those examining the MT of white matter reveal a parallel between inflammation and changes in the MT parameters [58-60], indicating inflammatory-related changes are at the root of MT measurement changes. The underlying myelin characteristics have also been related to MET_2 measurements, and there is good evidence that the short T_2 component is proportional to the amount of myelin in the tissue [50, 61-63]. The MWF has been found to consistently decrease with demyelination and corresponding increase in water content [61, 63-65]. Knowledge of the specific origin of

the MWF and quantitative MT (PSR) measurements could elucidate the physiological characteristics of the tissue being imaged, aiding in diagnosis and monitoring of disease treatment.

Exploration of the covariance between the MWF and MTR [58, 61] as well as between MWF and PSR [58, 61, 64, 66-68] in white matter has been done with varying results. A complete lack of correlation was found by Gareau [58], Vavasour [61], and Laule [68], indicating these MR methods are measuring different attributes of the myelin microstructure. Studies have shown that MET_2 in animal models are more specific than the MT measurements in indicating the myelin content in tissue [58, 69-71]. The composite nature of the MT measurement may explain the lack of correlation found with the MET_2 results. A significant correlation coefficient may be seen with a larger sample size or more quantitative measures of MT. It is hypothesized that knowledge of the relationship between the MET_2 measurements and quantitative MT measurements could elucidate the physiological basis of each respective technique.

The presented study aims to quantify the MR characteristics of excised rat spinal cord, with specific interest in the MWF, as well as the qMT property of PSR and relate these results to the myelin characteristics determined by quantitative histology. It is hypothesized that the myelin content measurements based on MET_2 imaging are not only a reflection of the myelin water fraction in the region of interest, but are also related to the local myelin thickness. As the myelin thickness increases, the restriction of the myelin-associated spins will increase. This increase in myelin thickness will limit the exchange between the two compartments therefore improving the accuracy of the MWF estimate.

References

1. McDonald, W.I. and G.D. Ohlrich, *Quantitative anatomical measurements on single isolated fibres from the cat spinal cord.* Journal of Anatomy, 1971. **110**(2): p. 191-202.

2. Fraher, J.P. and J.P. Rossiter, *Myelin-axon relationships established by rat vagal schwann cells deep to the brainstem surface.* Journal of Comparative Neurology, 1991. **304**: p. 253-260.

3. Rushton, W.A.H., *A theory of the effects of fibre size in medullated nerve.* Journal of Physiology London, 1951. **115**: p. 101-122.

4. Williams, P.L. and C.P. Wendell-Smith, *Some additional parametric variations between peripheral nerve fibre populations.* Journal of Anatomy, 1971. **109**(3): p. 505-526.

5. Samorajski, T. and R.L. Friede, *A quantitative electron microscopic study of myelination in the pyramidal tract of rat.* Journal of Comparative Neurology, 1968. **134**: p. 323-338.

6. Waxman, S.G. and M.L.V. Bennett, *Relative conduction velocities of small myelinated and non-myelinated fibres in the central nervous system.* Nature (London), 1972. **238**: p. 217-219.

7. Waxman, S.G. and H.A. Swadlow, *Ultrastructure of visual callosal axons in the rabbit.* Experimental Neurology, 1976. **53**: p. 115-127.

8. Gasser, H.S. and H. Grundfest, *Axon diameters in relation to the spike dimensions and conduction velocity in mammalian A fibres.* American Journal of Physiology, 1939. **127**: p. 393-414.

9. Sanders, F.K., *The thickness of myelin sheaths of normal and regenerating peripheral nerve fibre.* Proceedings of royal society B, 1948. **135**: p. 323-357.

10. Schmitt, F.O. and R.S. Bear, *The optical properties of vertebrate nerve axons as related to fibres size.* Journal of cell comparative physiology, 1937. **9**: p. 261-273.

11. Taylor, G.W., *The correlation between sheath birefringuence and conduction velocity with special reference to cat nerve fibres.* Journal of cell comparative physiology, 1942. **20**: p. 359-372.

12. Fraher, J.P., *Myelin-axon relationships in the rat phrenic nerve: longitudinal variation and lateral asymmetry.* Journal of Comparative Neurology, 1992. **323**: p. 551-557.

13. Friede, R.L. and T. Samorajki, *Relation between the number of myelin lamellae and axon circumference in fibers of vagus and sciatic nerves of mice.* Journal of Comparative Neurology, 1967. **130**: p. 223-232.

14. Fraher, J.P., *Quantitative studies on the maturation of central and peripheral parts of individual ventral motoneuron axons. I. Myelin sheath and axon calibre.* Journal of Anatomy, 1978. **126 (Pt 3)**: p. 509-533.

15. Fraher, J.P. and G.F. Kaar, *The development of alpha and gamma motoneuron fibres in the rat. II. A comparative ultrastructural study of their central and peripheral myelination.* Journal of Anatomy, 1985. **141**: p. 89-103.

16. Fabricius, C., C.H. Berthold, and M. Rydmark, *Dimensions of individual aplpha and gamma motor fibers in the ventral funiculus of the cat spinal cord.* Journal of Anatomy, 1994. **184**(2): p. 319-33.

17. Hess, A. and J.Z. Young, *The Nodes of Ranvier in the central nervous system.* Journal of Physiology, 1952. **108**(3): p. 52.

18. Lubinska, L. and J. Waryszewska, *Fibre population of the phrenic nerve of rat: changes of myelinated fibre dimensions along the nerve and characteristics of axonal branchings.* Acat. Neurobiol. Exp., 1974. **34**(525-541).

19. Schwartz, E.D., et al., *Ex vivo evaluation of ADC values within spinal cord white matter tracts.* American Journal of Neuroradiology, 2005. **26**(2): p. 390-397.

20. Gullapalli, J., J. Krejza, and E.D. Schwartz, *In vivo DTI evaluation of white matter tracts in rat spinal cord.* Journal of Magnetic Resonance Imaging, 2006. **24**(1): p. 231-234.

21. Madi, S., K.M. Hasan, and P.A. Narayana, *Diffusion tensor imaging of in vivo and excised rat spinal cord at 7 T with an icosahedral encoding scheme.* Magnetic Resonance in Medicine, 2005. **53**(1): p. 118-125.

22. Glauert, A.M., *Practical methods in electron microscopy*. Vol. 3 part 1. 1974, North-Holland, Amsterdam.

23. Van Harreveld, A. and F.I. Khattab, *Perfusion fixation with gluteraldehyde and post-fixation with osmium tetroxide for electron microscopy.* Journal of Cell Science, 1968. **3**: p. 579-594.

24. Hildebrand, C. and H. Muller, *Low angle X-ray diffraction studies on the period of central myelin sheaths during preparation for electron microscopy.* Neurobiology, 1974. **4**: p. 71-81.

25. Karnovsky, M.J., *A Formaldehyde-Glutaraldehyde Fixative of High Osmolality for Use in Electron Microscopy.* Journal of Cell Biology, 1965. **27**(2): p. A137.

26. Feirabend, H.K.P., H. Choufoer, and S. Ploeger, *Preservation and staining of myelinated nerve fibers.* Methods, 1998. **15**(2): p. 123-131.

27. Bloch, F., W.W. Hansen, and M. Packard, *Nuclear Induction.* Phys. Rev., 1946. **69**: p. 127.

28. Purcell, E.M., H.C. Torrey, and R.V. Pound, *Resonance absorption by nuclear magnetic moments in a solid.* Phys. Rev., 1946. **69**: p. 37.

29. Lauterbur, P.C., *Image Formation by Induced Local Interactions - Examples Employing Nuclear Magnetic-Resonance.* Nature, 1973. **242**(5394): p. 190-191.

30. Woessner, D.E., *Brownian motion and its effects in NMR chemical exchange and relaxation in liquids.* Concepts in Magnetic Resonance, 1996. **8**(6): p. 397-421.

31. Zimmerman, J.R. and W.E. Brittin, *Nuclear Magnetic Resonance Studies in Multiple Phase Systems: Lifetime of a Water Molecule in an Adsorbing Phase on Silica Gel.* Journal of Phys. Chem., 1957. **61**: p. 1328 - 1333.

32. Edelstein, W.A., et al., *Spin warp NMR imaging and applications to human whole-body imaging.* Phys. Med. Biol., 1980. **25**: p. 751-756.

33. Carr, H.Y. and E.M. Purcell, *Effects of diffusion on free precession in nuclear magnetic resonance experiments.* Phys. Rev., 1954. **94**: p. 630-638.

34. Meiboom, S. and D. GIll, *Modified spin-echo method for measuring nuclear relaxation times.* Rev. Sci. Instr., 1958. **29**: p. 688-691.

35. Madjumar, S., et al., *Errors in the measurment of T2 using multiple-echo MRI techniques. I. Effects of radiofrequency pulse imperfection.* Magn Reson Med, 1986. **3**: p. 397.

36. Poon, C.S. and R.M. Henkelman, *Practical T2 quantitation for analysis of multicomponent tissue T2 relaxation data.* Journal of Magnetic Resonance Imaging, 1992. **2**(5): p. 541-553.

37. Levitt, M.H. and R. Freeman, *Compensation for pulse imperfections in NMR spin-echo esperiments.* Journal of Magnetic Resonance, 1981. **43**: p. 65.

38. Whittall, K.P., M.J. Bronskill, and R.M. Henkelman, *Investigation of analysis techniques for complicated NMR relaxation data.* Journal of Magnetic Resonance, 1991. **84**: p. 134.

39. Whittall, K.P. and A.L. MacKay, *Quantitative Interpretation of NMR Relaxation Data.* Journal of Magnetic Resonance, 1989. **84**: p. 134-152.

40. Whittall, K.P., et al., *In vivo Measurement of T2 Distributions and Water Contents in Normal Human Brain.* Magnetic Resonance in Medicine, 1997. **37**(1): p. 34-43.

41. Stewart, W.A., et al., *Spin-spin Relaxation in Experimental Allergic Encephalomyelitis. Analysis of CPMG Data Using a Non-linear Least Squares Method and Linear Inverse Theory.* Magnetic Resonance in Medicine, 1993. **29**(6): p. 767-775.

42. Henkelman, R.M., et al., *Quantitative interpretation of magnetization transfer.* Magnetic Resonance in Medicine, 1993. **29**(6): p. 759-766.

43. Edzes, H.T. and E.T. Samulski, *Cross Relaxation and Spin Diffusion in Proton Nmr of Hydrated Collagen.* Nature, 1977. **265**(5594): p. 521-523.

44. Edzes, H.T. and E.T. Samulski, *Measurement of Cross-Relaxation Effects in Proton Nmr Spin-Lattice Relaxation of Water in Biological-Systems - Hydrated Collagen and Muscle.* Journal of Magnetic Resonance, 1978. **31**(2): p. 207-229.

45. Morris, G.A. and A.J. Freemont, *Direct Observation of the Magnetization Exchange Dynamics Responsible for Magnetization Transfer Contrast in Human Cartilage Invitro.* Magnetic Resonance in Medicine, 1992. **28**(1): p. 97-104.

46. Wolff, S.D. and R.S. Balaban, *Magnetization Transfer Contrast (Mtc) and Tissue Water Proton Relaxation Invivo.* Magnetic Resonance in Medicine, 1989. **10**(1): p. 135-144.

47. Gochberg, D.F. and J.C. Gore, *Quantitative imaging of magnetization transfer using an inversion recovery sequence.* Magnetic Resonance in Medicine, 2003. **49**: p. 501-505.

48. Gochberg, D.F., R.P. Kennan, and J.C. Gore, *Quantitative studies of magnetization transfer by selective excitation and T1 recovery.* Magnetic Resonance in Medicine, 1997. **38**(2): p. 224-231.

49. Gochberg, D.F. and J.C. Gore, *Quantitative magnetization transfer imaging via selective inversion recovery with short repetition times.* Magnetic Resonance in Medicine, 2007. **57**: p. 437-441.

50. Stewart, W.A. and e. al., *Spin-Spin Relaxation in Experimental Allergic Encephalomyelitis - Analysis of Cpmg Data Using a Nonlinear Least-Squares Method and Linear Invers-Theory.* Magnetic Resonance in Medicine, 1993. **29**(6): p. 767-775.

51. Minty, E.P., A.L. MacKay, and K.P. Whittall. *Measurement of Myelin Water in Human and Bovine Spinal Cord*. in *ISMRM*. 2002. Honolulu, Hawaii.

52. Minty, E.P., *Myelin water measurement in the spinal cord*, in *Physics*. 2005, University of Alberta: Edmonton, Alberta, Canada. p. 119.

53. Vavasour, I.M., *Physics*. 1998: University of British Columbia: Vancouver. 124.

54. Stanisz, G.J., et al., *Characterizing white matter with magnetization transfer and T-2*. Magnetic Resonance in Medicine, 1999. **42**(6): p. 1128-1136.

55. Wu, Y., et al., *Myelin water fraction in human cervical spinal cord in vivo.* Journal of Comput Assist Tomogr, 2006. **30**: p. 304-306.

56. Yung, A.C. and e. al. *Measurements of myelin water in rat spinal cord in vivo.* in *ISMRM*. 2004. Kyoto, Japan.

57. Lubinska, L. and J. Waryszewska, *Fibre population of the phrenic nerve of rat: Changes of myelinated fibre dimenstions along the nerve and characteristics of axonal branchings.* Acta Neurobiol. Exp., 1974. **34**: p. 524-541.

58. Gareau, P.J., et al., *Magnetization transfer and multicomponent T2 relaxation measurements with histopathologic correlation in an experimental model of MS.* Journal of Magnetic Resonance Imaging, 2000. **11**(6): p. 586-595.

59. Fillippi, M., et al., *Short-term evolution of individual enhancing multiple sclerosis lesions studied with magnetization transfer imaging.* Magnetic Resonance Imaging, 1999. **17**: p. 979-984.

60. Dousset, V., R.I. Grossman, and K.N. Ramer, *Experimental allergic encephalomyelitis and multiple sclerosis: lesion characterization with magnetization transfer imaging.* Radiology, 1992. **182**: p. 483-491.

61. Vavasour, I.M., et al., *A comparison between magnetization transfer ratios and myelin water percentages in normals and multiple sclerosis patients.* Magnetic Resonance in Medicine, 1998. **40**(5): p. 763-768.

62. Menon, R.S. and P.S. Allen, *Application of Continuous Relaxation-Time Distributions to the Fitting of Data from Model Systems and Excised Tissue.* Magnetic Resonance in Medicine, 1991. **20**(2): p. 214-227.

63. Mackay, A., et al., *In-Vivo Visualization of Myelin Water in Brain by Magnetic-Resonance.* Magnetic Resonance in Medicine, 1994. **31**(6): p. 673-677.

64. Laule, C., et al., *Water content and myelin water fraction in multiple sclerosis - A T-2 relaxation study.* Journal of Neurology, 2004. **251**(3): p. 284-293.

65. Laule, C., et al., *Myelin water imaging in multiple sclerosis: quantitative correlations with histopathology.* Multiple Sclerosis, 2006. **12**: p. 747-753.

66. Tozer, D.J., et al., *Correlation of apparent myelin measures obtained in multiple sclerosis patients and controls from magnetization transfer and multicompartmental T-2 analysis.* Magnetic Resonance in Medicine, 2005. **53**(6): p. 1415-1422.

67. Sled, J.G., et al., *Regional variations in normal brain shown by quantitative magnetization transfer imaging.* Magnetic Resonance in Medicine, 2004. **51**: p. 299-303.

68. Laule, C., et al. *Correlation between magnetization transfer ratio and myelin water content in normal white matter and MS lesions.* in *Proceedings of the annual meeting of the international society for magnetic resonance in medicine*. 2002. Honolulu, Hawaii.

69. Gareau, P.J., et al., *In vivo measurements of multi-component T-2 relaxation behaviour in guinea pig brain.* Magnetic Resonance Imaging, 1999. **17**(9): p. 1319-1325.

70. Stanisz, G.J., et al., *MR properties of excised neural tissue following experimentally induced inflammation.* Magnetic Resonance in Medicine, 2004. **51**(3): p. 473-479.

71. Moore, G.R.W., et al., *The short T2 component is absent in chronically demyelinated plaques in formalin-fixed multiple sclerosis brain.* Neurology, 1999. **52**(6): p. A567-A567.

CHAPTER II

SIMULATIONS FOR OPTIMAL MET_2 MEASUREMENT

Introduction

Magnetic resonance imaging serves as a modality for the investigation of white matter in the nervous system. One of the primary goals of a well-conducted MRI experiment is to obtain enough signal relative to the noise (as measured by the ratio of voxel signal to the noise standard deviation, or the signal to noise ratio, SNR) to examine the tissue of interest. The noise present in an image depends on the imaging parameters of the experiment. The term imaging parameters refers to those factors that can be chosen in an experiment and are not intrinsic properties of the sample. These include factors such as T_R, T_E, sweepwidth (SW), number of averages (N_{aq}), as well as voxel and matrix sizes.

The NMR signal from heterogeneous tissue such as white matter is the spatial sum over the microstructures existing in the voxel defined by the spatial encoding and allowed by the SNR. The T_2 of white matter in the nervous system has been characterized using multiexponential analysis [1-9]. These studies have identified two major exponentials present in the T_2 decay for white matter. The component with the longer T_2 is believed to originate from the intra and extra-axonal water, while the component with the shorter T_2 originates from the myelin water. Quantification of the MET_2 behavior in WM could provide insight into pathologies that result in alterations to neural microanatomy, including demyelination.

In order to quantify MET_2 arising from the microscopic compartition of water in WM the pulse sequence for multi-echo (ME) imaging must be optimized. The accuracy of MET_2 quantification using MRI has been addressed in several publications [10-13] which identified sources of error and proposed pulse-sequence solutions. The common conclusion of these studies was that accurate measurement of MET_2 is complicated by the inability to generate precise RF refocusing pulses as well as static and B_1 field inhomogeneities. These errors can be addressed by using broadband RF refocusing pulses or even composite hard pulses that are designed to further improve the accuracy of refocusing in presence of B_1 and B_o spatial variation [14, 15]. However in most imaging situations the refocusing is far from perfect, creating unwanted signal, which can be eliminated using spoiler gradients such as those proposed by Poon and Henkelman [13]. The theoretical requirements of these gradients to successfully eliminate all unwanted signal often surpass the capabilities of the gradient coils, often imposing limitations on the imaging parameters.

Obtaining reliable MET_2 information requires high quality T_2 decays. The relaxation times and sizes of the components extracted from MET_2 data are excessively sensitive to noise. The SNR requirements stem from the ability to detect the shorter T_2^{mye} peak in the T_2 spectrum. The noise in MET_2 has been found to be non-Gaussian [16] and/or echo-dependent [5, 16]. SNR requirements have been addressed by Graham et al. [17], who found that the minimum acceptable standard deviation of the noise is 1% of the signal strength at the shortest echo time in order to obtain meaningful MET_2 data. Beaulieu et al. [18] aimed to provide more definitive evidence of compartmentalization in nerve water T_2. They used an echo sampling of 1.6 ms, resulting in an SNR of 3000. He was able to

resolve components with a minimum factor of two between the component relaxation times. Kroeker and Henkelman [19] used simulated and experimental data from aqueous solutions to examine the relaxation measurements of two component models similar to WM. They found that for an SNR of 150, samples with relaxation values separated by less than a factor of three were not resolved in continuous fits.

The SNR is also affected by the echo sampling times. Many studies have examined the window for MET_2 data acquisition [17, 20-25]. Fenrich et al. [23] found when the data acquisition window approaches the value of the transverse relaxation, broadening of the peak close to that extremity occurs, resulting in a loss of precision. They found that the minimum acquisition window giving optimal precision was $0.75*T_{2,short} - 2*T_{2,long}$. Whittall et al. [25] highlights the increased sensitivity to the noise as the number of echoes is decreased. Some suggest that the resolution varies as $SNR/\sqrt{N_E}$, where N_E is the number of echoes sampled [17, 20, 21, 24]. But Fenrich et al. found that the resolution degraded more rapidly than $SNR/\sqrt{N_E}$ [22]. Graham et al. have highlighted how the relationship between $SNR/\sqrt{N_E}$ and the abilities to resolve components depends on where those components are relative to each other in time, indicating tissue dependence [17]. Finally, the spacing of the echoes has been examined by Shrager et al. [26] revealing nonlinear echo spacing valuable in specific biexponential conditions. Does and Gore [27] further examined the application of nonlinear echo spacing, including practical aspects of imaging such as the effects of imperfect refocusing and inhomogeneity of the magnetic fields concluding linear echo spacing to be more appropriate for investigation of MET_2. However, even under optimal echo acquisition conditions, the SNR is usually far more important determinant of precision than data acquisition window limitations.

The estimation of multiexponential T_2 relaxation measurements in biological samples is dependent on the model used to interpret the NMR data. The most common approach is to fit with the smallest number of exponentials which provide a satisfactory representation of the data, but this becomes inaccurate when there are more than 2-3 terms or when any two time constants are similar [28]. Kroeker and Henkelman recognized that in biological samples the signal's approach to equilibrium reflected a distribution of relaxation times due to the water protons' range of environments [29]. They used a linear inversion technique to solve the model of the signal's return to equilibrium that is based on a least squares approach developed by Provencher [30, 31]. Nonlinear optimization techniques are also applied [32, 33] but usually require a starting estimate from which to begin iterating and are vulnerable to converging on a local instead of a global minimum. This technique has also been used by Menon [5] to reproduce known relaxation time distributions from data on a controllable model system. Due to the number of *a priori* assumptions necessary when using the nonlinear techniques, typical MET_2 processing [7, 18, 29-31, 34] involves the use of the linear inversion program based on the least squares approach [19].

Whittall and MacKay [28] have used a NNLS approach based on an algorithm of Lawson and Hanson [35] to derive a continuous solution from multi-echo data. Using this approach, they have avoided the *a priori* assumptions about the number of components as well as their nature. This method is highly dependent on the SNR of the ME data and will sample from an extensive range of solutions if the SNR is low.

The continuous distribution fit has also been applied unregularized by MacKay to estimate *in vivo* T_2 distributions of WM on volunteers with multiple sclerosis [4]. The

unregularized method provides enhanced admissibility [17], which is defined as the percentage of T_2 distributions with the correct number of components. This method constrains the fit according to the χ^2. One method is to use a constant χ^2 by adjusting λ iteratively, allowing the T_2 distributions from different data sets to be compared effectively [17]. Constraining χ^2 within the range of 1.02% - 1.025% produces more robust solutions than those from least squares NNLS [5, 19, 28].

The fitting technique has been shown to impact not only the admissibility but also the detection of MET_2 based on peak separation. Some groups have found that relaxation values must be at least a factor of two apart for reliable separation [5, 21]. But Stewart et al. [7] have found that with doped water samples that the fits were inaccurate when the T_2 times differ by less than a factor of three. In addition, Graham found that equally weighted components are easier to resolve than if one component dominates the signal [17].

Data acquisition parameters of particular interest are the SW and the corresponding minimum T_E ($T_{E,min}$). Exploration of the relationship between the data acquisition time (proportional to the SW) and the minimum T_E permitted can aid in selection of appropriate MET_2 acquisition parameters. Reducing the SW will bring improvements in the SNR, but will also cause the $T_{E,min}$ to be longer. This tradeoff must be examined in respect to MWF quantification using MET_2 to uncover the point at which the relationship between SW and $T_{E,min}$ will cancel out the benefits of smaller T_E.

Optimal choices for ME acquisition parameters will improve the fidelity of MET_2 characterization and provide a clear standard for implementation of ME pulse sequences.

This study aims to determine these appropriate imaging parameters in order to improve the level of confidence in the MET_2 measurements for application to WM.

Methods

Biexponential T_2 decay curves were generated using MATLAB (R2006a, Mathworks, Natick, MA) to simulate signals expected from CNS white matter. T_2 decays were generated using Eq. [2.1],

$$M_T = M_o^{mye} e^{-T_E / T_2^{mye}} + M_o^{ie} e^{-T_E / T_2^{ie}} + \varepsilon(0,\sigma_n), \qquad [2.1]$$

where the superscripts *mye* and *ie* denote distinct tissue compartments, myelin and intra- and extra-axonal, from which the signal components arise. Random Gaussian noise was added to each generated signal, denoted in Eq. [2.1] by ε, with a mean of zero and standard deviation of σ_n. The simulation loop was cycled 50,000 times for all discussed studies. In order to make the MET_2 simulations applicable to the T_2^{mye}, it was necessary to consider the range of imaging parameters expected to be sensitive to this component [6, 9, 16]. The simulation parameters addressed in this study included T_2^{mye} of 10, 15, and 20 milliseconds, T_2^{ie} of 40, 60, and 80 milliseconds, $T_{E,min}$ from 5.5 – 30 ms, and SNR from 250 - 2000. The relation between the SW and required $T_{E,min}$ for the multi-echo, single-slice imaging sequence can be found in Figure 2.1, these $T_{E,min}$ values were used for all further analysis.

The choice of fitting technique for MET_2 data is very important in terms of image processing time as well as preservation of data quality. A series of regularized and unregularized simulations were performed. The regularized smoothing technique from Graham et al. [17] was used with smoothing at 2.5% for parameters at 1.5 T. The bias (β_{MWF}) and standard deviation (σ_{MWF}) of the MWF were examined to ensure comparable fits resulted, justifying the use of the quicker, unregularized fit.

The next step in choosing the optimal processing technique involves addressing the NNLS fitting domain. The algorithm chosen fits the decay to a continuous distribution of exponentials, which can either be fixed for all studies or vary based on the T_E value. MET_2 data was generated using Eq. [2.1] for both a constant fitting domain of 5 millisecondss to 1 second as well as a variable fitting domain ($T_{E,min}(1) – 2*T_{E,min}(32)$).

Adequate sampling for the T_2^{ie} component of white matter was ensured. The simulations used a constant N_E of 52, with 32 initial echoes at a spacing of $T_{E,min}$ followed by 20 late echoes spaced at 50 milliseconds. Since N_E is held constant, the $T_{E,min}$ will determine the extent of echo train acquisition. The shortest $T_{E,min}$ considered, 5.5 ms, will sample up to 5.5 ms * 32 echoes = 176 ms for the early echoes, then 176 + 20 * 50 ms = 1.176 seconds, adequately sampling the longer T_2 component [36]. The longest $T_{E,min}$ considered will sample the echo train up to 1.96 seconds. Batch simulations were performed using the unregularized fitting technique, constant fitting domain, and 52 echoes with a varying $T_{E,min}$ to examine the effects of inadequately sampling the long T_2 component.

Simulations varying the $T_{E,min}$ were performed for an M_o^{mye} of 0.2 and different component T_2 values to examine the effects of SW on the MWF estimate. The results are reported in terms of the SNR_{MWF} which is defined as

$$SNR_{MWF} = {}^{MWF}\!/_{\sigma_{MWF}}. \quad [2.2]$$

Results

The $T_{E,min}$ permitted at varying sweepwidth values is plotted in Figure 2.1. As the SW increases, the minimum T_E allowed decreases. The tradeoff between these parameters and its effect on MET_2 characterization of white matter is based on this relation, characteristic of the imaging sequence.

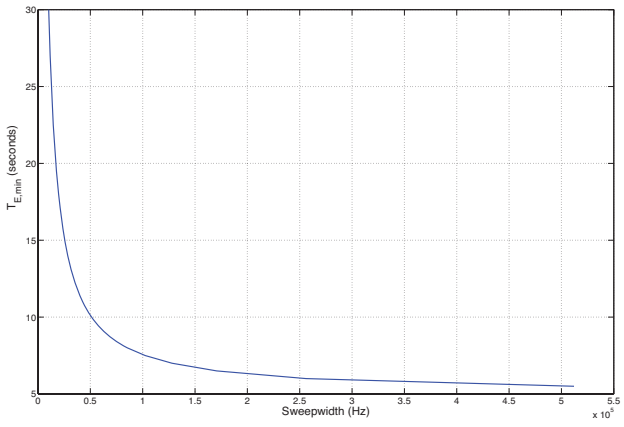

Figure 2.1 – Relationship between sweepwidth and minimum T_E for multi-echo, single slice imaging sequence.

The results of the comparison between unregularized and least-squares smoothing [17] at 2.5% can be found in Figure 2.2. The β_{MWF} and σ_{MWF} are shown for both fitting techniques and the results indicate that smoothing can reduce σ_{MWF} and doesn't influence

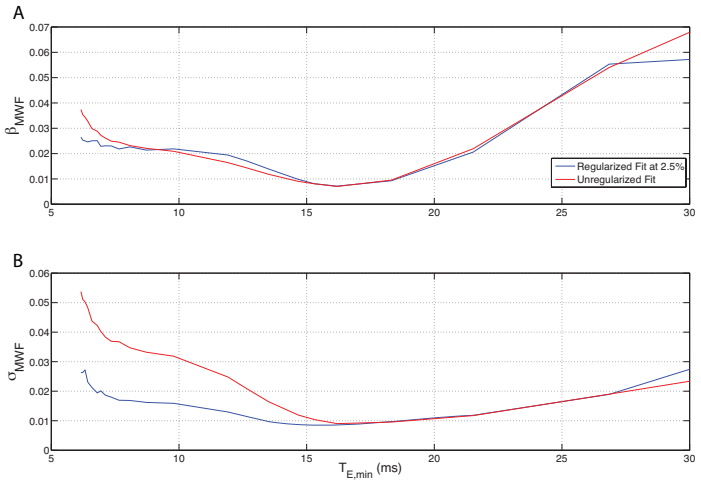

Figure 2.2 – The A) bias and B) standard deviation of the MWF for regularized (blue) versus non-regularized (red) processing techniques

β_{MWF}, but both techniques exhibit the same trends. The unregularized fitting technique was used for all further studies.

Figure 2.3 shows the comparison of the constant and variable fitting domains using an unregularized NNLS fitting technique. These results show the differences between the variable and constant fitting domains. No significant difference is seen for the range of $T_{E,min}$ values of concern for application to WM, hence the more efficient constant fitting domain was used in all further processing.

The effects of echo train length on the characterization of the T_2^{ie} component appear in Figure 2.4. The trends all begin with high $\sigma_{M_0^{ie}}$ values due to under-sampling of the T_2^{ie} component. Distinct minima exist for each case based on the T_2 values of the two components.

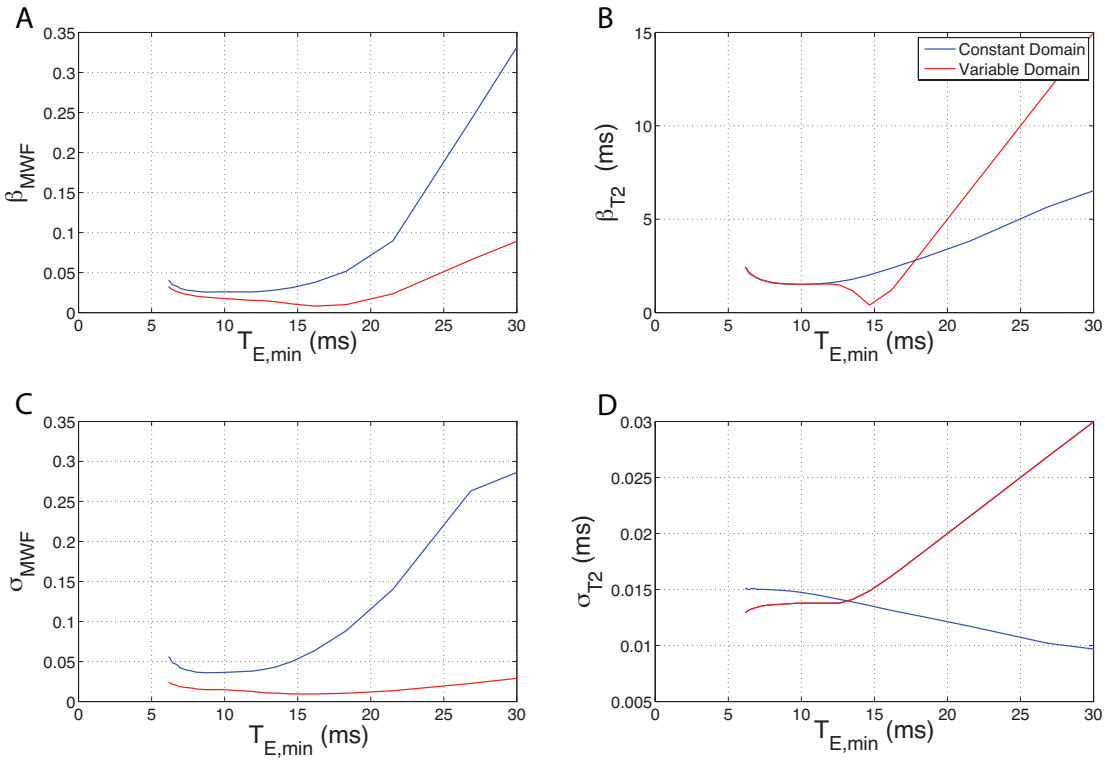

Figure 2.3 – The A) bias and C) standard deviation of the myelin water fraction and the B) bias and D) standard deviation of the myelin T_2 simulated signals decomposed using a constant and variable fitting domain.

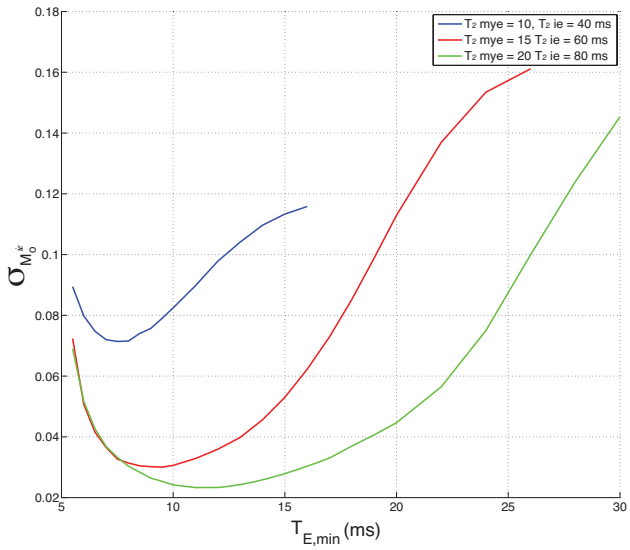

Figure 2.4 – The $\sigma_{M_0^{ie}}$ for varying T_2^{mye} and T_2^{ie} values.

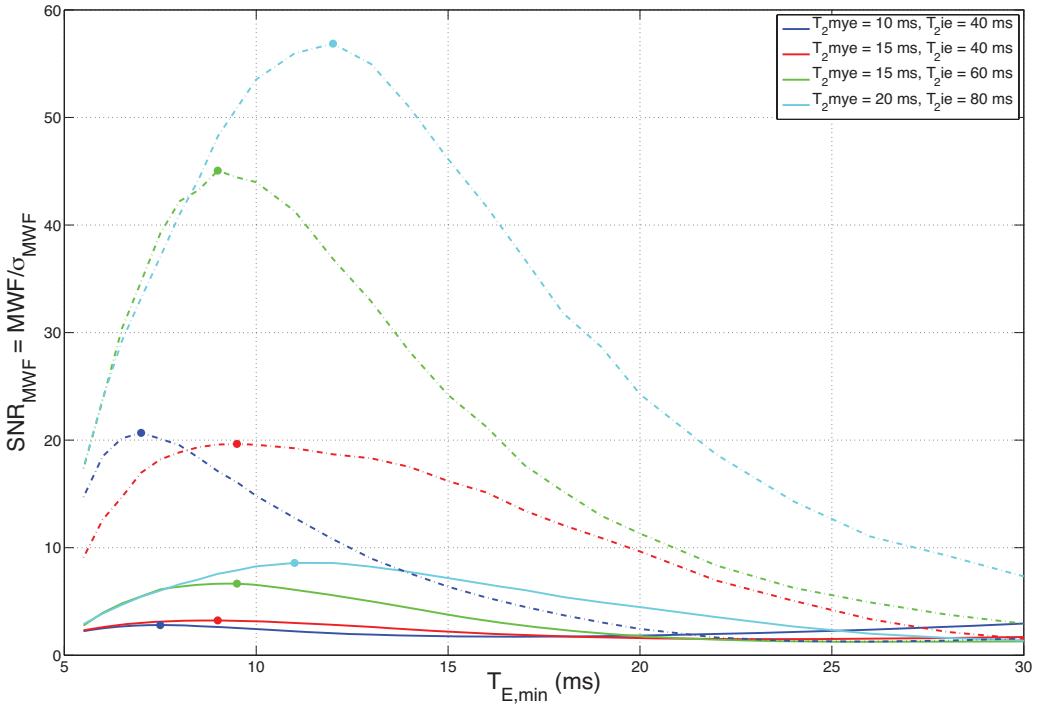

Figure 2.5 – The calculated SNR_{MWF} as a function of $T_{E,min}$ for an SNR of 250 (solid lines) and 2000 (dashed lines).

The results of batch simulations can be found in Figure 2.5, highlighting the SNR_{MWF} peaks for optimal $T_{E,min}$ values. The solid lines represent an SNR of 250 while the dashed lines represent and SNR of 2000. Maxima of SNR_{MWF} are indicated with a circle.

Disscussion

Specific imaging parameters were found to exist significantly improving the ability to characterize the MET_2 of WM. The simulations performed demonstrated a distinct $T_{E,min}$ and SW value exist for the best MWF estimate.

Previous studies have used simulations to assess the accuracy of MET_2 analysis and the minimum signal to noise ratios necessary to precisely measure the myelin component [17, 23, 24, 28, 37]. T_2 Decay curves must have high SNR values with the minimum acceptable noise standard deviation being approximately 1% of the signal at the first echo time [17, 23]. It has been shown that the NNLS can accurately find T_2 peaks at high SNR but falls apart at lower SNR values [37, 38], with significant errors in T_2 estimation found at SNR values lower than 250 [37]. It is essential to obtain a high-fidelity T_2 decay curve in order to ensure meaningful T_2-spectral data, particularly when attempting to quantify a short T_2 and small signal contribution such as myelin.

It is known that a decrease in SW will bring improvements in SNR, but will also cause the $T_{E,min}$ to increase, hindering the characterization of the shorter myelin component. The echo spacing is commonly minimized in order to characterize the T_2^{mye}. Graham et al. [17] determined that any T_E value can be chosen as long as the shorter T_2 is adequately sampled. It is also important to adequately sample the longer T_2 component. The trends in

Figure 2.4 demonstrate the difficulty in characterizing the longer T_2 component with short T_E values. The $\sigma_{M_0^{ie}}$ was initially high for the short $T_{E,min}$ simulations then decreased to an optimal $T_{E,min}$ for MET_2 acquisition between 7 and 12 milliseconds.

Table 2.1 - Potential loss in SNR_{MWF} resulting from incorrect T_2 estimates

Estimated T_2 Values	Optimal $T_{E,min}$	SNR_{MWF}	Actual T_2 Values	SNR_{MWF} Lost
T_2^{mye} = 10 ms T_2^{ie} = 40 ms	7.5 ms	2.8	T_2^{mye} = 20 ms T_2^{ie} = 80 ms	30%
T_2^{mye} = 15 ms T_2^{ie} = 40 ms	9.0 ms	3.2	T_2^{mye} = 20 ms T_2^{ie} = 80 ms	11.70%
T_2^{mye} = 15 ms T_2^{ie} = 40 ms	9.0 ms	3.2	T_2^{mye} = 10 ms T_2^{ie} = 40 ms	5.70%

It was interesting to find that the $T_{E,min}$ where the minimum of the standard deviation of estimated MWF occurred was not necessarily the shortest T_E possible. When simulating various combinations of T_2^{mye} and T_2^{ie}, as seen in Figure 2.5, it was found that the maximum SNR_{MWF} was dependent on these combinations as well as the SNR of the MET_2 signal. Previous studies have also found this dependence on the tissue's T_2 properties [5, 17, 21]. The dashed lines in Figure 2.5 represent an SNR of 2000 while the solid lines are an SNR of 250. The $T_{E,min}$ corresponding to the maximum SNR_{MWF} changes for the different SNR values, but not significantly or consistently. On the other hand, variation in the SNR_{MWF} due to the T_2^{mye} and T_2^{ie} combinations could significantly affect the results of an experiment. A priori knowledge of the T_2 component values could

prevent a significant loss of SNR_{MWF}. For example, at an SNR ≈250, if the T_2^{mye} was estimated at 10 ms and T_2^{ie} was estimated at 40 ms the optimal $T_{E,min}$ of 7.5 ms is chosen according to Figure 2.5. If the actual T_2^{mye} is 20 ms and T_2^{ie} is 80 ms, the choice of 7.5 ms for $T_{E,min}$ would result in a loss of 30% of the potential SNR_{MWF}. Table 2.1 describes some possible situations in which the T_2 component values are estimated incorrectly and the resulting loss of potential SNR_{MWF}. This loss of SNR_{MWF} is concerning since the component only comprises a relatively small fraction of the signal and the fitting techniques typically require a robust SNR_{MWF} to be reliable. Despite these potential effects, all of the optimal $T_{E,min}$ values fell between 7.5 and 12 milliseconds for a SNR ≈ 250.

Conclusions

Simulations were used to investigate data requirements for multicomponent T_2 analysis under experimental conditions common for research MRI scanners. Sweepwidth and minimum T_E combinations were found over a range of typical parameters for optimal MET_2 quantification of myelin. The simulation results indicate minimization of echo spacing is not always the optimal choice when attempting to quantify the fraction of the myelin water component. The optimal SNR_{MWF} is not significantly dependent on the SNR of the signal but does vary based on the T_2^{mye} and T_2^{ie} values.

References

1. Does, M.D. and R.E. Snyder, *Multiexponential T-2 relaxation in degenerating peripheral nerve.* Magnetic Resonance in Medicine, 1996. **35**(2): p. 207-213.

2. Gareau, P.J., et al., *In vivo measurements of multi-component T-2 relaxation behaviour in guinea pig brain.* Magnetic Resonance Imaging, 1999. **17**(9): p. 1319-1325.

3. Harrison, R., M.J. Bronskill, and R.M. Henkelman, *Magnetization-Transfer and T-2 Relaxation Components in Tissue.* Magnetic Resonance in Medicine, 1995. **33**(4): p. 490-496.

4. Mackay, A., et al., *In-Vivo Visualization of Myelin Water in Brain by Magnetic-Resonance.* Magnetic Resonance in Medicine, 1994. **31**(6): p. 673-677.

5. Menon, R.S. and P.S. Allen, *Application of Continuous Relaxation-Time Distributions to the Fitting of Data from Model Systems and Excised Tissue.* Magnetic Resonance in Medicine, 1991. **20**(2): p. 214-227.

6. Peled, S., et al., *Water diffusion, T-2, and compartmentation in frog sciatic nerve.* Magnetic Resonance in Medicine, 1999. **42**(5): p. 911-918.

7. Stewart, W.A., et al., *Spin-spin Relaxation in Experimental Allergic Encephalomyelitis. Analysis of CPMG Data Using a Non-linear Least Squares Method and Linear Inverse Theory.* Magnetic Resonance in Medicine, 1993. **29**(6): p. 767-775.

8. Swift, T.J. and O.G.J. Fritz, *A Proton Spin-Echo Study of the State of Water in Frog Nerves.* Biophysics Journal, 1969. **9**: p. 54-59.

9. Vasilescu, V., et al., *Water Compartments in the Myelinated Nerve.* Experientia, 1977. **34**: p. 1443-1445.

10. Majumdar, S., et al., *An Estimation and Correction Scheme for System Imperfections in Multiple-Echo Magnetic-Resonance-Imaging.* Magnetic Resonance in Medicine, 1987. **4**(3): p. 203-220.

11. Majumdar, S., et al., *Errors in the Measurements of T2 Using Multiple-Echo Mri Techniques .2. Effects of Static-Field Inhomogeneity.* Magnetic Resonance in Medicine, 1986. **3**(4): p. 562-574.

12. Majumdar, S., et al., *Errors in the Measurements of T2 Using Multiple-Echo Mri Techniques .1. Effects of Radiofrequency Pulse Imperfections.* Magnetic Resonance in Medicine, 1986. **3**(3): p. 397-417.

13. Poon, C.S. and R.M. Henkelman, *Practical T2 Quantitation for Clinical-Applications.* Jmri-Journal of Magnetic Resonance Imaging, 1992. **2**(5): p. 541-553.

14. Levitt, M.H. and R. Freeman, *Compensation for Pulse Imperfections in Nmr Spin-Echo Experiments.* Journal of Magnetic Resonance, 1981. **43**(1): p. 65-80.

15. Poon, C.S. and R.M. Henkelman, *180o refocusing pulses which are insensitive to static and radiofrequency field inhomogeniety.* Journal of Magnetic Resonance, 1993. **99**: p. 45.

16. Does, M.D. and R.E. Snyder, *T-2 Relaxation of Peripheral-Nerve Measured in-Vivo.* Magnetic Resonance Imaging, 1995. **13**(4): p. 575-580.

17. Graham, S.J., P.L. Stanchev, and M.J. Bronskill, *Criteria for analysis of multicomponent tissue T-2 relaxation data.* Magnetic Resonance in Medicine, 1996. **35**(3): p. 370-378.

18. Beaulieu, C., F.R. Fenrich, and P.S. Allen, *Multicomponent water proton transverse relaxation and T-2-discriminated water diffusion in myelinated and nonmyelinated nerve.* Magnetic Resonance Imaging, 1998. **16**(10): p. 1201-1210.

19. Kroeker, R.M. and R.M. Henkelman, *Analysis of Biological Nmr Relaxation Data with Continuous Distributions of Relaxation-Times.* Journal of Magnetic Resonance, 1986. **69**(2): p. 218-235.

20. Backus, G. and F. Gilbert, *Uniqueness in Inversion of Inaccurate Gross Earth Data.* Philosophical Transactions of the Royal Society of London Series a-Mathematical and Physical Sciences, 1970. **266**(1173): p. 123-&.

21. Brown, R.J.S., *Information Available and Unavailable from Multiexponential Relaxation Data.* Journal of Magnetic Resonance, 1989. **82**(3): p. 539-561.

22. Fenrich, F.R.E., *A simulation and experimental stud of water proton relaxation in a white matter model*. 1992, University of Alberta.

23. Fenrich, F.R.E., C. Beaulieu, and P.S. Allen, *Relaxation times and microstructures.* NMR in Biomedicine, 2001. **14**(2): p. 133.

24. Whittall, K.P., M.J. Bronskill, and R.M. Henkelman, *Investigation of Analysis Techniques for Complicated Nmr Relaxation Data.* Journal of Magnetic Resonance, 1991. **95**(2): p. 221-234.

25. Whittall, K.P., A.L. MacKay, and D.K.B. Li, *Are mono-exponential fits to a few echoes sufficient to determine T-2 relaxation for in vivo human brain?* Magnetic Resonance in Medicine, 1999. **41**(6): p. 1255-1257.

26. Shrager, R.I., G.H. Weiss, and R.G.S. Spencer, *Optimal time spacings for T2 measurements: monoexponential and biexponential systems.* NMR in Biomedicine, 1998. **11**: p. 297-305.

27. Does, M.D. and J.C. Gore, *Complications of nonlinear echo time spacing for measurement of T-2.* Nmr in Biomedicine, 2000. **13**(1): p. 1-7.

28. Whittall, K.P. and A.L. MacKay, *Quantitative Interpretation of NMR Relaxation Data.* Journal of Magnetic Resonance, 1989. **84**: p. 134-152.

29. Kroeker, R.M., et al., *Continuous Distributions of Nmr Relaxation-Times Applied to Tumors before and after Therapy with X-Rays and Cyclophosphamide.* Magnetic Resonance in Medicine, 1988. **6**(1): p. 24-36.

30. Provencher, S.W., *Contin - a General-Purpose Constrained Regularization Program for Inverting Noisy Linear Algebraic and Integral-Equations.* Computer Physics Communications, 1982. **27**(3): p. 229-242.

31. Provencher, S.W., *A Constrained Regularization Method for Inverting Data Represented by Linear Algebraic or Integral-Equations.* Computer Physics Communications, 1982. **27**(3): p. 213-227.

32. Provencher, S.W., *Fourier Method for Analysis of Exponential Decay Curves.* Biophysical Journal, 1976. **16**(1): p. 27-41.

33. Smith, M.R. and S.T. Nichols, *Improved Resolution in the Analysis of Multicomponent Exponential Signals.* Nuclear Instruments & Methods in Physics Research, 1983. **205**(3): p. 479-483.

34. Graham, S.J. and M.J. Bronskill, *MR measurement of relative water content and multicomponent T-2 relaxation in human breast.* Magnetic Resonance in Medicine, 1996. **35**(5): p. 706-715.

35. Lawson, C.L. and R.J. Hanson, *Solving least squares problems.* 1974, Englewood Cliffs, NJ: Prentice-Hall.

36. Fenrich, F.R.E., *A simulation and experimental study of water proton relaxation in a white matter model.* 1992, University of Alberta.

37. Andrews, T., et al., *Testing the three-pool white matter model adapted for used with T2 relaxometry.* Magnetic Resonance in Medicine, 2005. **54**(2): p. 449-454.

38. Whittal KP, M.A., *Quantitative Interpretation of NMR Relaxation Data.* Journal of Magnetic Resonance, 1989. **84**: p. 134-152.

CHAPTER III

HISTOLOGICAL IMAGE PROCESSING

Introduction

Morphometric studies are valuable in the investigation of neural development and pathology. Histological examination of excised neural tissue allows measurements on individual cells resulting in useful parameters such as the fiber size, axon size, and myelin thickness. Accurate morphological measurements can be complicated by a number of issues. The variability of tissue staining intensity from sample to sample or even within different regions of the same tissue section requires sufficient robustness to these luminance changes. In addition, tracts with large fiber population may have a heterogeneous fiber distribution, which would introduce bias with the use of any sampling scheme. These measurements can be performed manually or with the aid of computer programs.

Manual morphometric fiber measurements are executed with the use of image-viewing software. The experimenter chooses fibers and manually measures parameters using image processing software. An unavoidable bias is introduced by the selection the experimenter makes from the entire fiber population. It must be stressed that the manual technique of measurement is subject to error sources such as sampling bias as well as inter-observer variability. In addition to these established error sources, manual measurement requires lengthy computation time. This time is dependent on the tissue cross sectional area and the fiber size population. The population sampling has been

varied in different studies. One group [1] found a good estimation of fiber parameters with less than 10% of the fibers measured, whereas another [2] claims that a minimum of 50% of the entire fiber population is needed for parameter estimations. As a consequence, an automated image analysis system is sought to avoid bias and sampling issues and to facilitate objective and efficient analysis.

Various degrees of automation exist to accomplish these measurements. Fully automated measurements are typically achieved with computerized image analysis systems that can be programmed to analyze the myelinated fibers using morphological recognition algorithms to isolate regions of interest in images. Numerous groups have used the contour model approach where physical properties of the axons along with image data are used in an optimization scheme to converge on axon boundaries [3-5]. Complete automation requires the ability to handle both local and structural analysis in one step. Often, these techniques are computationally expensive and prone to error.

A semi-automated approach could decrease the computational demands characteristic of fully automated techniques. Semi-automated methods involve the automated analysis of tissue with operator intervention to manually eliminate dark elements such as pericytes and glial cell nuclei. The present study proposes and evaluates a semi-automatic method for segmentation, recognition, and measurement of myelinated fiber parameters. The semi-automated results are compared to a manual measurement technique. The most commonly used morphometric parameters such as axon diameter and myelin thickness were considered.

Methods

Animal and Tissue Preparation

The spinal cord tissue used in this study was obtained from six Sprague Dawley rats (300-420 grams). The animals were sacrificed with inhaled CO_2. The spinal cord was immediately extracted using a saline filled syringe to apply pressure at the caudal end of the vertebral column. The excised spinal cord was separated into three longitudinal sections: cervical, thoracic, and caudal. These sections were immediately placed in 0.5% paraformaldehyde/4% gluteraldehyde in phosphate buffer, a solution found to optimally preserve the structure of myelin [6, 7]. Following 48 hours submersion in the fixative, the tissue sections were post-fixed in 1% osmium tetroxide in cacodylate buffer and dehydrated in graded ethanol. After epoxy resin embedding, the spinal cord was sectioned axially and stained with 1% toluidine blue solution.

Microscopy

Light microscopy was performed with a Leica DM IRB inverted microscope (Meyer Instruments, Inc., Houston, TX) using a 40 x 0.55 N Plan DIC air lens. Photomicrographs were captured using a DXM1200C (Nikon, Japan) with a 1024 x 1372 pixel resolution representing a 256 μm x 343 μm tissue area. A microscale was imaged in the same way to obtain the scaling factor. The pixel size corresponded to 0.25 μm. Five WM tracts were examined within the axial plane, delineated in Figure 3.1. A total of five images were taken for each of the three longitudinal sections of the spinal cord.

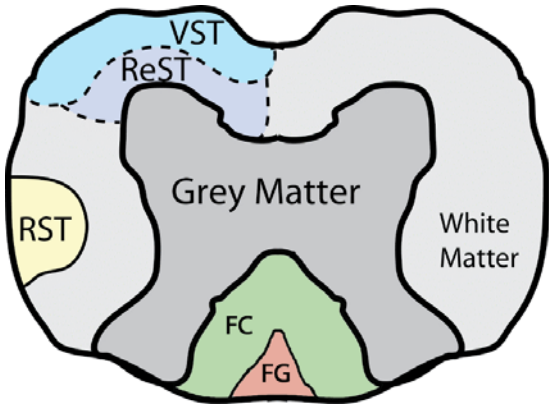

Figure 3.1 – Regions of interest rat spinal cord, FC = fasciculus cuneatus, FG = fasciculus gracilis, ReST = reticulospinal tract, RST = rubrospinal tract, VST = vestibulospinal tract

Semi-automated Morphometry

Semi-automated analysis was carried out using a set of image processing tools [8] developed in house for MATLAB software (The MathWorks Inc., Natick, MA). The program converts the color photomicrograph to a grayscale 8-bit image and applies an edge-preserving smoothing filter. User input is then required to determine the threshold values for a sigmoid function that is used to enhance the gradients of the image. The gradient magnitude is calculated for each pixel based on the user-defined threshold image. The software performs segmentation on the gradient image using a watershed algorithm. Global thresholds were set for axon circularity ($4\pi(\text{area}/\text{perimeter}^2)$ where circularity of 1 is a perfect circle) to avoid consideration of axons imaged at an oblique angle as well as extracellular space being considered as axon space. The segmented

watershed image is then analyzed resulting in an index for each identified axon. The centroid coordinates of the axon, axonal area, the axon's major and minor axes lengths, the eccentricity of the axonal ellipse, and radial statistics used to determine the myelin thickness measurements are calculated for each axon index. To obtain the radial statistics, eight radial lines are drawn from the center of each axon, and the myelin inner and outer boundaries are defined by a contrast change based on the sigmoid function threshold. This results in eight measurements of the myelin thickness around each axon.

Post processing of the semi-automated results converts the arbitrary pixel values to quantitative measurements based on the calibration of the microscale. The axon diameter was calculated by taking the mean of the major and minor axes. The minimum myelin thickness measurement was used in order to avoid overestimation of the myelin thickness caused by oblique or abutting axons.

Manual Morphometry

Manual measurements were accomplished using ImageJ software (NIH http://rsb.info.nih.gov/ij/). To determine the detection ability of the semi-automated technique, an entire photomicrograph was examined using the Cell Counter plug-in [9] to establish the number of axons present. The false positive rate was determined by examining the results of the semi-automated analysis and counting the number of extra-axonal spaces were considered as axons and dividing it by the total number of true axons determined using the manual cell counter.

For direct comparison with the semi-automated method, twenty individual axons were manually selected from a segment of the micrograph. Manual measurements were

performed on these 20 axons in the same manner as the semi-automated method, with major and minor axon axes averaged to obtain the axon diameter and the minimum of myelin thickness measured in eight locations around the axon. The manual and semi-automated measurements of these twenty axons were then compared on an axon-by-axon basis.

To further compare the results of reliable manual morphometry with those of the semi-automated analysis, one hundred axons were randomly chosen from the entire micrograph and the axon diameter and myelin thickness were measured manually. The axon selection was accomplished using the ImageJ Analyze Particles command following manual thresholding of the image. This resulted in an index for each detected circle on the micrograph. One hundred axons were randomly selected using Matlab's randperm command. Axon diameter and myelin thickness measurements were performed on each selected axon with myelin measured only once through the thinnest section of the sheath. The means of the axon diameter were compared to the mean values calculated by the semi-automated method and myelin thickness measurements were compared to that of the semi-automated method.

Results

All spinal cord sections included in this study showed good preservation of myelin and axonal structures. An example micrograph is shown in Figure 3.2.

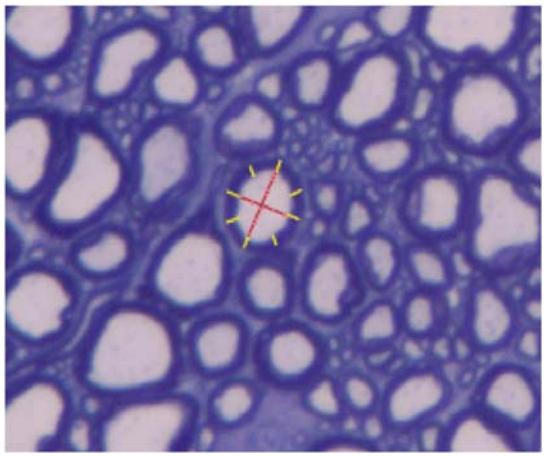

Figure 3.2 – Example of manual measures where yellow lines are myelin thickness measurements and red lines are major and minor axes.

Manual Morphometry

Photomicrographs of each ROI were examined manually using the ImageJ software. The semi-automatic method detected 3265 fibers, nearly all (98%) fibers found manually (3346). An example of the manual measurements used for direct comparison with the semi-automatic method is shown in Figure 3.2. Eight radial lines (yellow) were drawn through the axon; the mean of these measurements was considered the myelin thickness. Two axon diameters were drawn to estimate the major and minor axes of the axon; the mean of these two measurements is classically considered the axon diameter and was used as such in this part of the study.

Semi-automated Morphometry

Various steps of the semi-automated method are shown in Figure 3.3. Part A depicts a section of a typical photomicrograph acquired, part B shows an image following application of a sigmoid threshold with user defined limits, part C is a gradient magnitude

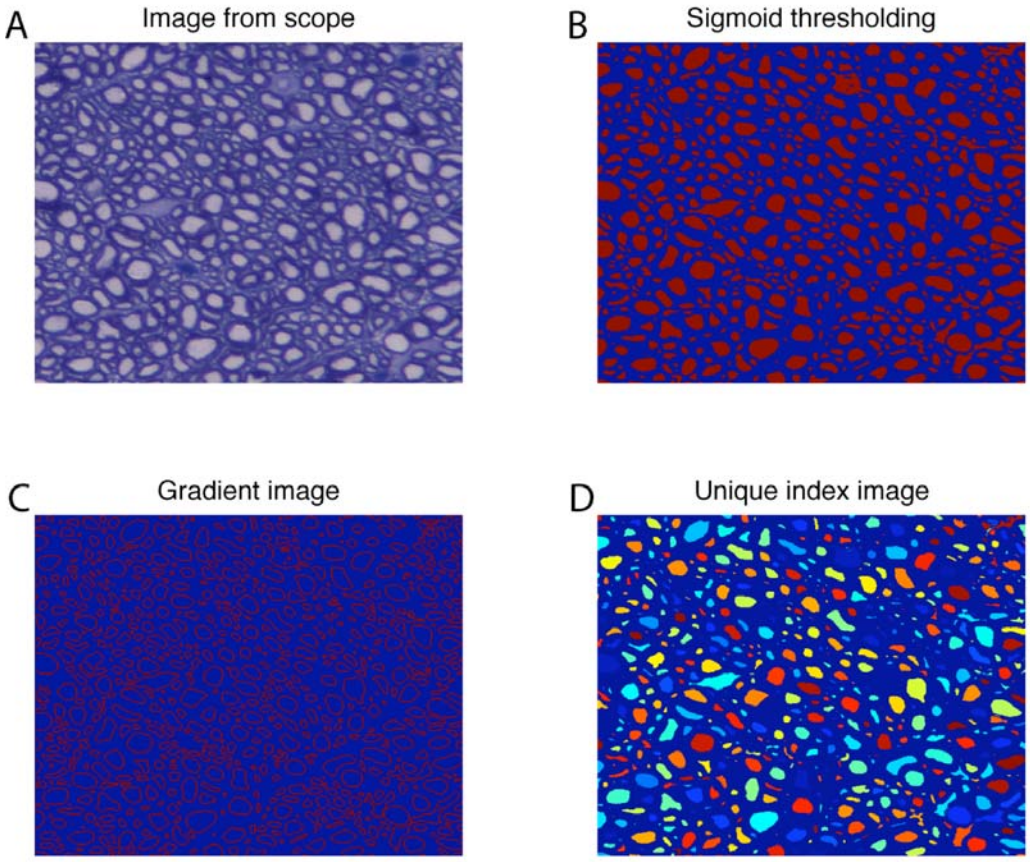

Figure 3.3 – Results from semi-automatic nerve analysis A) original histological image, B) image resulting from user-input, sigmoid thresholding, C) pixel gradient magnitude image, D) image resulting from segmentation of image C and performing a watershed segmentation algorithm resulting in a unique color index for each axon.

image, and part D is the result of segmentation by taking the gradient image and performing a watershed segmentation algorithm. It is important to note that in part D, each axon has a unique color index. The semi-automatic method detected 3265 fibers, nearly all (98%) fibers found manually. The false positive rate was less than 2.5%.

Direct Comparison of Methods

In Figure 3.4 the corresponding manual and semi-automatic histograms are depicted for the axon-by-axon myelin thickness measurements. The histograms do not differ significantly. The Pearson's χ^2 value for independence is 2.79, with approximate P value of 0.05. The semi-automatic and manual methods were correlated for both the myelin

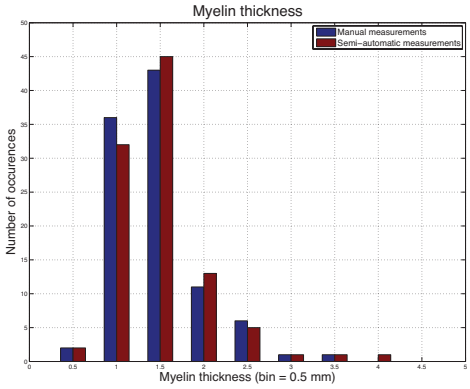

Figure 3.4 – Distribution comparison of semi-automatic and manual measures for equivalent fiber diameters for all ROIs.

thickness and axon diameter measurements. Figure 3.5 shows the semi-automatic measurements plotted against the manual measurements for both parameters on an axon-by-axon basis. The legend of each graph indicates the individual correlation coefficients

for each ROI while the overall correlation coefficient is 0.82 for the myelin thickness and 0.94 for the axon diameter.

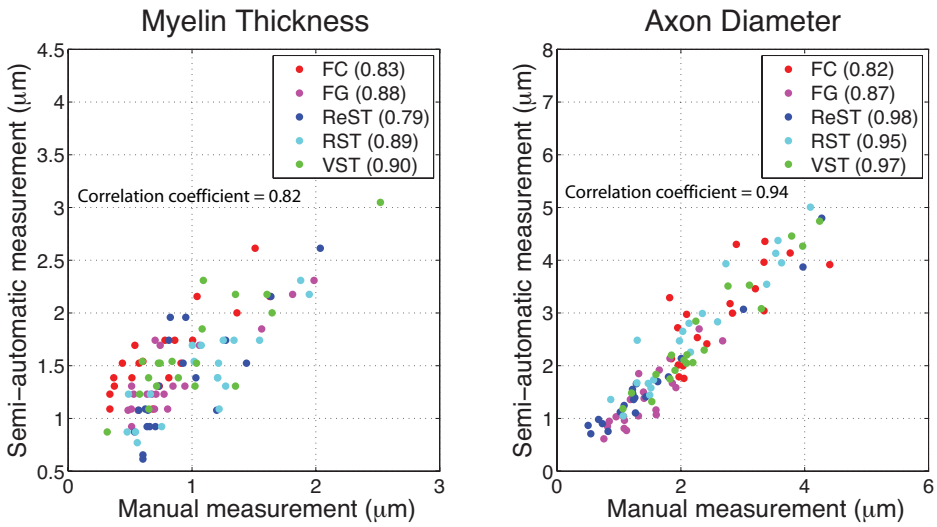

Figure 3.5 – Semi-automatic measurements plotted against manual measurements for both myelin thickness and axon diameter on an axon-by-axon basis. Correlation coefficients are shown in parentheses for each individual ROI while the overall correlation coefficient is printed above the data.

Indirect Comparison, Increased Sample Size

The larger-scale analysis of myelin thickness and axon diameter measures for manual versus semi-automatic measurements aimed to quantify the distributions of measurements resulting from each technique. A direct correlation could not be performed since there were only one hundred manual measures compared to varying numbers of semi-automated axons detected. A comparison of the mean of the distributions is shown in Figure 3.6. The dashed line indicates a linear fit to the entire data set. The semi-automatic technique tends to overestimate the myelin thickness and underestimate the

axon diameter, but not consistently, causing an obvious lack of correlation. This is demonstrated by the correlation coefficients of 0.16 for the myelin thickness measurements and 0.85 for the axon diameter measurements.

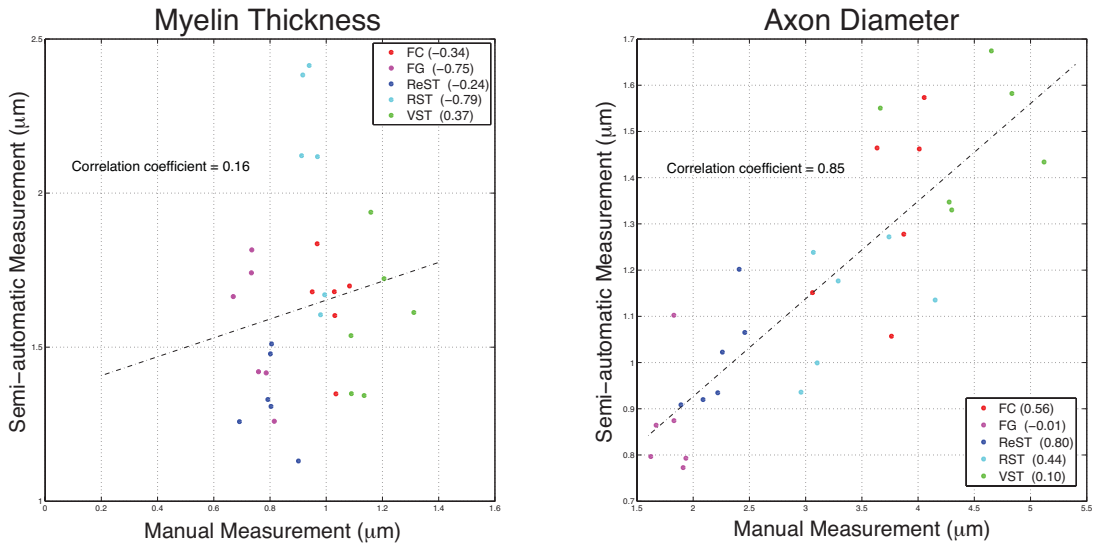

Figure 3.6 – The mean of semi-automatic measurements plotted against that of manual measurements for both myelin thickness and axon diameter. Correlation coefficients are shown in parentheses for each individual ROI while the overall correlation coefficient is printed above the data. The dashed line is indicates a linear fit.

Discussion

This study evaluates an efficient semi-automatic method to measure various fiber parameters such as the axon diameter and myelin thickness. Morphometric histological analysis has developed from time-consuming manual measurements to include the use of automatic programs. The semi-automatic program used in this study enables analysis of regions of interest in the rat spinal cord, which presents unique structural organization of central WM. The peripheral regions of the oval-shaped spinal cord contain the well-

organized white matter tracts surrounding a characteristic butterfly-shaped grey matter region. The parallel structure of the white matter tracts in the spinal cord facilitates analysis of their myelin properties. The ROIs delineated in Figure 3.1 were chosen based on the white matter structure in these areas, suggesting a difference in axon morphometry.

The detection rate of the semi-automatic method is an important issue when considering heterogeneous fiber populations such as those found in the spinal cord. The semi-automatic method detected 3265 fibers, nearly all (98%) fibers found manually (3346). The false positive rate was less than 2.5%, a negligible level originating from misclassification of extra-axonal spaces as intra-axonal space.

The manual morphometric measurements used for direct comparison was time-consuming, with 20 fiber measurements taking over 40 minutes due to the 8 radial lines drawn for each myelin thickness measurement and two axes drawn for each axon diameter measurement. The semi-automatic method presented in this manuscript achieved comprehensive analysis of each photomicrograph (3000+ measurements) in about 40 minutes following user intervention. The experimenter must initially load an image and manually adjust the threshold values, which are applied globally to the entire micrograph. These values are saved and the program proceeds to calculate axon counts, measurements, myelin thickness, perimeter, and eccentricity measurements for each identified fiber.

Initially, the measurement techniques were compared directly on an axon-by-axon basis sampled from a small area of the micrograph. The manual myelin thickness measurements were acquired such that the resulting parameters would be similar to those

produced by the semi-automatic method. The minima of the eight manual measures were used to obtain the final myelin thickness measure. This approach ensured myelin from other axons was not being included in calculations, a problem which could be specifically avoided in the manual measurement technique.

Figure 3.5 supports the use of the semi-automated technique to obtain morphometric parameters from nervous tissue. Regardless of strong correlation coefficients, this direct comparison only considered a small area of the entire micrograph and expanding that area to include the entire micrograph could confound the effects of non-uniform staining and difficulties setting the threshold values. Consideration of results from the semi-automated method from a random sample of the entire micrograph is in order.

Despite the promising axon-by-axon results discussed above, the semi-automated method was further examined with an increased sample size. One hundred manual measurements of myelin thickness and axon diameter were acquired for each cervical spine micrograph. The axons were chosen systematically in order to minimize user bias and adequately represent the axon heterogeneity. Each set of 100 measurements took approximately 12 minutes to perform manually, with the reduced time accomplished by only measuring one location for axon diameter and myelin thickness.

The correlations shown in Figure 3.6 are much weaker than those of Figure 3.5. In the first panel of Figure 3.6, the mean of the myelin thickness measurements for each ROI are plotted for each technique. The relationship between the two techniques is not strong. The results suggest that the semi-automatic method overestimates the actual myelin thickness. This overestimation could be caused by inaccurate manual threshold levels, which would cause the perimeter of the myelin sheath to be extended past its actual

location. In addition, the inclusion of myelin from neighboring axons in the radial measurements could explain this overestimation of the myelin thickness when using the semi-automatic method. The second panel of Figure 3.6 shows the comparison of techniques for the axon diameter measures. These results suggest that the semi-automatic method underestimates the actual axon diameter. This could be a consequence of the overestimation of myelin thickness. In addition, when using the semi-automatic method, there is a potential for extra-axonal space to be considered as intra-axonal space if it meets the circularity threshold. The overall poor correlation of the two techniques found when expanding the sample number establishes very different results than the previous direct comparison. This discrepancy is potentially caused by the under-sampling or user bias in the initial selection of the 20 axons for the direct comparison.

Figure 3.7 shows the cumulative distribution function for the myelin thickness measurement. The semi-automatic method overestimates the myelin thickness for values less than 0.65 μm due to the internal thresholds on the processing. In order for pixels to be designated as myelin, they must be at least 2 pixels (0.5 μm) thick, resulting in the bias in these thinner myelin measurements. In addition, the semi-automatic method overestimates the myelin thickness for values over 0.8 μm due to the complications from abutting axons' myelin. The manual technique allows exclusion of the myelin from adjacent axons, which could potentially bias the semi-automated results.

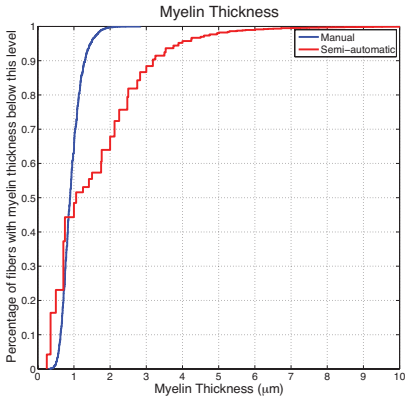

Figure 3.7 – The relative cumulative distribution functions of the myelin thickness measurements for both techniques. All regions of interest are grouped for analysis.

Figure 3.8 shows the comprehensive results of the semi-automated and manual measures for both the myelin thickness and axon diameter. The manual myelin thickness and axon diameter measurements are in agreement with previous histological analysis of the rat cervical spinal cord [10, 11] for the various regions examined, while the semi-automatic measures do not completely agree with the literature values for excised rat spinal cord histology.

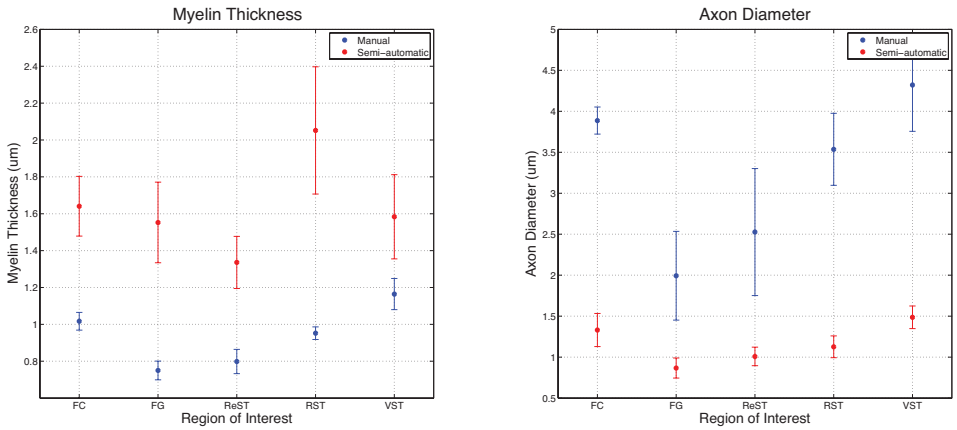

Figure 3.8 – The myelin thickness and axon diameter measurements resulting from the manual and semi-automatic methods.

Conclusions

A semi-automated measurement technique was evaluated for application to histological images of rat cervical spine. The semi-automated results were compared to those of manual measurement. Direct comparison of myelin thickness and axon diameter for twenty axons resulted in a good correlation, but further analysis with a larger sample size did not correlate well. The semi-automated measurement distributions were not normal and did not accurately represent the myelin thickness and axon diameters due to threshold and neighboring axons biasing the measures. Based on the results of this evaluation, the most robust and reliable method for measurement of myelin thickness and axon diameter is the manual measurement technique.

Acknowledgements

The author would like to thank Holly Valentine for help obtaining the spinal cord tissue, Elvin Woodruff and the Cell Imaging Shared Resource for microscopy help, and Kevin Wilson and Tuhin Sinha for image processing assistance.

References

1. Mayhew, T.M. and A.K. Sharma, *Sampling schemes for estimating nerve fibre size. I. Methods for nerve trunks of mixed fascicularity.* Journal of Anatomy, 1984. **139**: p. 45-48.

2. Torch, S., et al., *There is no simple adequate sampling scheme for estimating the myelinated fibre size distribution in human peripheral nerve: a statistical ultrastructural study.* Journal of Neuroscience Methods, 1989. **27**: p. 149-164.

3. Elmoataz, A., et al., *Using active contours and mathematical morphology tools for quantification of immunohistochemical images.* Signal Processing, 1998. **71**: p. 215-226.

4. Amini, A.A., T.E. Weymuth, and R.C. Jain, *Using dynamic programming for solving variational problems in vision.* IEEE Trans Pattern Analysis Machine Intelligence, 1990. **12**: p. 855-67.

5. Fok, Y.L., J.C.K. Chan, and R.T. Chin, *Automated analysis of nerve-cell images using active contour models.* IEEE Transactions on medical imaging, 1996. **15**(3): p. 353-68.

6. Glauert, A.M., *Practical methods in electron microscopy*. Vol. 3 part 1. 1974, North-Holland, Amsterdam.

7. Schwartz, E.D., et al., *Ex vivo evaluation of ADC values within spinal cord white matter tracts.* American Journal of Neuroradiology, 2005. **26**(2): p. 390-397.

8. Wilson, K. and T. Sinha, *Center for Image Analysis; Vanderbilt University Institute of Imaging Science VuTools*, in *http://wiki.vuiis.vanderbilt.edu*, K. Wilson and T. Sinha, Editors. 2007, Center for Image Analysis; Vanderbilt University Institute of Imaging Science.

9. De Vos, K., *Cell Counter*. 2001, http://rsbweb.nih.gov/ij/plugins/cell-counter.html: University of Sheffield, Adademic Neurology.

10. Chin, C.L., et al., *Assessment of axonal fiber tract architecture in excised rat spinal cord by localized NMR q-space imaging: Simulations and experimental studies.* Magnetic Resonance in Medicine, 2004. **52**(4): p. 733-740.

11. Ford, C.J., et al., *Dependence of apparent diffusion coefficients on axonal spacing, membran permeability, and diffusion time in spinal cord white matter.* Journal of Magnetic Resonance Imaging, 1998. **8**(4): p. 775 - 782.

CHAPTER IV

EVALUATION OF MRI RESULTS

Introduction

Magnetic resonance imaging techniques offer tissue contrast but provide limited information regarding the variation of the magnetic resonance signal that exists on a smaller scale than the imaging voxel. The T_2 spectrum from a white matter voxel is interpreted based on the known anatomy of central white matter. The component with the longer T_2 (> 25 milliseconds) is believed to originate from the intra and extra-axonal water, while the component with the shorter T_2 (8 – 25 milliseconds) originates from the myelin water [1-3]. Qualitative histological evaluation corroborates the assignment of the short T_2 component to myelin [4-6] and the MWF qualitatively corresponded to the anatomic distribution of myelin from Luxol Fast Blue stain [7].

The short T_2 component associated with myelin has been previously observed in the central nervous system *in vitro* [2, 3] as well as *in vivo* [1] and has been consistently demonstrated in white matter of the spinal cord [3, 8, 9], although quantitation of the MWF varies between studies. Minty [8] found two T_2 components in excised and in vivo human spinal cord (SC) at 3 Tesla, revealing a myelin T_2 = 16 milliseconds and a relative myelin fraction of 30.7%. This estimate of the MWF is substantially higher than those made in guinea pig SC [3] or bovine brain [10], but they do agree with similar measures in bovine optic nerve (32%) [11] and in vivo measurements of human cervical SC (26.8%) [12].

The specific parameters of the tissue microstructure reflected in MET_2 measurements must still be determined. The myelin histological content of the tissue, axon diameter, and myelin thickness will all have effects on water exchange, potentially impacting the MET_2 signal. The spinal cord provides an environment of normal variation of tissue microstructure, establishing a favorable situation for further analysis of the MET_2 signal and its sensitivities to the tissue microstructure.

One aspect of tissue microstructure of concern is the *g-ratio*. Previous studies have suggested that the thickness of the myelin sheath is related to the axonal fiber size in mature nerve fibers [13-17], with thicker axons having a thicker myelin sheath. Conversely, others have found constant *g-ratios* for all fiber diameters [14-16], and finally, some have found values of *g-ratio* smaller in larger fibers [18]. The axon diameter is known to vary among different WM tracts in the spinal cord axially [19] and is postulated to vary longitudinally based on results indicating variation of spinal roots upon exiting the SC [20]. Therefore, the *g-ratio* could be characteristic of each WM tract. This study examines the MR parameters as well as quantitative histology in order to examine the g-ratio trends. An increase in the *g-ratio* corresponds to a decrease in relative myelin thickness and increase in the myelin surface to volume ratio, while a decrease in *g-ratio* would mean an increase in the myelin thickness relative to the axon diameter and a lower surface to volume ratio. It is possible the MET_2 parameters of myelin are influenced by the *g-ratio.* The local myelin thickness and surface to volume ratio will influence the water exchange between the two tissue compartments, but the specific effects on the MET_2 spectra are still unclear.

The biological basis of both MT and MET_2 imaging methods has been previously studied [1-3, 21-24]. Those examining the MT of WM reveal a parallel between inflammation and changes in the MT parameters [21-23], indicating inflammatory-related changes are often the root of MT measurement changes, but the role of the myelin content and morphometry is yet to be elucidated. The underlying myelin characteristics have also been related to MET_2 measurements, and there is good evidence that the short T_2 component is proportional to the myelin content of the tissue [1-3, 24]. The MWF has been found to consistently decrease with demyelination and corresponding increase in water content [1, 24-26]. Knowledge of the specific origin of the MWF and PSR measurements could elucidate the physiological characteristics of the tissue being imaged, aiding in diagnosis and monitoring of disease treatment. Quantitative histology is used to explore the WM morphometry and its relation to variations in the MR measurements from qMT and MET_2.

Exploration of the covariance between the MWF and MTR [21, 24, 27] as well as between MWF and PSR [21, 24, 25, 28, 29] in WM has been done with varying results. A complete lack of correlation was found by Gareau [21], Vavasour [24], and Laule [27], indicating these MR methods are measuring different attributes of the myelin microstructure. Studies have shown that MET_2 in animal models are more specific than the MT measurements in indicating the myelin content in tissue [5, 21, 30, 31]. Others have found correlations [24] while including demyelinated tissue as well as in healthy WM [28]. Conflicting results confound the ability to relate these two measures of myelin. It is hypothesized that knowledge of the relationship between the MET_2 measurements

and qMT measurements could elucidate the physiological basis of each respective technique.

This study aims to evaluate the underlying tissue parameters influencing magnetic resonance measurements typical of central white matter characterization. Quantitative histology is used to elucidate the tissue structures that affect the variation of MR parameters. In addition, the myelin water fraction, derived from multiexponential T_2 measurements is compared to the myelin pool size ratio measurements, derived from quantitative magnetization transfer imaging. Such an understanding of the complex combination of the various relaxation and exchange properties is important in developing an anatomical basis for interpreting magnetization transfer and T_2 weighted images, particularly with respect to myelination.

Methods

Animal, Tissue Preparation, and Microscopy

Spinal cord tissue was obtained from six Sprague Dawley rats, stained with toluidine blue, and examined with the Leica microscope as previously described in Chapter 3 of this dissertation.

Statistical Analysis

A one-way analysis of variance (ANOVA) was used to determine differences between measurements. If ANOVA results were significant, a post-hoc analysis using the Tukey-

Kramer method for multiple comparisons was used to determine significance differences among means. Significance is defined as a $P < 0.05$.

Magnetic Resonance Imaging

All imaging was performed on a 7 Tesla 16 cm bore Varian Inova scanner using a 6 millimeter loop coil for radio frequency transmission and signal reception. Phantom studies were initially performed to ensure the multi-echo, single slice sequence could reliably measure MET_2. A two-tube phantom was created using $MnCl_2$ (Sigma, St. Louis, MO) to exhibit similar T_2 properties as those expected in spinal cord white matter. The phantoms' T_2 values were measured using a reliable CPMG method as well as the multi-echo, single slice sequence applied to the excised spinal cord sections for MET_2 measurements.

MET_2 spinal cord imaging was achieved using a multi-echo, single-slice modified CPMG sequence [32]. Fixed tissue was submerged in a 5-millimeter outer diameter NMR tube filled with Fomblin (Solvay Solexis, Brussels) to avoid extra signal contribution. Single-slice (2 mm thickness) transverse images were acquired of the spinal cord sections using the multi-echo, single-slice imaging sequence with T_R of 6 seconds, the initial T_E (T_{E1}) minimized at 8 milliseconds, and the subsequent 31 echo times spaced at 9.2 milliseconds. Following the initial 32 echoes, 16 late echoes were acquired at 50 milliseconds spacing for a total of 48 echoes; resulting in echo sampling to approximately 1.1 seconds. Images were acquired at 30 kHz. Six averages resulted in an imaging time of 1 hour and 17 minutes for each sample.

Quantitative magnetization transfer imaging was accomplished using the pulse sequence created by Gochberg and Gore [33]. It was implemented with T_R/T_E = 11,000/10 milliseconds, T_i = 21 points logarithmically spaced from 3.5 to 150 milliseconds, and 300 milliseconds, 1 second, 2 seconds, and 10 seconds, and 6 averages. The field of view, slice thickness, and image resolution is identical to the MET_2 imaging (FOV = 5 x 5 mm, thickness = 2 mm, 32 x 32 imaging matrix.) Least square fitting of the data is performed using MATLAB's built-in Nelder-Mead simplex method.

MET_2 Processing

The image data were filtered using a 3 x 3 median filter and corrected for Rician noise. The regularizing term, λ, was held constant at 1.5 for all processing.

Transverse Region of Interest Selection

Initially, ROIs were drawn manually around five white matter tracts of the rat spinal cord. Examination of MET_2 spectra from the manually drawn ROIs revealed heterogeneity, potentially caused by errors in manual ROI delineation. To address this heterogeneity, additional ROIs (termed high-correlation ROIs) were established based on correlations of the MET_2 spectra. The pixels within the delineated regions of the drawn ROIs having a correlation coefficient > 0.95 were used for further processing.

Results

Phantoms

The results of the phantom imaging studies are found in Table 4.1. Comparable results were found for the multi-echo, single slice sequence when compared to the standard CMPG sequence, validating the multi-echo, single slice sequence for accurate T_2 data acquisition.

Table 4.1- T_2 measurement validation of the multi-echo, single slice (MESS) sequence.

Tube	T_2 (ms) CPMG	T_2 (ms) MESS
A	19.1	18.2
B	35.7	38.8

Microscopy

Microscopy was performed on all extracted tissue; an example is shown in Figure 4.1, the scale-bar indicates a 10-micron distance. The myelin fraction, axon diameter, and myelin thickness for each longitudinal section are shown in Figure 4.2. No significant differences were found except between the myelin thickness of the thoracic and caudal regions, most likely due to the difficulty measuring the caudal region and lack of corresponding white matter tracts. The lack of significant trends along the length of the spinal cord justifies consideration of just the cervical spine for the analysis of transverse regions of interest.

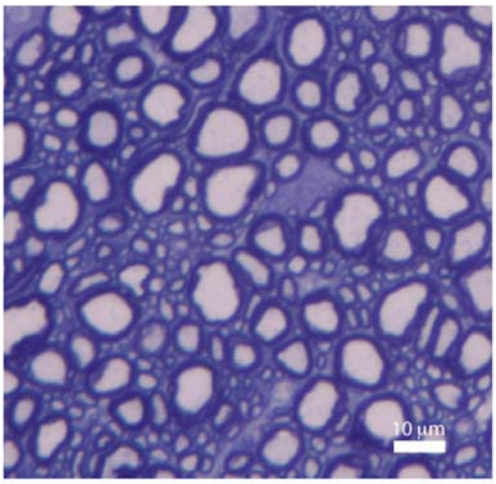

Figure 4.1 – Example micrograph of rat spinal cord stained with Toluidine Blue, scale-bar indicates 10 μm length.

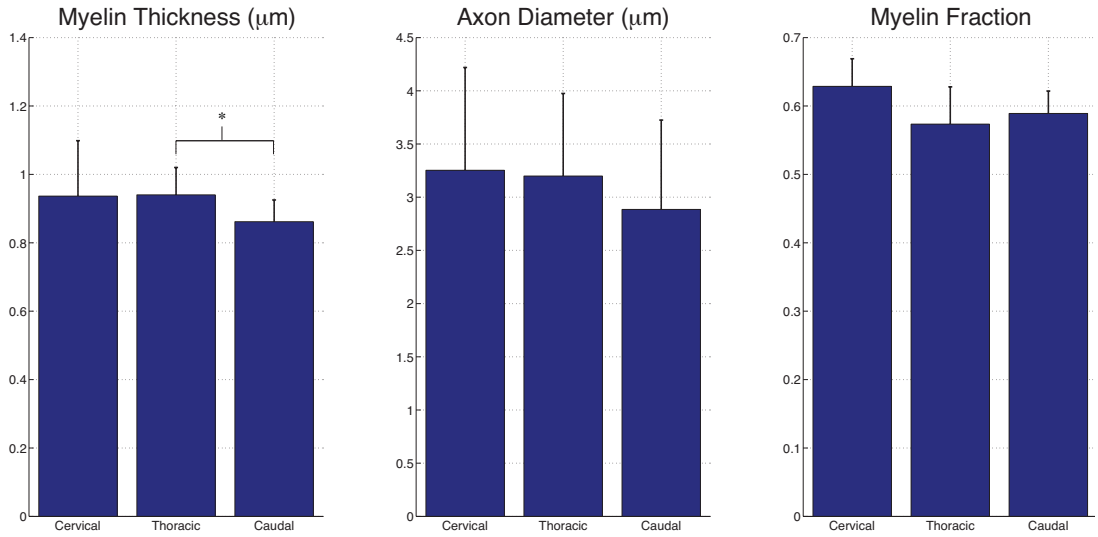

Figure 4.2 – Examination of the mean histological properties of the rat spinal cord for the longitudinal sections (cervical, thoracic, and caudal), error bars indicate standard deviation of sample means. No significant trends were found for progression along the length of the cord.

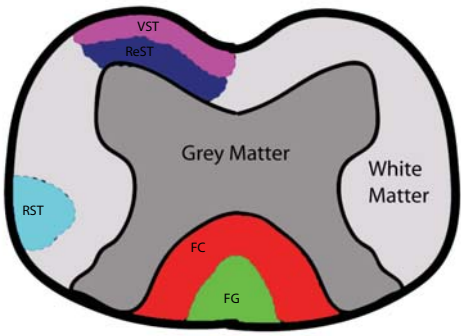

Figure 4.3 – White matter tracts in rat spinal cord, FC = fasciculus cuneatus, FG = fasciculus gracilis, ReST = reticulospinal tract, RST = rubrospinal tract, and VST = vestibulospinal tract.

Figure 4.3 was used as a guide to outline the WM tracts known to have different structure. Photomicrographs were obtained of these regions for each sample (n = 6). Photomicrographs representative of each ROI can be found in Figure 4.4. The measurements resulting from transverse ROI analysis can be found in Figure 4.5. The colors of the bars in Figure 4.5 correspond to the ROIs delineated in Figure 4.3. All white matter tract ROI results were different at the 5% significance level based on ANOVA and post-hoc analysis except the myelin fractions from the ReST and the RST regions. The myelin thickness and axon diameter seem to be related with increasing axon diameter corresponding to an increase in myelin thickness.

The relation between the axon diameter and myelin thickness is apparent with the calculation of the *g-ratio* as previously described. Figure 4.6 plots the myelin thickness as a function of axon diameter for all transverse ROIs in panel A. The correlation coefficient

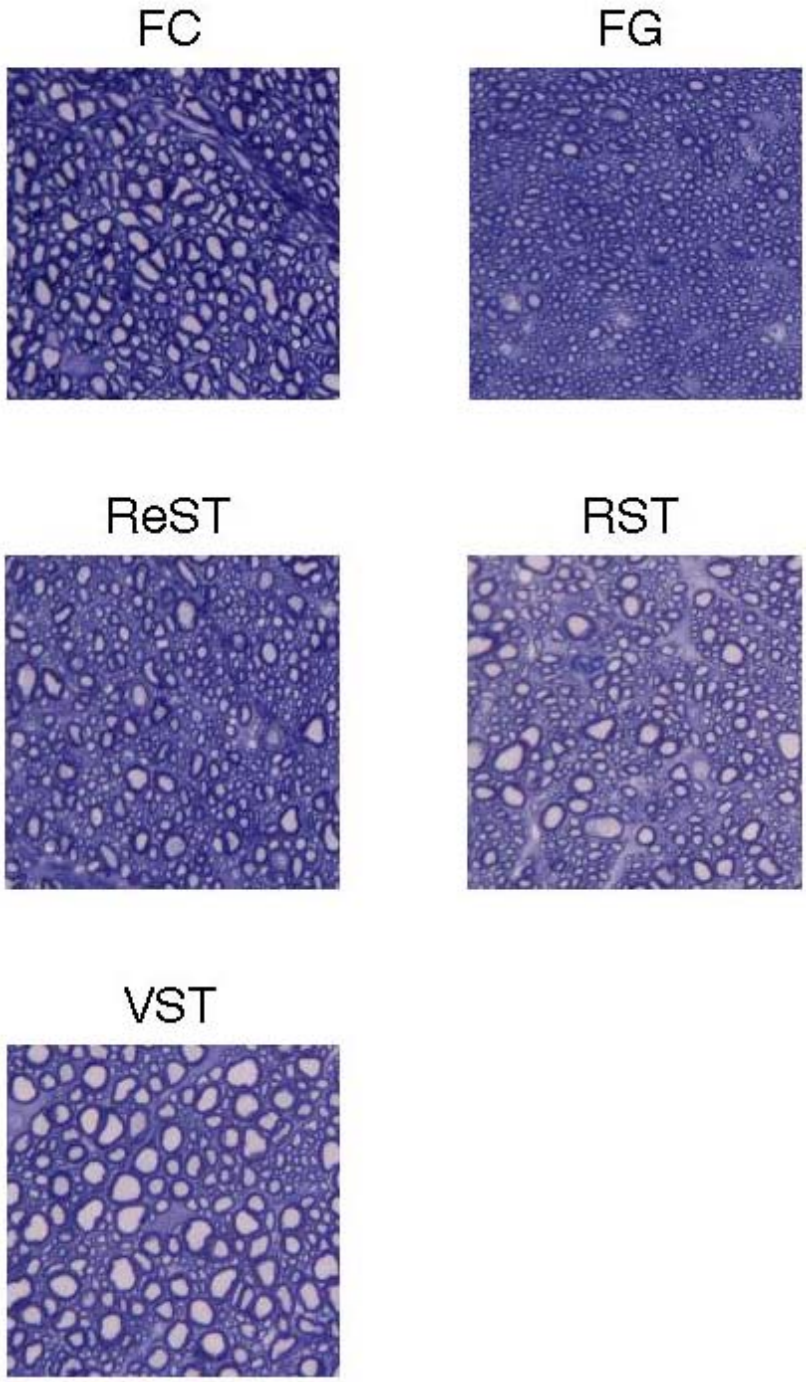

Figure 4.4 – Photomicrographs characteristic of each white matter tract delineated in Figure 4.3.

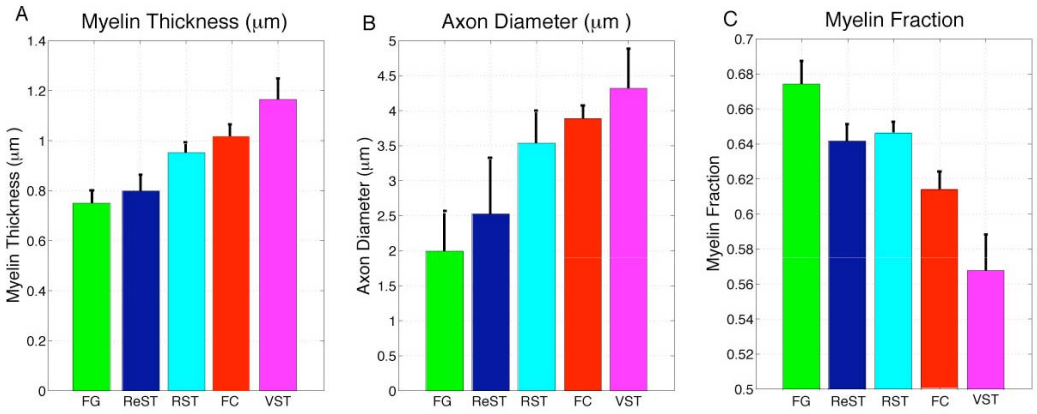

Figure 4.5 – White matter tract ROI microscopy results for the cervical spinal cord. A) myelin thickness, B) axon diameter, and C) myelin fraction determined from Otsu thresholding.

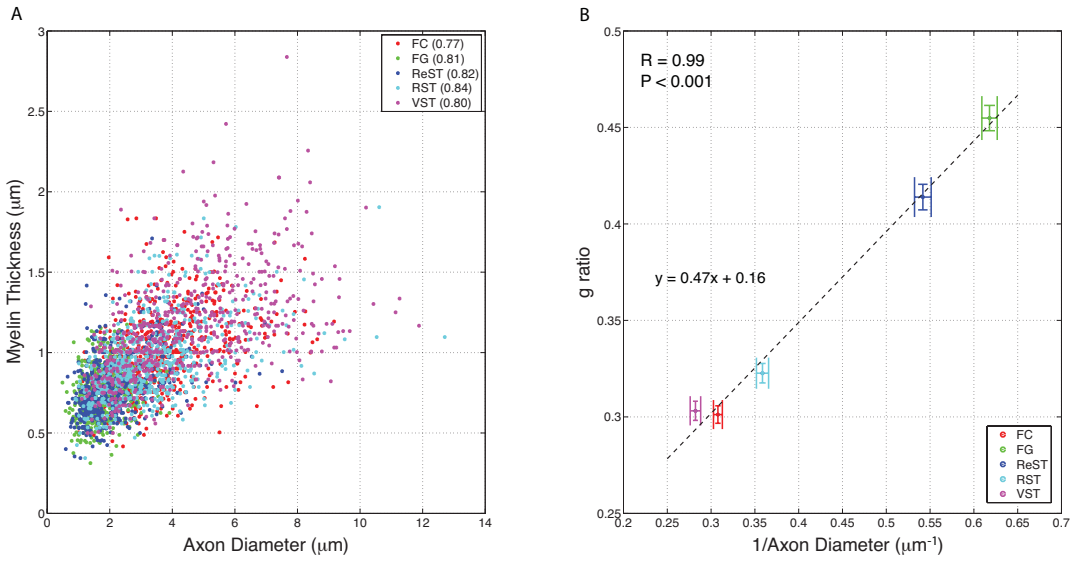

Figure 4.6 – A) Scatter-plot of the axon diameter versus the myelin thickness for the five white matter tract ROIs, individual correlation coefficients indicated in legend. B) Relation between the *g-ratio* and the inverse of the axon diameter measurement.

for the entire data set was 0.97 with individual ROIs' correlation coefficients shown in the legend. Panel B shows the calculated *g-ratio* as a function of the inverse axon diameter with error bars indicating the standard deviation of the measures. The correlation coefficient is 0.99 ($P < 0.001$) indicating a strong dependence of *g-ratio* on the axon diameter.

Further examination of Figure 4.5 indicates a relationship between the axon diameter and the myelin fraction. This is shown in Figure 4.7 where an inverse relation is found between the axon diameter and the myelin fraction, demonstrating as the axon diameter increases, the fraction of the photomicrograph designated as myelin decreases due to increased intracellular space as well as the decreased *g-ratio* in the larger axons. To further investigate the dependence of myelin fraction on axon diameter, the individual relationships were modeled for each WM tract.

Numerical modeling can help understand the dependence of myelin fraction on the local axon diameter. If the photomicrograph is assumed to be a square and the axon

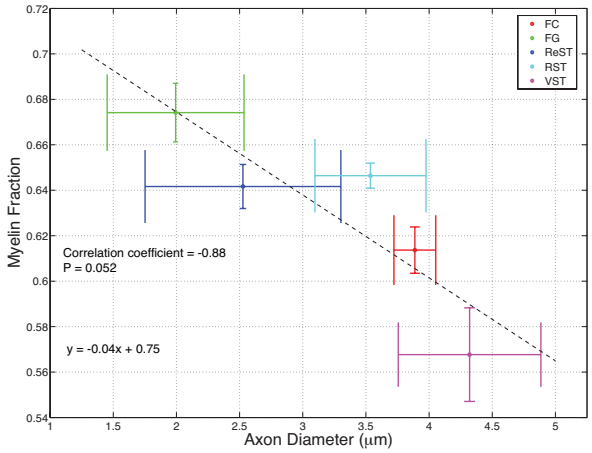

Figure 4.7 – Relation between myelin fraction and axon diameter derived from quantitative histology analysis for different WM tracts.

packing is regular [34], the myelin fraction can be defined as

$$mf = \frac{4\pi\left(r_2 - r_1\right)^2}{r_2^2}, \qquad [4.1]$$

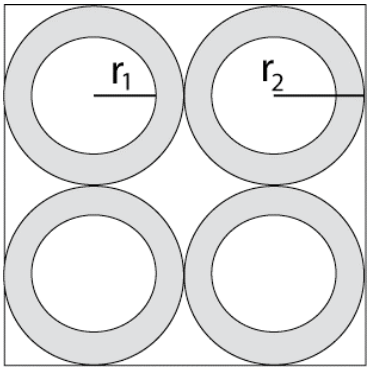

Figure 4.8 – Diagram of WM fibers used to model the relationship between axon diameter and myelin fraction.

where r_1 is the axon radius and r_2 is the fiber radius. Figure 4.8 depicts this geometry. The local *g-ratio* is known to vary based on Figure 4.6. Using the characteristic relationships in each WM tract, the myelin thickness (r_2-r_1) was related to the axon diameter and the resulting *mf* was modeled. The results of this numerical modeling are shown in Figure 4.9. Panel A shows the expected myelin fraction as a function of axon diameter and panel B is a section of panel A with the experimental results. The trends shown in Figure 4.9 A indicate that the myelin fraction is inversely proportional to the axon size up to a certain point, then as the axon grows to larger diameters, the relationship becomes positive. The experimental results from the different WM tracts

overlaid on the model in panel B correspond well for all regions except the VST and FC, regions which are known to be heterogeneous and have typically larger axons.

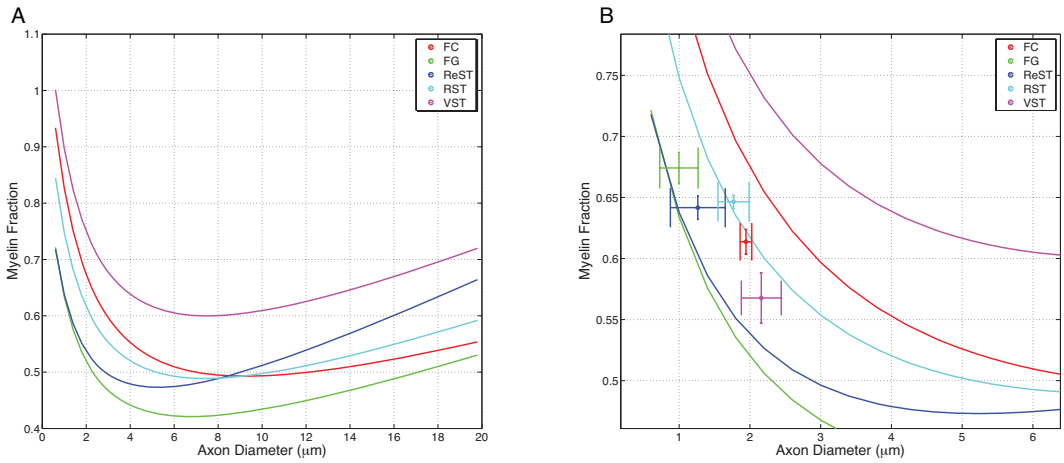

Figure 4.9 – A) Results of numeric modeling for the expected relationship between myelin fraction and axon diameter. B) Modeling results with experimental results plotted, error bars indicate standard deviation of sample means.

Magnetic Resonance Imaging

In the present study, all 18 image sets were analyzed and an example MWF map is shown in Figure 4.10. Examination of this MWF map indicates variation of the MWF within the transverse plane. ROIs were manually drawn on the MWF maps according to the WM tracts delineated in Figure 4.3. These manually drawn ROIs are highlighted in panel A of Figure 4.11. The spectra arising from each voxel within an ROI were averaged and the resulting mean T_2 spectra appear in panel B of Figure 4.11 The five different spectra shown in panel B exhibit different T_2 component signal fractions and mean T_2

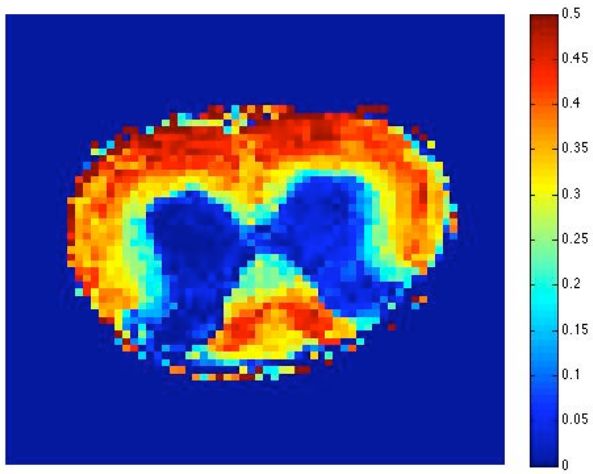

Figure 4.10 – Example of a myelin water fraction map of a rat cervical spinal cord created using multiexponential T_2 analysis.

values for both the myelin and longer T_2 values. These differences suggest that the MET_2 spectra possess underlying information regarding the tissue structure.

Capitalizing on the spectral differences, an additional set of ROIs was created by grouping the pixels with high spectral correlation. The MET_2 spectra were correlated for all pixels within the sample. Pixels that exhibited an $R > 0.95$ and fell within the regions delineated by Figure 4.3 were grouped as the high-correlation ROIs. Examples of high-correlation ROIs are shown in panel C of Figure 4.11. The corresponding mean MET_2 spectra arising from these ROIs appear in panel D of Figure 4.11. The MWF and myelin T_2 resulting from MET_2 analysis of the high-correlation ROIs can be found in Figure 4.12. ANOVA revealed significant differences among the

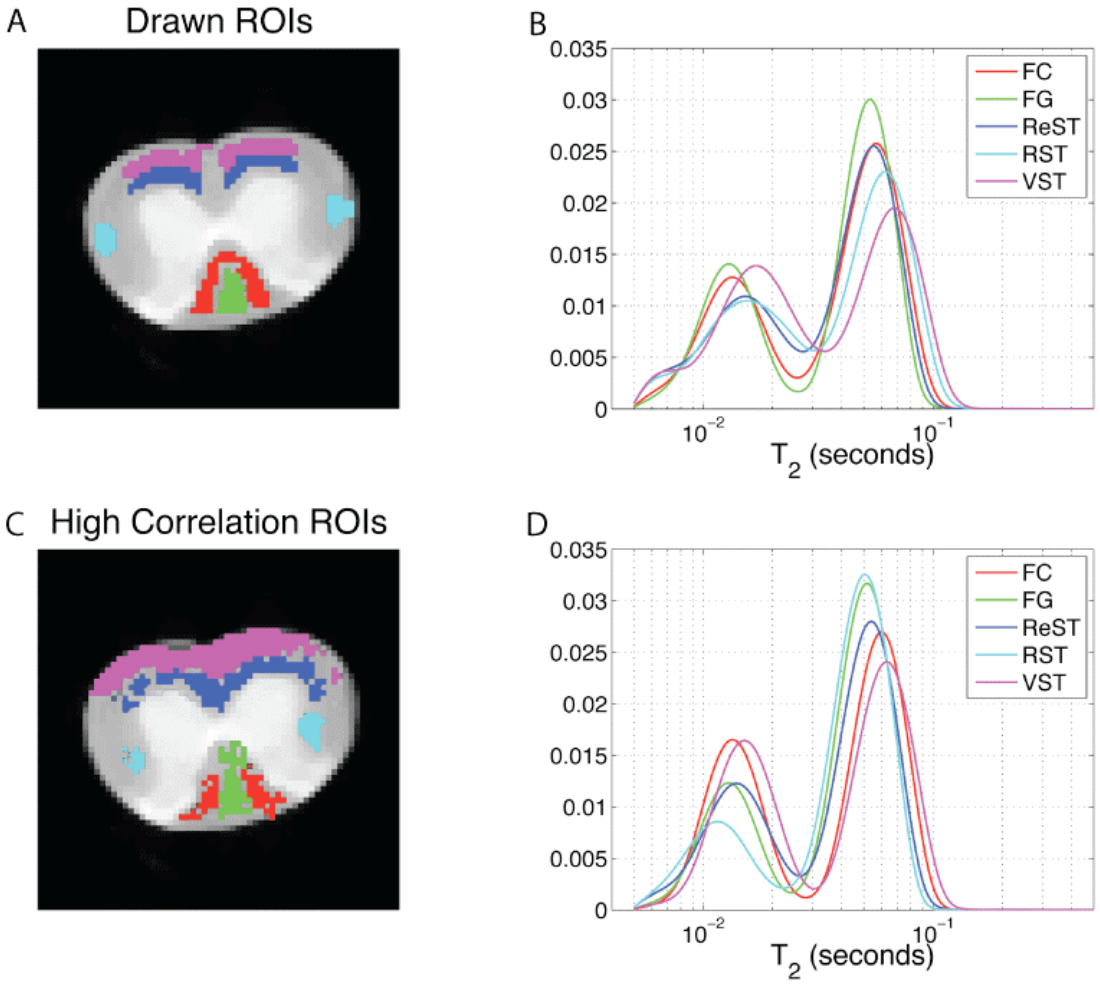

Figure 4.11 – A) Drawn ROIs, B) mean T_2 spectra of drawn ROIs, C) image with high correlation ROIs, and D) mean T_2 spectra of high correlation ROIs.

MWF of white matter tracts with a $P < 0.05$. Post-hoc analysis using the Tukey-Kramer test for multiple comparisons revealed significant differences between all regions. ANOVA indicated significant differences among the myelin T_2 values with post-hoc analysis revealing significant differences between the FC and the FG, ReST, and RST as well as between the VST and the FG, ReST, and RST.

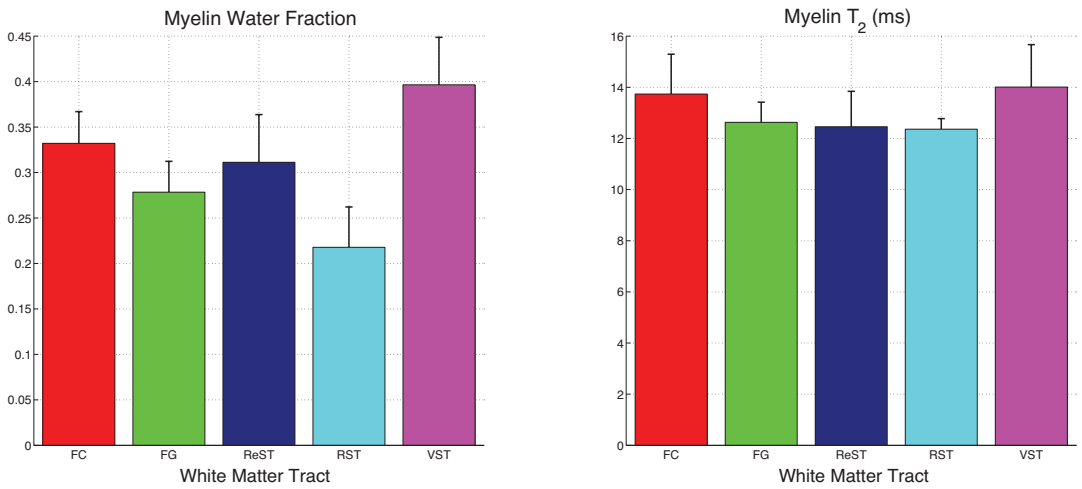

Figure 4.12 – Transverse variation of MET_2 parameters arising from high-correlation ROIs, error bars indicate standard deviation among sample means.

Histology Compared to MET_2

The results of the myelin fraction measurement from quantitative histology are compared to the MET_2 results for the high-correlation ROIs in Figure 4.13. Panel A shows the MWF and panel B shows the myelin T_2 as a function of the histology myelin

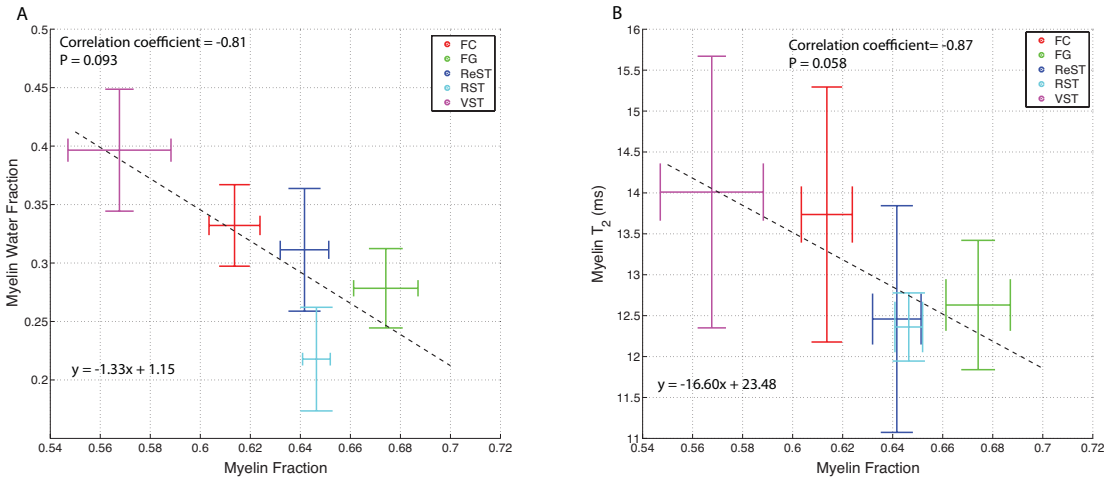

Figure 4.13 – A) myelin water fraction and B) myelin T_2 derived from MET_2 analysis plotted against the myelin fraction resulting from quantitative histology. Error bars indicated standard deviation across sample means.

fraction. Both demonstrate negative but insignificant relationships (P > 0.05) between these parameters. Figure 4.14 presents the MWF as a function of myelin thickness in panel A, demonstrating a linear relationship with the black dashed line (R = 0.95, P > 0.05). The RST region appeared to be an outlier and was excluded for the linear fit denoted by the dashed gray line. Exclusion of the RST region resulted in a significant correlation between the MWF and myelin thickness, R = 0.95, P = 0.04. Panel B shows the MWF as a function of axon diameter with a linear fit of all WM tracts indicated with the dashed black line. Inclusion of all regions for the comparison of MWF to axon diameter also resulted in a weak and insignificant correlation, R = 0.47, P > 0.05. Once again, the RST region appeared as an outlier and was excluded, resulting in a strong

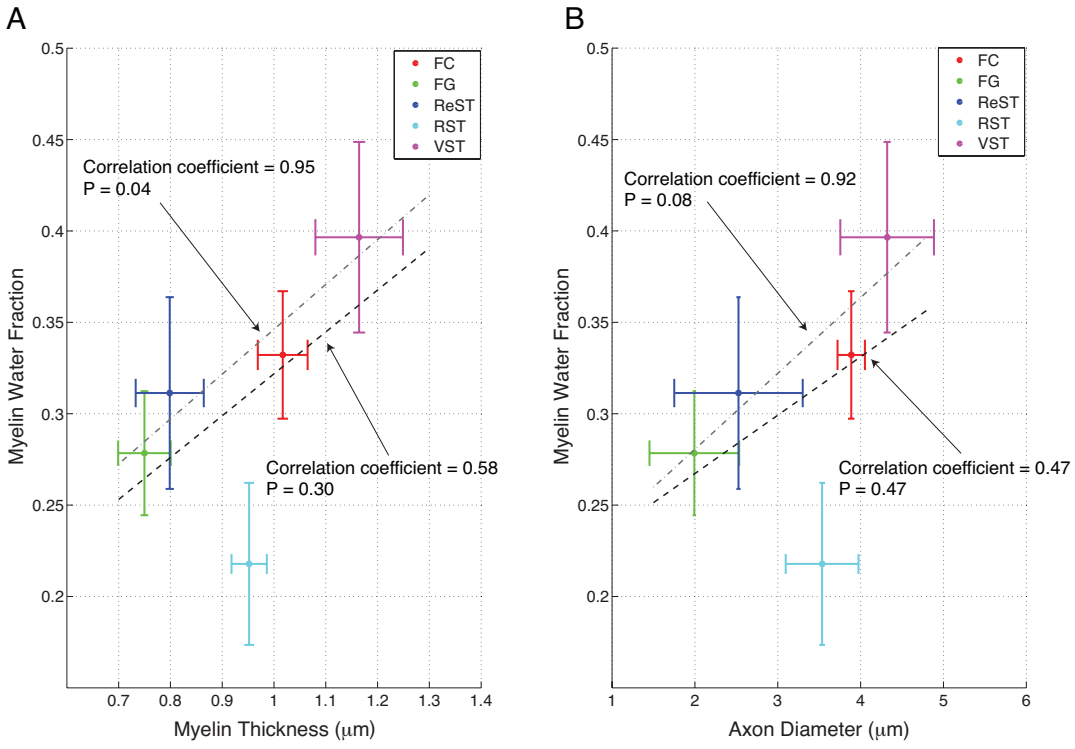

Figure 4.14 – MWF as a function of A) myelin thickness and B) axon diameter. Black dashed line indicates linear fit to all WM tracts while dashed gray line indicates fit excluding RST region.

correlation of 0.92 (P = 0.08) with the gray dashed line indicating a linear fit of the remaining four WM tracts with axon diameter.

Further comparison of the MET_2 and quantitative histology parameters were based on the relationship between the myelin water fraction and the myelin water density,

$$MWF = MF * \rho_m, \qquad [4.4]$$

where MF is the myelin fraction derived from histology and ρ_m is the myelin water density. Figure 4.15 correlates the ratio of MWF/MF to the myelin thickness, essentially comparing the apparent myelin water density ($\tilde{\rho}_m$) to the myelin thickness in each ROI. The correlation coefficient was 0.70 with P < 0.2, indicating the possible existence of different ρ_m values in different spinal cord tracts.

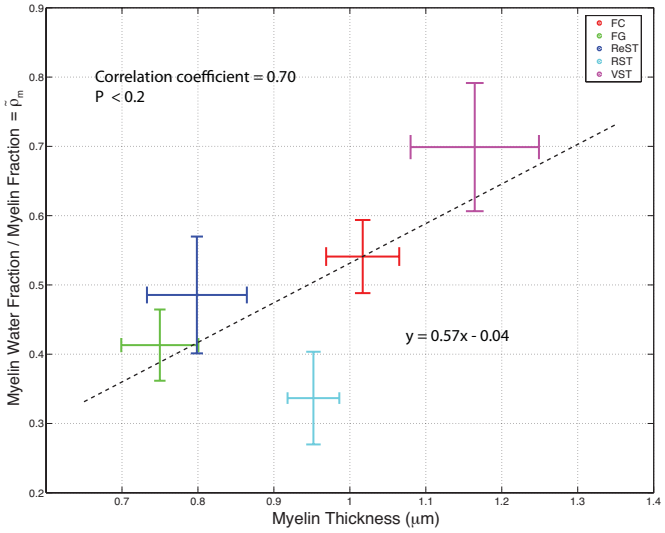

Figure 4.15 – The ratio of MWF/MF, analogous to the ρ_m, as a function of myelin thickness.

Elaboration of this postulated ρ_m variation leads to the relation of T_2 to ρ_m. The local water density within the tissue is known to affect the T_2 distribution [35]. The macromolecules in myelin can be related to the presence of a contrast agent,

$$R_2 \cong R_{2o} + r[myelin], \qquad [4.5]$$

where R_2 is the inverse of T_2, R_{2o} is the initial R_2 value and r is the relaxivity of myelin and [*myelin*] is the concentration of the myelin. This [*myelin*] is inversely proportional to the myelin water density, ρ_m, making Eq. [4.5]

$$R_2 \cong R_{2o} + r/\rho_m, \qquad [4.6]$$

indicating that R_2 is dependent on the inverse of the myelin water density. Assuming the R_2 is dominated by the r/ρ_m term,

$$R_2 \cong r/\rho_m, \qquad [4.7]$$

leads to the conclusion that a change in myelin R_2 is inversely proportional to a change in the myelin water density. Therefore,

$$T_2 \approx \rho_m/r, \qquad [4.8]$$

based on the relation between T_2 and R_2.

The inter-sample variation in myelin T_2 values blurred intra-sample comparisons therefore the relation between T_2 ROI values was examined for each sample. The T_2 for the RST region was used as a reference point to calculate a ΔT_2 for each sample with

$$\Delta T_2 = T_2^{ROI} - T_2^{RST}, \qquad [4.9]$$

where T_2^{RST} is the mean T_2 for the pixels within RST region and T_2^{ROI} denotes the other white matter tracts. This ΔT_2 was calculated for each WM tract within each sample and error was defined as the standard deviation among samples for each WM tract, the mean ΔT_2 is plotted against the $\tilde{\rho}_m$ for each WM tract in Figure 4.16 . Panel A shows this relation for the myelin with a correlation coefficient of 0.98 (P = 0.001) and panel B for the intra- and extra-axonal space with a correlation coefficient of 0.97 (P = 0.007).

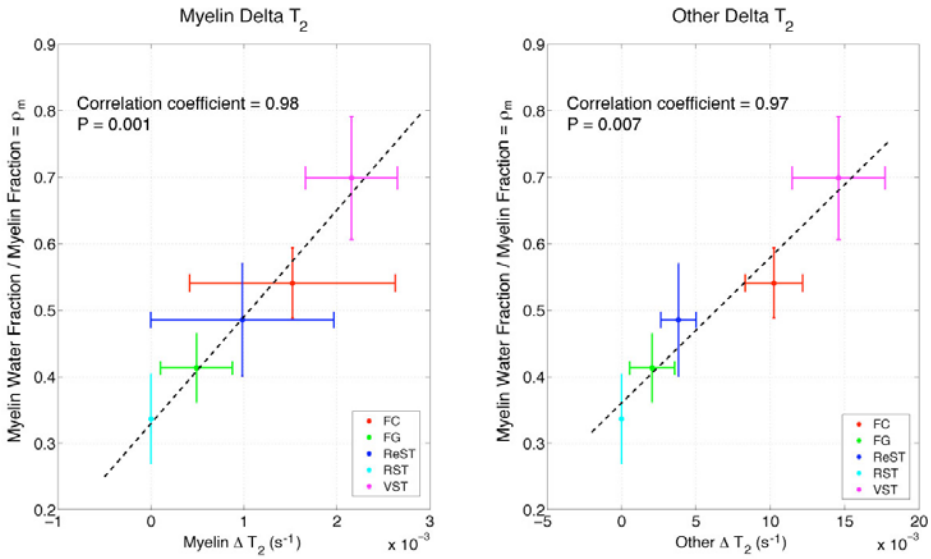

Figure 4.16 – Results supporting the assumed linear relationship between the MWF/MF ratio and the ρ_m. A) MWF/MF as a function of ΔT_2 for myelin component and B) MWF/MF as a function of ΔT_2 for intra- and extra-axonal component.

Histology Compared to qMT

The results of quantitative histology are compared to the results of qMT measures for high-correlation ROIs in Figure 4.17. Panel A shows the relation between the PSR and the myelin fraction for the transverse ROIs. The black dashed line indicates a linear fit to all ROIs, with the correlation coefficient R = 0.11 (P = 0.86), indicating a poor correlation. If the VST ROI is eliminated from the fit and correlation, the dashed grey line results with a correlation coefficient of R = 0.85 (P = 0.15). Panel B shows the relationship between the fast recovery rate, k_{mf}, and the measured myelin fraction, showing no dependence of these parameters.

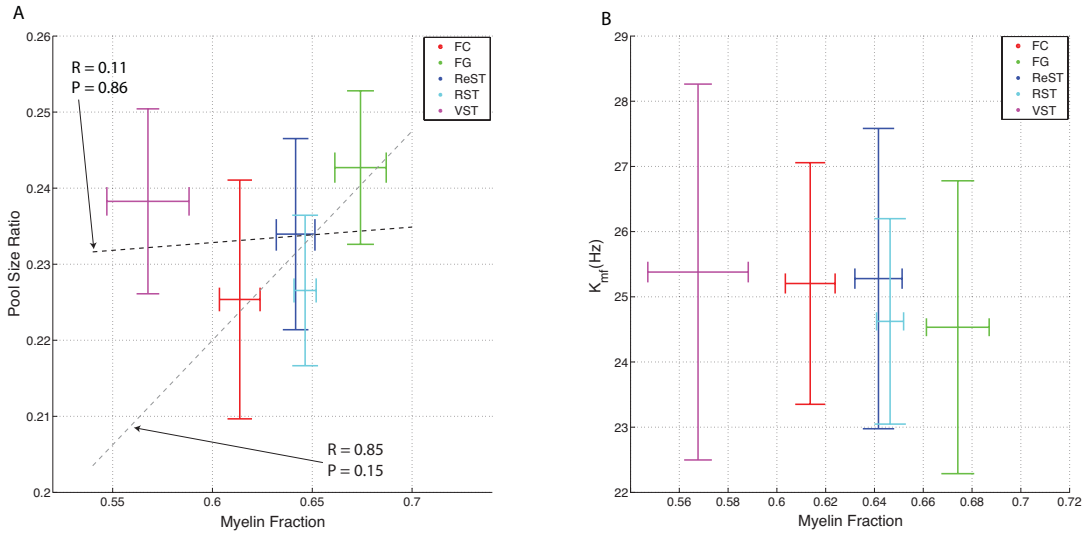

Figure 4.17 – A) Pool size ratio derived from qMT compared to myelin fraction with correlation coefficients and linear fits shown for all ROIs (black) and excluding VST (gray). B) K_{mf} rate derived from qMT compared to myelin fraction.

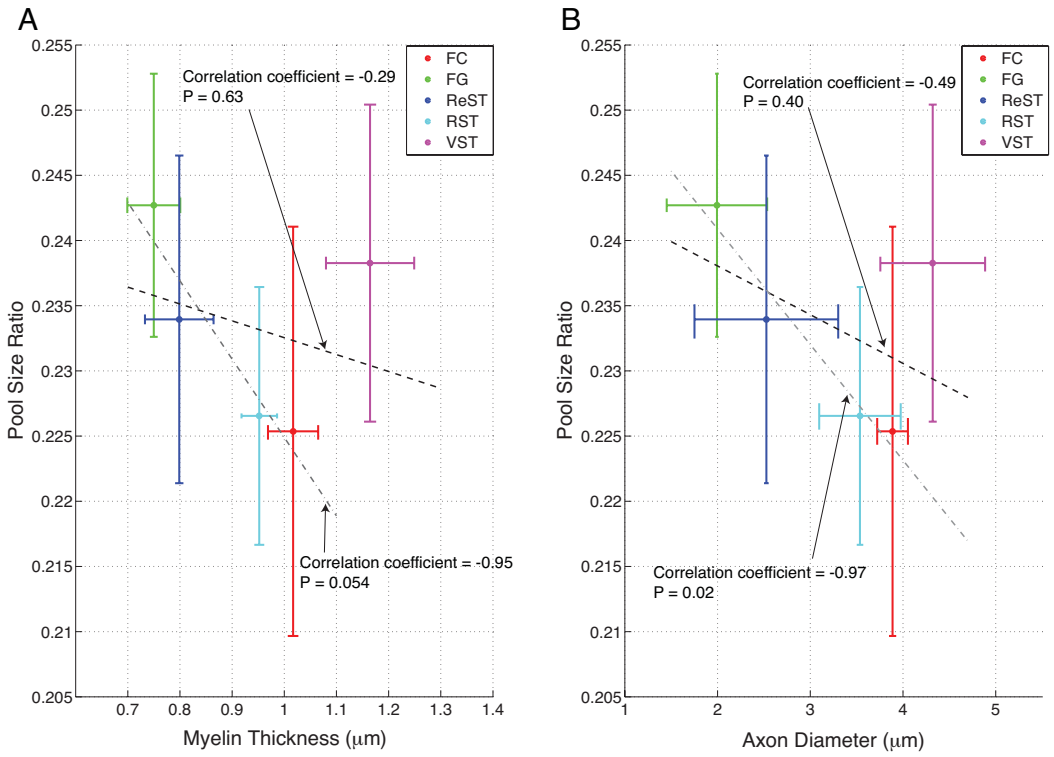

Figure 4.18 – Pool size ratio as a function of A) myelin thickness and B) axon diameter. Dashed black lines indicate linear fit to all WM tracts while dashed gray lines indicate linear fit excluding VST region.

The qMT data is also compared to the structural parameters from histology. Figure 4.18 shows the PSR as a function of A) the myelin thickness and B) the axon diameter. Weak correlations were found when all WM tracts were considered but significant correlations were found upon exclusion of the VST. The PSR and myelin thickness were correlated with $R = -0.95$ ($P = 0.054$) and the PSR and the axon diameter were also significantly correlated with $R = -0.97$ ($P = 0.02$). The comparisons shown in Figures 4.17 and 4.18 indicate a dependence of PSR on the white matter morphology when the VST tract is excluded.

MET_2 Compared to qMT

MET_2 measurements are compared to the qMT measurements in Figure 4.19. Panel A is a pixel-by-pixel scatter plot of the PSR versus the MWF for all WM tracts. There was a weak but significant correlation when considered on this pixel-by-pixel basis. Panel B shows the grouped data with error bars indicating the standard deviation of means across the six samples for each ROI. The grouping of the means produced a lack of correlation between the MWF and PSR measurements.

Further examination of the pixel-by-pixel analysis is explored on a region of interest basis in Figure 4.20. The MWF and PSR relationship is shown for each pixel within the regions, the dashed black line indicates a linear fit to the entire data set. The correlation coefficients and slopes of best linear fit were all found to be significant based on a $P < 0.05$, but the correlation coefficients varied according to the ROI examined. The

correlations between the PSR and MWF are shown as a function of the quantitative histology measurements in Figure 4.21. The correlation strength was independent of parameters extracted from quantitative histology.

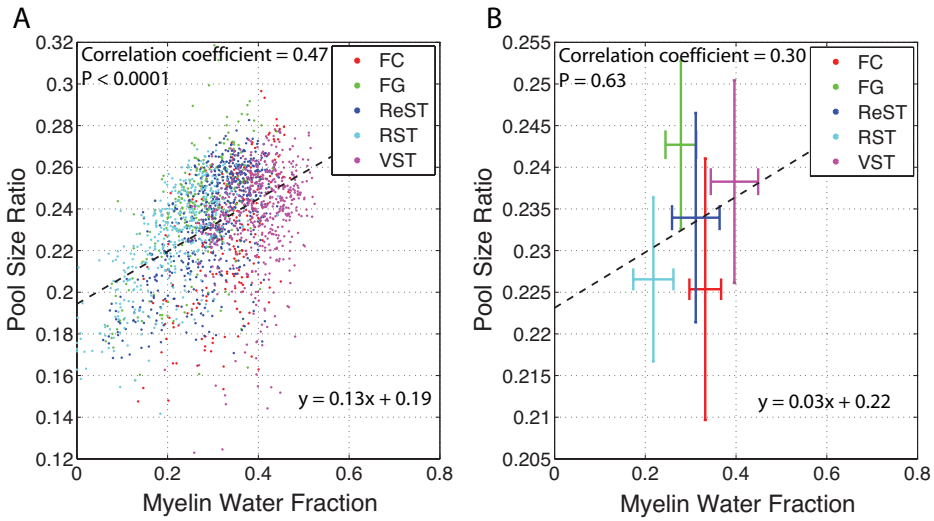

Figure 4.19 – A) PSR compared to MWF on a pixel-by-pixel basis. B) PSR compared to MWF for group averages, error bars indicate standard deviation among sample means.

Discussion

The white matter tracts of the spinal cord present an attractive system for evaluation of quantitative magnetic resonance imaging techniques aimed to probe myelin. Elucidation of the sensitivities of quantitative magnetization transfer and multiexponential T_2 analysis is of great importance for both research and clinical applications. Validation of MRI measurements using quantitative histology can uncover how the tissue parameters influence different MR measurements. The comparison of histological parameters to both MET_2 and qMT myelin measurements along with further correlation of the MR

measurements establishes a comprehensive evaluation of these myelin measurement techniques.

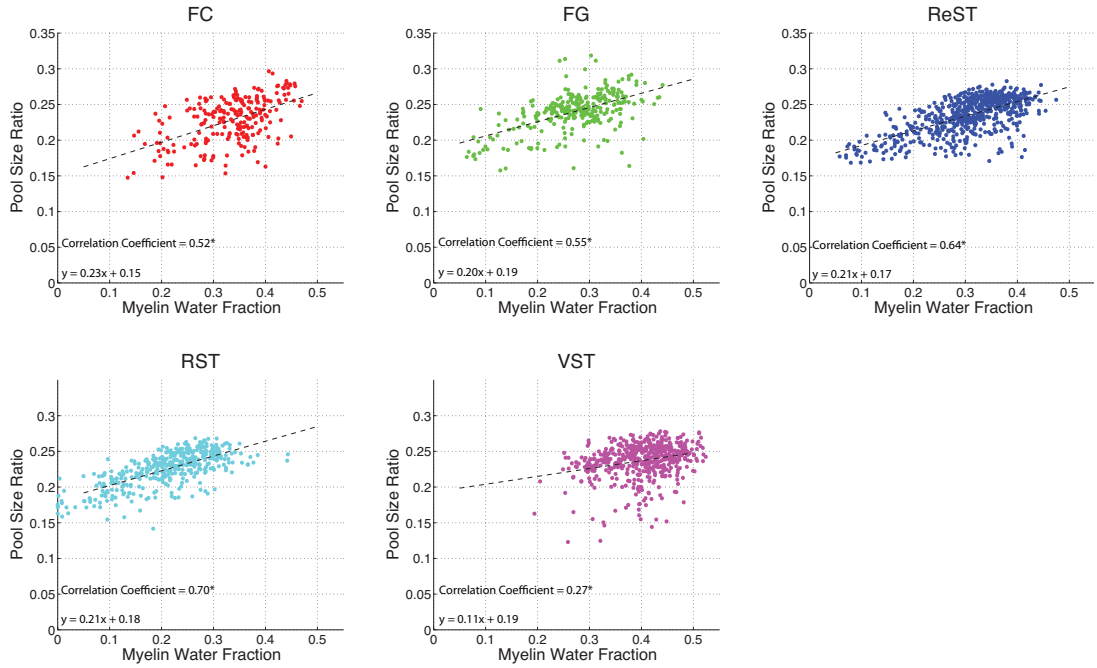

Figure 4.20 – Pixel-by-pixel analysis of relation between MWF and PSR for each WM tract. Correlation coefficients for each tract are shown, significance indicated with an *.

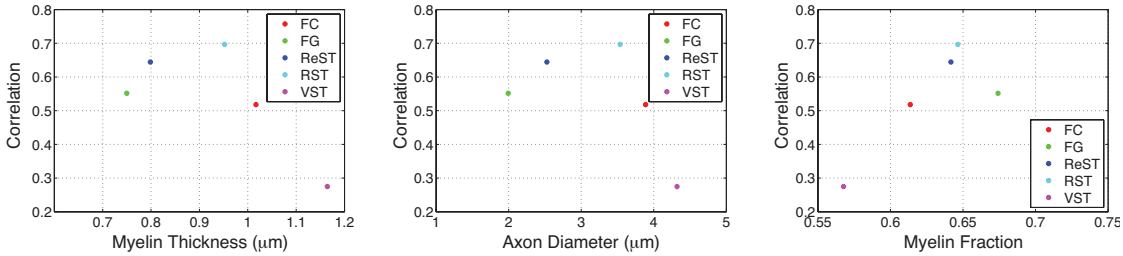

Figure 4.21 – Myelin water fraction and pool size ratio correlation coefficients as a function of quantitative histology measurements.

Histology

Histological analysis of the longitudinal sections of the rat spinal cord revealed no significant longitudinal variation in myelin fraction, myelin thickness, or axon diameter. Ellingson et al. [36] also examined the rat spinal cord longitudinally using apparent diffusion coefficient (ADC) *in vivo*. They found a decrease in the fractional anisotropy with increased distance from the brain. This decrease in anisotropy can be attributed to an increase in the extra-axonal space in the thoracic and caudal spine. The presented findings revealed no trends of tapering or branching along the length of the spinal cord.

Qualitative differences of histology for different white matter tracts within the transverse plane can be observed in the micrographs of Figure 4.4. The appearance of these images corresponds to those of Schwartz et al. [37]. The histological measurements of axon size and myelin fraction of the presented study correspond well to measurements made by Chin et al. [19] who found the average axon diameter in the FG to be 1.1 μm and the FC to be 2.7 μm comparing to average axon diameters of 1.8 μm for the FG and 3.7 mm for the FC in the present study. Previous studies have performed histology on white matter tracts in rat spinal cord [19, 37, 38] revealing similar trends as found in the presented study. In addition to histological studies, various groups have evaluated the rat spinal cord tracts using diffusion MRI [36, 37, 39, 40]. Schwartz and colleagues have suggested that the longitudinal ADC is proportional to the axon diameter [40] and based on this, similar trends were found for axon diameter using quantitative histology as presented in Figure 4.5. This agreement among studies regarding the varying axon morphometry supports the use of the spinal cord to examine variation in MR properties.

The impact of axon diameter on myelin fraction can be observed in Figure 4.7 where, in general, measured myelin fraction increases as axon size decreases. The decreased myelin fraction in the VST is due to the increased axon size and fiber heterogeneity as seen in the micrographs of Figure 4.4. The VST consistently has the largest and most loosely packed axons while the FG (dorsal region) is found to have the smallest axons [19, 38, 40]. The experimental results corresponded to expected results pictured in Figure 4.9. Although the relationship between axon diameter and myelin fraction was negative for the range of axon sizes considered, based on numerical modeling, this relation becomes positive for larger axons.

The axon diameter was also found to influence the myelin thickness. The *g-ratio* was calculated for each fiber examined and is shown in Figure 4.6, panel A, revealing a strong relationship as previously found [13-17]. The *g-ratio* is dependent on axon size as shown in Figure 4.6, panel B. The significantly high correlation coefficient indicates the *g-ratio* is not constant for the WM tracts of the rat cervical spinal cord. This variation of the *g-ratio* with axon size reveals that the myelin thickness increases with axon diameter. The results of *g-ratio* studies vary widely, but they fall broadly into several groups, regardless of the animal or nerve investigated; a) constant values of *g-ratio* for all fiber diameters [14, 41, 42], b) *g-ratio* rising with increasing fiber diameter and reaching a plateau [43-46], c) *g-ratio* continues to rise with increasing fiber diameter without a plateau [47], d) values of *g-ratio* smaller in larger fibers [18], and e) no correlation between *g-ratio* and fiber diameter [48]. The results of the present study support the direct dependency of myelin thickness on axon diameter [43-47].

Histology Compared to MET_2

Comparing the myelin fraction derived from histology to the MWF measurements did not reveal a positive correlation as expected. Previous studies have correlated the MWF arising from MET_2 with measured myelin fraction and found significant positive correlations [6, 27, 49]. These studies examined the optical density of Luxol Fast Blue stain. They also included regions of demyelination in their correlation. The lack of correlation found for normal white matter in this study and the positive correlations found in other studies including demyelinated areas indicate that demyelination could be required for a positive correlation between MWF and myelin fraction from histology.

In addition to the overall myelin fraction, axon morphometry parameters were compared to MET_2. The MWFs for each WM tract (Figure 4.12) were found to be significantly different. The MWF increased with increasing axon size as found in histology and previous studies [19, 37, 38] with the exception of the RST. The example micrograph in Figure 4.4 and larger standard deviation of axon diameter measurements in Figure 4.5 demonstrate the heterogeneity of the RST region. This heterogeneity could explain why the MWF is not higher for this region relative to other regions with smaller axons.

While the MWF is accepted to reflect myelin content, the myelin T_2 can also reveal valuable information regarding the tissue morphometry. T_2 relaxation of water in a particular environment is a complex phenomenon influenced by many variables including proximity of non-aqueous molecules and how far the water molecule diffuses during the

T_2 time scale. Various groups have examined the properties of the peaks from white matter MET_2 [3, 50]. The location of a T_2 peak can reveal information about the amount of water diffusion occurring within the sample or the cellular morphometry. The width of the T_2 peaks may be sensitive to the cellular homogeneity of the sample but fitting techniques present difficulty interpreting this parameter. The width of the T_2 peak changes with the χ^2 misfit of the NNLS fit. The absolute peak width is difficult to interpret because it could be the intrinsic width of a single peak or indistinguishable narrow peaks.

Examination of the MET_2 characteristics can reveal valuable information about the tissue. The relation between myelin fraction and myelin T_2 is not clearly defined. A negative correlation was found between the histological myelin fraction and the myelin T_2, disagreeing with results from Stanisz [30], which included demyelinated regions in the correlations. Significant differences were found between FC and FG, ReST, and RST as well as between VST and FG, ReST, and RST resonating the known histological differences among these regions.

From Eq. [4.4] and [4.7], T_2 and MWF/MF can be related to the water density of myelin, ρ_m. This relationship is shown in Figure 4.16 where the change in T_2 is found to be proportional to the MWF/MF, indicating that the MET_2 parameters reflect information about the local ρ_m. The water density of myelin has been pinned at 0.4 by Morell [51], but other studies have found ranges of 0.3 – 0.5 [52-54]. A range of $\rho_m = 0.35 – 0.70$ was found in this study. The higher values of this calculation could be caused by a bias in the MWF measurement causing over estimation of ρ_m. These higher values of ρ_m could also be a result of a bias in the MF measurement based on the manual morphometry, which

were found to be lower than the semi-automated methods in Chapter 3 of this dissertation. Based on the results in Figure 4.16, it can be concluded that the myelin water density, which can be measured as ΔT_2 is reflective of the local myelin thickness.

Interpretation of axon morphometry effects on the MET_2 parameters is complicated due to the numerous tissue aspects influencing these measures. Based on the presented results, the MWF seems to be a reflection of the myelin thickness and axon diameter where a higher MWF indicates thicker myelin and larger axons. In this respect, variations in the MWF for different WM regions found by Whittall et al. [35] should correspond to different myelin thickness and/or axon size for these regions but limited histological information is available for all WM areas in question. The axon diameter is known to change in the human corpus callosum, with fiber diameter being smaller in the anterior (genu) region and decreasing toward the central region, then increasing again in the posterior (splenium) [55]. In addition, the genu is comprised of 16% unmyelinated fibers compared to < 5% for other WM regions [55]. This presents difficulties interpreting the MWF values Whittall et al. measured in normal human WM. The relatively higher MWF found in the splenium may indicate larger fibers and thicker myelin. Alternately, the relatively lower MWF of the genu could be a consequence of the high percentage of unmyelinated fibers. Overall, the direct relation between MWF and axon morphometry found in the excised rat spinal cord corresponds well with selected MWF measurements in the human brain [35].

In addition, the properties of the MET_2 spectra are affected by water exchange between the myelin and intra- and extra-axonal compartments in the tissue [56]. Evidence exists suggesting relatively slow exchange in CNS tissue [11, 57, 58], but not completely

negligible. The effects of water exchange on the MET_2 signal in the context of WM were examined in Chapter 1 of this dissertation. If water exchange is fast in relation to T_2, the apparent T_2 of myelin, $T_2^{'mye}$, as well as the apparent M_o of myelin, $M_o^{'mye}$, will be smaller than the actual values. Thinner myelin could create such an environment in which water exchange would be fast compared to the T_2, impacting the MET_2 results. Fast exchange could exist in WM tracts with relatively thin myelin (FG, ReST, and RST) explaining the relatively low MWF and T_2^{mye} observed. Underestimation of these values could account for the lack of correlation found between MWF and MF (Figure 4.13). This underestimation due to exchange could also explain the relatively low ρ_m (MWF/MF) values calculated for the WM tracts with thinner myelin, as seen in Figure 4.16. Consequently, the presence of fast exchange can cause the apparent relaxation decay curve to differ significantly, resulting in difficulties comparing the MET_2 results from regions with unique morphometry.

Histology Compared to qMT

Quantitative MT measurements are expected to reflect intrinsic properties of the tissue such as myelin fraction, but correlation of the PSR and myelin fraction revealed no significant relation. This lack of correlation agrees with Odrobina's study in normal white matter tissue [59]. If the VST region is eliminated from the correlation based on the increased size and spacing of the axons and concomitant alteration of the cytoskeletal proteins, a higher correlation is observed, (Figure 4.17 panel A, dashed grey line) but is still not significant. The PSR also reveals an improved correlation with axon diameter

and myelin thickness when the VST is excluded (Figure 4.18). The negative relationship between these fiber parameters could indicate that PSR is related to the axon density, which is proportional to the axon diameter in the cervical spinal cord where fibers are well organized. The VST is known to have a lower *g-ratio* and larger fibers. It seems that the PSR measurements provide more reliable information when examining tracts that include highly-myelinated, tightly packed axons.

MWF and PSR are not directly measuring a single tissue parameter. Expected relations between MR parameters and histological myelin fraction was not observed for either technique, conflicting with expected results. The MWF seems to be a good indicator of the local myelin water density in the situation of slow exchange. The ρ_m can reveal information about the myelin thickness of the constituent axons. The PSR proves to be indicative of axon diameter or axon density, but is not nearly as sensitive based on the outlier results of the VST region. Future studies incorporating a pixel-by-pixel analysis of qMT, MET_2, and corresponding histology data are needed to further examine the white matter tract properties and the sensitivities of the MR techniques.

The techniques of qMT and MET_2 are both probing the properties of myelin in the examined tissue. Logically, the resulting parameters would be related. Figure 4.19 A reveals a significant, but weak pixel-by-pixel correlation between the MWF and PSR. These results agree with those of Vavasour et al. [24] and Tozer et al. [28].Vavasour found an $R = 0.5$ ($P < 0.05$) in human WM including demyelinated regions affected by multiple sclerosis, but Tozer et al. included only normal WM, finding an $R = 0.6$ ($P < 0.05$). Grouping the ROIs as shown in Figure 4.19 B eliminates the relation between the PSR and MWF, agreeing with various other attempts to correlate MWF and MTR [5, 30,

60], as well as PSR [29]. The lack of significant correlation between regions with known variation in tissue parameters indicates the methods are measuring different but complementary aspects of tissue structure.

If each region is examined individually on a pixel-by-pixel basis, Figure 4.20, it is apparent that for some regions the correlation is better. The strengths of the regional correlations are shown in Figure 4.21, which indicates that the relation between PSR and MWF does not depend on tissue morphometry. Interestingly, the relation between PSR and MWF are strongest in regions of median histological parameters. The weakest relation is found in the VST, another indication of uniqueness in this region explained by increased amounts of collagen and extracellular matrix [61]. In addition, when considering the linear fits to the pixel-by-pixel correlations, a higher intercept is found for VST, indicating a higher concentration of macromolecules not associated with myelin such as neurofilaments and microtubules, which could contribute to the MR measurements.

The MET_2 parameters are typically considered more specific indicators of myelin content while MT measurements are found to be more sensitive to physiological changes to myelin resulting from inflammation [1, 4, 27, 49]. The present study reveals the sensitivity of MET_2 to the tissue morphology. While there was no direct correlation between MWF and myelin fraction, the relative location of the myelin T_2 was found to be proportional to the local myelin thickness in the white matter tracts of the spinal cord. While this is not a specific indicator of myelin content, it reveals important information about the local myelin properties. The PSR measurements were found to be related to the tissue architecture as well, particularly to the axon diameter of a tissue. These tissue

parameters would be influenced by inflammation, corresponding well with the established relationship between MT measurements and pathology.

Further studies involving demyelination models could increase the range of measurements, potentially strengthening the relationship between PSR and MWF, as well as help elucidate the sensitivity of each MR technique. Corresponding quantitative histology is imperative due to the complex nature of pathologies. Further examination involving direct correspondence between MR and histology could distinguish concomitant pathologies of inflammation, axonal loss, and demyelination as well as evaluate responses to treatments. Ultimately, distinctions could be made in regards to myelin thickness as well as axon diameter and density based on MR properties.

Conclusions

Quantitative histological measurements were performed on the cervical spine sections. *G-ratios* were found to vary with axon size, revealing a dependence of myelin thickness on with axon diameter. Comparison of the myelin fraction to the MWF measurements did not reveal a positive correlation, although the MWF was found to increase with increasing axon size. The myelin T_2 was also compared to quantitative histology measures, revealing that the myelin water density, which can be measured as ΔT_2 is dependent on the local myelin thickness.

Correlation of the PSR and myelin fraction also revealed no significant relation, indicating that MWF or PSR are not directly measuring a single tissue parameter, direct correspondence between MR parameters and histological myelin fraction was not observed for either technique. The relative myelin T_2 seems to be a good indicator of the

local myelin water density, which can reveal information about the myelin thickness of the constituent axons. The PSR proves to be indicative of axon diameter. Future studies incorporating a pixel-by-pixel analysis of qMT, MET_2, and corresponding histology data are in order to further examine the white matter tract properties and the sensitivities of the MR techniques.

References

1. Mackay, A., et al., *In-Vivo Visualization of Myelin Water in Brain by Magnetic-Resonance.* Magnetic Resonance in Medicine, 1994. **31**(6): p. 673-677.

2. Menon, R.S. and P.S. Allen, *Application of Continuous Relaxation-Time Distributions to the Fitting of Data from Model Systems and Excised Tissue.* Magnetic Resonance in Medicine, 1991. **20**(2): p. 214-227.

3. Stewart, W.A. and e. al., *Spin-Spin Relaxation in Experimental Allergic Encephalomyelitis - Analysis of Cpmg Data Using a Nonlinear Least-Squares Method and Linear Invers-Theory.* Magnetic Resonance in Medicine, 1993. **29**(6): p. 767-775.

4. Gareau, P.J. and e. al., *Magnetization transfer and multicomponent T2 relaxation measurements with histopathologic correlation in an experimental model of MS.* Journal of Magnetic Resonance Imaging, 2000. **11**(6): p. 586-595.

5. Gareau, P.J., et al., *In vivo measurements of multi-component T-2 relaxation behaviour in guinea pig brain.* Magnetic Resonance Imaging, 1999. **17**(9): p. 1319-1325.

6. Webb, S. and e. al., *Is multicomponent T2 a good measure of myelin content in peripheral nerve?* Magnetic Resonance in Medicine, 2003. **49**: p. 638-645.

7. Moore, G.R.W., et al., *A pathology-MRI study of the short-T2 component in formalin-fixed multiple sclerosis brain.* Neurology, 2000. **55**(10): p. 1506-1510.

8. Minty, E.P., *Myelin water measurement in the spinal cord*, in *Physics*. 2005, University of Alberta: Edmonton, Alberta, Canada. p. 119.

9. Minty, E.P., A.L. MacKay, and K.P. Whittall. *Measurement of Myelin Water in Human and Bovine Spinal Cord*. in *ISMRM*. 2002. Honolulu, Hawaii.

10. Vavasour, I.M., *Physics*. 1998: University of British Columbia: Vancouver. 124.

11. Stanisz, G.J., et al., *Characterizing white matter with magnetization transfer and T-2.* Magnetic Resonance in Medicine, 1999. **42**(6): p. 1128-1136.

12. Wu, Y., et al., *Myelin water fraction in human cervical spinal cord in vivo.* Journal of Comput Assist Tomogr, 2006. **30**: p. 304-306.

13. Friede, R.L., T. Miyaghishi, and K.H. Hu, *Axon calibre, neurofilaments, microtubules, sheath thickness nad cholesterol in cat optic nerve fibres.* Journal of Anatomy, 1971. **108**(2): p. 365-373.

14. Samorajski, T. and R.L. Friede, *A quantitative electron microscopic study of myelination in the pyramidal tract of rat.* Journal of Comparative Neurology, 1968. **134**: p. 323-338.

15. Waxman, S.G. and M.V.L. Bennett, *Relative Conduction Velocities of Small Myelinated and Non-Myelinated Fibers in Central Nervous-System.* Nature-New Biology, 1972. **238**(85): p. 217-&.

16. Waxman, S.G. and H.A. Swadlow, *Ultrastructure of Visual Callosal Axons in Rabbit.* Experimental Neurology, 1976. **53**(1): p. 115-127.

17. Williams, P.L. and C.P. Wendell-Smith, *Some additional parametric variations between peripheral nerve fibre populations.* Journal of Anatomy, 1971. **109**(3): p. 505-526.

18. Fraher, J.P., *Myelin-axon relationships in the rat phrenic nerve: longitudinal variation and lateral asymmetry.* Journal of Comparative Neurology, 1992. **323**: p. 551-557.

19. Chin, C.L., et al., *Assessment of axonal fiber tract architecture in excised rat spinal cord by localized NMR q-space imaging: Simulations and experimental studies.* Magnetic Resonance in Medicine, 2004. **52**(4): p. 733-740.

20. Lubinska, L. and J. Waryszewska, *Fibre population of the phrenic nerve of rat: changes of myelinated fibre dimensions along the nerve and characteristics of axonal branchings.* Acat. Neurobiol. Exp., 1974. **34**(525-541).

21. Gareau, P.J., et al., *Magnetization transfer and multicomponent T2 relaxation measurements with histopathologic correlation in an experimental model of MS.* Journal of Magnetic Resonance Imaging, 2000. **11**(6): p. 586-595.

22. Fillippi, M., et al., *Short-term evolution of individual enhancing multiple sclerosis lesions studied with magnetization transfer imaging.* Magnetic Resonance Imaging, 1999. **17**: p. 979-984.

23. Dousset, V., R.I. Grossman, and K.N. Ramer, *Experimental allergic encephalomyelitis and multiple sclerosis: lesion characterization with magnetization transfer imaging.* Radiology, 1992. **182**: p. 483-491.

24. Vavasour, I.M., et al., *A comparison between magnetization transfer ratios and myelin water percentages in normals and multiple sclerosis patients.* Magnetic Resonance in Medicine, 1998. **40**(5): p. 763-768.

25. Laule, C., et al., *Water content and myelin water fraction in multiple sclerosis - A T-2 relaxation study.* Journal of Neurology, 2004. **251**(3): p. 284-293.

26. Laule, C., et al., *Myelin water imaging in multiple sclerosis: quantitative correlations with histopathology.* Multiple Sclerosis, 2006. **12**: p. 747-753.

27. Laule, C., et al. *Correlation between magnetization transfer ratio and myelin water content in normal white matter and MS lesions.* in *Proceedings of the annual meeting of the international society for magnetic resonance in medicine.* 2002. Honolulu, Hawaii.

28. Tozer, D.J., et al., *Correlation of apparent myelin measures obtained in multiple sclerosis patients and controls from magnetization transfer and multicompartmental T-2 analysis.* Magnetic Resonance in Medicine, 2005. **53**(6): p. 1415-1422.

29. Sled, J.G., et al., *Regional variations in normal brain shown by quantitative magnetization transfer imaging.* Magnetic Resonance in Medicine, 2004. **51**: p. 299-303.

30. Stanisz, G.J., et al., *MR properties of excised neural tissue following experimentally induced inflammation.* Magnetic Resonance in Medicine, 2004. **51**(3): p. 473-479.

31. Moore, G.R.W., et al., *The short T2 component is absent in chronically demyelinated plaques in formalin-fixed multiple sclerosis brain.* Neurology, 1999. **52**(6): p. A567-A567.

32. Poon, C.S. and R.M. Henkelman, *Practical T2 quantitation for analysis of multicomponent tissue T2 relaxation data.* Journal of Magnetic Resonance Imaging, 1992. **2**(5): p. 541-553.

33. Gochberg, D.F. and J.C. Gore, *Quantitative imaging of magnetization transfer using an inversion recovery sequence.* Magnetic Resonance in Medicine, 2003. **49**: p. 501-505.

34. Ford, J.C., et al., *Dependence of apparent diffusion coefficients on axonal spacing, membrane permeability, and diffusion time in spinal cord white matter.* Journal of Magnetic Resonance Imaging, 1998. **8**: p. 775-782.

35. Whittall, K.P., et al., *In vivo measurement of T-2 distributions and water contents in normal human brain.* Magnetic Resonance in Medicine, 1997. **37**(1): p. 34-43.

36. Ellingson, B.M., et al., *In vivo diffusion tensor imaging of the rat spinal cord at 9.4T.* Journal of Magnetic Resonance Imaging, 2008. **27**(3): p. 634-642.

37. Schwartz, E.D., et al., *Ex vivo evaluation of ADC values within spinal cord white matter tracts.* American Journal of Neuroradiology, 2005. **26**(2): p. 390-397.

38. Lehnen, L.P.H., et al., *Differences in the fiber composition of the pyramidal tracts in two- and 14 month-old rats.* Neuroscience, 1989. **28**(3): p. 635-643.

39. Gullapalli, J., J. Krejza, and E.D. Schwartz, *In vivo DTI evaluation of white matter tracts in rat spinal cord.* Journal of Magnetic Resonance Imaging, 2006. **24**(1): p. 231-234.

40. Schwartz, E.D., et al., *MRI diffusion coefficients in spinal cord correlate with axon morphometry.* Neuroreport, 2005. **16**(1): p. 73-76.

41. Waxman, S.G. and M.L.V. Bennett, *Relative conduction velocities of small myelinated and non-myelinated fibres in the central nervous system.* Nature (London), 1972. **238**: p. 217-219.

42. Waxman, S.G. and H.A. Swadlow, *Ultrastructure of visual callosal axons in the rabbit.* Experimental Neurology, 1976. **53**: p. 115-127.

43. Gasser, H.S. and H. Grundfest, *Axon diameters in relation to the spike dimensions and conduction velocity in mammalian A fibres.* American Journal of Physiology, 1939. **127**: p. 393-414.

44. Sanders, F.K., *The thickness of myelin sheaths of normal and regenerating peripheral nerve fibre.* Proceedings of royal society B, 1948. **135**: p. 323-357.

45. Schmitt, F.O. and R.S. Bear, *The optical properties of vertebrate nerve axons as related to fibres size.* Journal of cell comparative physiology, 1937. **9**: p. 261-273.

46. Taylor, G.W., *The correlation between sheath birefringuence and conduction velocity with special reference to cat nerve fibres.* Journal of cell comparative physiology, 1942. **20**: p. 359-372.

47. Fraher, J.P. and J.P. Rossiter, *Myelin-axon relationships established by rat vagal schwann cells deep to the brainstem surface.* Journal of Comparative Neurology, 1991. **304**: p. 253-260.

48. Friede, R.L. and T. Samorajki, *Relation between the number of myelin lamellae and axon circumference in fibers of vagus and sciatic nerves of mice.* Journal of Comparative Neurology, 1967. **130**: p. 223-232.

49. Laule, C., et al., *Myelin water imaging of multiple sclerosis at 7T: correlations with histopathology.* NeuroImage, 2007. **In Press**.

50. Whittall, K.P., et al., *In vivo Measurement of T2 Distributions and Water Contents in Normal Human Brain.* Magnetic Resonance in Medicine, 1997. **37**(1): p. 34-43.

51. Morell, P., R.H. Quarels, and W. Norton, *Formation, structure, and biochemistry of myelin*, in *Basic Neurochemistry: Molecular, Cellular, and Medical Aspects*, J. Siegel, Editor. 1989, Raven Press Ltd.: New York, NY. p. 109-136.

52. Caspar, D.L.D. and Kirschne.Da, *Myelin Membrane Structure at 10 a Resolution.* Nature-New Biology, 1971. **231**(19): p. 46-&.

53. Finean, J.B., *The role of water in the structure of peripheral nerve myelin.* J. Biophys. Biochem. Cytol., 1957. **3**: p. 95-102.

54. Schmitt, F.O., R.S. Bear, and K.J. Palmer, *X-ray diffraction studies on te structure of the nerve myelin sheath.* J. Cell. Comp. Physiol., 1941. **18**: p. 31-42.

55. Aboitiz, F., et al., *Fiber composition of the human corpus callosum.* Brain Research, 1992. **598**(1-2): p. 143-153.

56. Woessner, D.E., *Brownian motion and its effects in NMR chemical exchange and relaxation in liquids.* Concepts in Magnetic Resonance, 1996. **8**(6): p. 397-421.

57. Bjarnason, T., et al., *Characterization of the NMR behaviour of white matter in bovine brain.* Magnetic Resonance in Medicine, 2005. **54**: p. 1072-1081.

58. Vavasour, I.M., et al., *Different magnetization transfer effects exhibited by the short and long T(2) components in human brain.* Magnetic Resonance in Medicine, 2000. **44**: p. 860-866.

59. Odrobina, E.E., et al., *MR properties of excised neural tissue following experimentally induced demyelination.* NMR in Biomedicine, 2005. **18**(5): p. 277-284.

60. Mackay, A., et al., *In-Vivo Visualization of Myelin Water in Brain by Magnetic-Resonance.* Magnetic Resonance in Medicine, 1994. **31**(6): p. 673-677.

61. Matesz, C., et al., *Extracellular matrix molecules and their possible roles in the regeneration of frog nervous system.* Brain Research Bulliten, 2005. **66**: p. 526-531.

CHAPTER V

CONCLUSIONS

Most magnetic resonance imaging techniques offer tissue contrast but provide limited information regarding the variation of the magnetic resonance signal that exists on a smaller scale. The magnetic resonance signal is a reflection of the tissue compartments within the imaging voxel. Analysis of this signal can better characterize the micro-anatomical heterogeneity tissue, white matter in particular. Many questions remain with regard to the compartmental contributions for the various types of MRI contrast. This project utilized a variety of *in vitro* studies as well as simulations to better characterize the contribution of different water compartments to conventional MRI methods providing understanding of the complex combination of the various relaxation and exchange properties important in developing an anatomical basis for interpreting magnetization transfer and T_2 weighted images, particularly with respect to myelination.

Simulations were used to investigate data requirements for multicomponent T_2 analysis under experimental conditions common for clinical and research MRI scanners. Sweepwidth, minimum T_E, and matrix size combinations were found over a range of typical research parameters for optimal MET_2 quantification of myelin.

Histological analysis was used to evaluate the results of MR measurements. A semi-automated measurement technique was evaluated for application to histological images of rat cervical spine. The semi-automated results were compared to those of manual measurement. Direct comparison of myelin thickness and axon diameter for twenty axons resulted in a good correlation, but further analysis with a larger sample size did not

correlate well. The semi-automated measurement distributions did not accurately represent the myelin thickness and axon diameters due to threshold and neighboring axons biasing the measures. Based on the results of this evaluation, the most robust and reliable method for measurement of myelin thickness and axon diameter is the manual measurement technique.

Quantitative histological measurements were performed on the cervical spine sections. *G-ratios* were found to vary with axon size, revealing a dependence of myelin thickness on axon diameter. Comparison of the myelin fraction to the MWF measurements did not reveal a positive correlation as expected although the MWF was found to increase with increasing axon size. The lack of correlation found for normal white matter in this study and the positive correlations found in other studies including demyelinated areas indicate that demyelination could be required for a positive correlation between MWF and myelin fraction from histology. The myelin T_2 was also compared to quantitative histology measures, revealing that the myelin water density, which can be measured as ΔT_2 is dependent on the local myelin thickness.

Correlation of the PSR and myelin fraction also revealed no significant relation, indicating that MWF or PSR are not directly measuring a single tissue parameter, correspondence between MR parameters and histological myelin fraction was not observed for either technique, conflicting with expected results. The relative myelin T_2 seems to be a good indicator of the local myelin water density, which can reveal information about the myelin thickness of the constituent axons. The PSR proves to be indicative of axon diameter. Future studies incorporating a pixel-by-pixel analysis of

qMT, MET_2, and corresponding histology data are in order to further examine the white matter tract properties and the sensitivities of the MR techniques.

The white matter tracts of the spinal cord present an ideal system for evaluation of quantitative magnetic resonance imaging techniques aimed to probe myelin. Elucidation of the sensitivities of quantitative magnetization transfer and multiexponential T_2 analysis is of great importance for both research and clinical applications. Validation of MRI measurements using quantitative histology can uncover the tissue parameters influencing the different MR measurements. The comparison of histological parameters to both MET_2 and qMT myelin measurements along with further correlation of the MR measurements establishes a comprehensive evaluation of these myelin measurement techniques.